

N 70 27 17 9

NASA CR-72674
BOEING D2-121734-1



HIGH VOLTAGE SOLAR ARRAY STUDY

by
W. F. Springgate

THE **BOEING** COMPANY

CASE FILE COPY

prepared for
NATIONAL AERONAUTICS AND SPACE ADMINISTRATION

NASA Lewis Research Center
Contract NAS3-11534
Stanley Domitz, Project Manager

NOTICE

This report was prepared as an account of Government-sponsored work. Neither the United States, nor the National Aeronautics and Space Administration (NASA), nor any person acting on behalf of NASA:

- A.) Makes any warranty or representation, expressed or implied, with respect to the accuracy, completeness, or usefulness of the information contained in this report, or that the use of any information, apparatus, method, or process disclosed in this report may not infringe privately-owned rights; or
- B.) Assumes any liabilities with respect to the use of, or for damages resulting from the use of, any information, apparatus, method or process disclosed in this report.

As used above, "person acting on behalf of NASA" includes any employee or contractor of NASA, or employee of such contractor, to the extent that such employee or contractor of NASA or employee of such contractor prepares, disseminates, or provides access to any information pursuant to his employment or contract with NASA, or his employment with such contractor.

FINAL REPORT
HIGH VOLTAGE SOLAR ARRAY STUDY

Prepared By:

W. F. Springgate - Technical Leader

Henry Oman - Program Leader

THE BOEING COMPANY
AEROSPACE GROUP
KENT FACILITY
P.O. BOX 3999
SEATTLE, WASHINGTON 98124

Prepared For:

NATIONAL AERONAUTICS AND SPACE ADMINISTRATION

NASA-LEWIS RESEARCH CENTER
CLEVELAND, OHIO

Contract NAS3-11534

Stanley Domitz, Project Manager
Spacecraft Technology Division

FOREWARD

The research described herein, which was conducted by The Boeing Company, Aerospace Systems Division, was performed under NASA Contract NAS3-11534. The work was done under the management of the NASA Project Manager, Mr. Stanley Domitz, Spacecraft Technology Division, NASA Lewis Research Center.

TABLE OF CONTENTS

	<u>Page</u>
1.0 INTRODUCTION	2
2.0 SPACE ENVIRONMENT MODEL	3
3.0 LEAKAGE CURRENTS	8
4.0 ENVIRONMENTAL EFFECTS	23
5.0 INSULATION BREAKDOWN	33
6.0 FABRICATION AND CONCEPTUAL DESIGN	47
7.0 RELIABILITY ANALYSES	58
8.0 CONCLUSIONS	67
9.0 GLOSSARY	69
10.0 APPENDIX 1: COMPUTER PROGRAM FOR CURRENT COLLECTION	70
11.0 APPENDIX 2: DETERMINATION OF NET ACCELERATING VOLTAGE PRODUCED BY A SOLAR ARRAY OPERATING AN ION THRUSTOR	78
12.0 APPENDIX 3: PLASMA-RESISTANT ORGANIC MATERIALS	90
13.0 APPENDIX 4: HIGH VOLTAGE SOLAR ARRAY SPACE ENVIRONMENT MODEL	91
14.0 REFERENCES	141

ABSTRACT

The problems in operating a 15 kW, 2 to 16 kV solar array in Earth orbit are analyzed. The array would first power ion thrusters on a spacecraft climbing from 185 km to synchronous altitude, and then power transmitting tubes for 5 years. Such an array is feasible. Solar-cell interconnectors and other conducting surfaces would probably be insulated to prevent power loss through plasma. Several insulated-array designs appear practical. High-voltage insulations must be tested in the laboratory for performance in the ionospheric plasma, followed by 5 years in synchronous orbit. The leakage current from exposed conductors and through pinholes needs to be calculated for all plasma conditions, and confirmed experimentally.

SUMMARY

The purpose of the study described in this report was to define the problems associated with operating a high voltage solar array in Earth orbit and to recommend methods for solving these problems. Voltages considered were 2000 volts to 16,000 volts, both positive and negative with respect to the spacecraft. The solar array would power ion thrusters to raise a spacecraft from low Earth orbit (185 kilometers) to synchronous orbit (35,800 kilometers) during three months, and then power high-frequency electron tubes for five years of broadcasting. Most of the problems related to the power loss resulting from current flow between the array and the surrounding space plasma.

We postulated an array with uninsulated solar cell interconnectors, but which otherwise is perfectly insulated. Analysis of the electric field about an uninsulated interconnector and the interaction of this field with the surrounding plasma required a sophisticated digital computer program. The calculations showed that the total electron current collected by the interconnectors is about the same as the total ion current swept out by the array. At low altitude this represents a significant power loss (for example 210 watts per square meter of interconnector area at 300 km). Further analytical and experimental work is needed to provide the losses for specific voltages and altitudes.

After concluding that the high-voltage solar array must be completely insulated to avoid leakage-current power losses, we developed conceptual designs of insulated arrays. Properties of insulating materials were examined with respect to voltage breakdown, chemical interaction with the space plasma, ultraviolet radiation, and ease of array fabrication. A new 5600 volt-per-mil dielectric, Parylene C, has many characteristics that could make it useful for insulating. Insulation performance under the proper environmental conditions is not available. Proposed further work includes: (1) Use of a duoplasmatron to measure charge buildup phenomena; (2) use of a current-limiting apparatus for voltage breakdown measurements; and (3) use of laboratory plasmas to produce accelerated rates of chemical reaction.

Other work in this study included the evaluation of sputtering, mercury contamination, solar cell radiation damage, micrometeoroid damage, and array reliability. A model of the space environment, as it applies to this study, was established.

1.0

INTRODUCTION

This document reports the results of a High Voltage Solar Array Study, conducted by The Boeing Company for NASA Lewis Research Center on contract NAS3-11534. The objectives of this program were to study, define, and evaluate the design, fabrication, test, and application problems resulting from the use of a high voltage solar array.

A single application was defined for the program--a 15 kW array, producing from 2,000 to 16,000 volts dc, in six voltage steps, at one voltage, or up to six voltage and power levels. The program anticipates a spacecraft that spirals from 100 nautical miles altitude to synchronous orbit in three months, using ion thrusters, and then serves for five years as a direct broadcast satellite using high voltage electron tubes in the transmitter. The array must be capable of operating at either negative or positive potential relative to the space plasma. The array must also operate in eclipse orbits and have safeguards for personnel protection during ground handling.

To produce such an array, research and development is needed in: (1) designing and operating high voltage solar arrays; (2) regulating and switching array elements; and (3) deploying large-area arrays. This study was confined to the problems associated with the first item, designing and operating a high voltage solar array. Problems common to both high voltage and low voltage solar arrays, such as solar cell radiation damage, were treated only briefly.

A problem requiring extensive study was that of current leakage between the solar array and the space plasma. The plasmas in space contain charge carriers of both polarities, and one or the other will drift to the high voltage portions of the solar array if leakage paths can be established. Since the mobility of electrons is much higher than that of ions, an array operating at positive potentials sustains the higher leakage current. A previous study (Ref. 1) based on data from the first OGO spacecraft established that even a solar array operating at a low positive voltage (+36 volts) in Earth orbit can draw enough electron current to its exposed solar cell interconnectors to shift the spacecraft potential relative to the plasma.

Data obtained from simulated plasma experiments in a later study (Ref. 2) indicated that a solar array with exposed interconnectors maintained at a positive potential (kilovolts) while immersed in a plasma typical of low Earth orbit collected electron leakage currents representing significant power loss. Thus an objective of our study was to determine what analytical and experimental effort is needed to enable one to predict, with reasonable accuracy, this leakage current and power loss.

Other problem areas studied extensively were voltage breakdown of insulation, chemical interaction between the plasma and the array, techniques of fabricating an insulated array, and surface flashover between exposed portions of the array.

A space environment model was established and is described in detail in Appendix 4. A summary of the space environment model is provided in Section 2.0 of this report. This model provided the environmental data used in our analysis.

2.0

SPACE ENVIRONMENT MODEL

The environment for the high voltage solar array is summarized in Figure 1 where altitude is plotted in Earth radii, nautical miles and kilometers horizontally on a logarithmic scale, but with the center of the Earth brought from minus infinity to the edge of the illustration.

Dominating this region is the Earth's magnetic field, which can be represented mathematically as a tilted dipole (30 percent accuracy), off-center tilted dipole (10 percent accuracy), or multipole model (2 percent accuracy). At some 14 Earth radii on the sunward side, the Earth's magnetic field meets the solar wind, forming a bow shock wave that constrains the field to a tear-drop shape having its point in the Earth's shadow. The solar wind is a neutral plasma composed mostly of protons, but with one percent hot hydrogen atoms and lesser quantities of other atoms. Its temperature is 10^5 degrees Kelvin, it travels at 270 to 800 km per second, and it contains trapped magnetic fields of around 5 gamma (5×10^{-9} webers/m²) intensity. Between the bow shock and the magnetosphere is a magnetically turbulent region called the plasmasheath which drops down to synchronous altitude (6.6 Earth radii) only during solar events.

The Earth's magnetic field does not directly affect the high voltage solar array, but it controls other phenomena that do affect the array. These phenomena vary by orders of magnitude in intensity as a result of solar-activity induced changes in the Earth's magnetic field and particle arrival rates. For example, the ionospheric layers, of which the F₁ and F₂ are in the 100 nautical mile (NM) to synchronous-altitude operating regime, are affected not only by the magnetic fields, but also by the time of day and season of the year. During the day the ultraviolet in the sunlight ionizes the oxygen and nitrogen neutral atoms of the air, producing over 10^6 electrons per cm³ (Figure 2). At night the recombination of electrons with ionized oxygen produces the air-glow. At synchronous altitude the normal electron count falls to 100 per cm³, and 60 cubic kilometers must be swept to find a coulomb of charge. The thermal flux of electrons and the flux of ions swept out by the spacecraft are plotted as a function of altitude in Figure 3.

Ionospheric electron densities below the F₂ layer have been measured for many years with Earth-surface ionosondes, which plot as a function of frequency the time required for radio signals to echo back from the ionosphere. The echo time is converted to altitude, and the critical frequency above which no signals are reflected can be converted to ion density. The ionosphere above the F₂-peak electron density zone has been explored with rockets, satellite-mounted ionosondes which probe downward, and plasma probes. The modulation and delay time results found for ultra-low frequency (1 Hertz) whistlers echoing in the magnetospheric "waveguide" during quiet time provides the electron density data in the 2-8 Earth radii range.

Solar cell degradation is most severe in the Van Allen trapped electron and proton belts, where up to 10^6 protons of greater than 4 MeV energy bombard every square centimeter of cell area each second. The energetic protons are particularly damaging because each proton of energy over 4 MeV can penetrate a 6-mil quartz cover and produce thousands of crystal defects before coming to rest. Compared with trapped protons the galactic cosmic rays (10^8 per sq. cm. per year) produce trivial damage in solar cells.

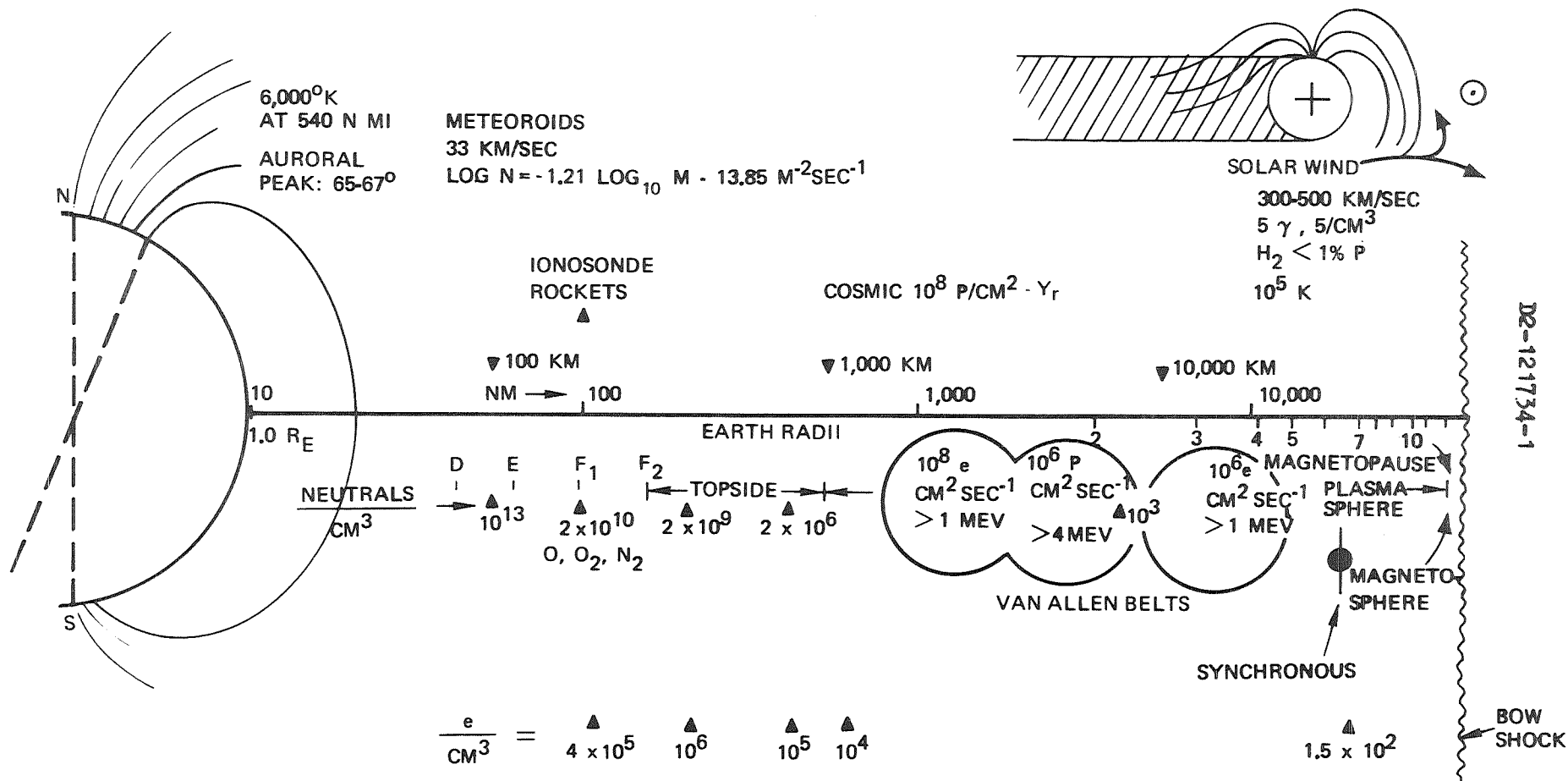


Figure 1: SPACE ENVIRONMENT

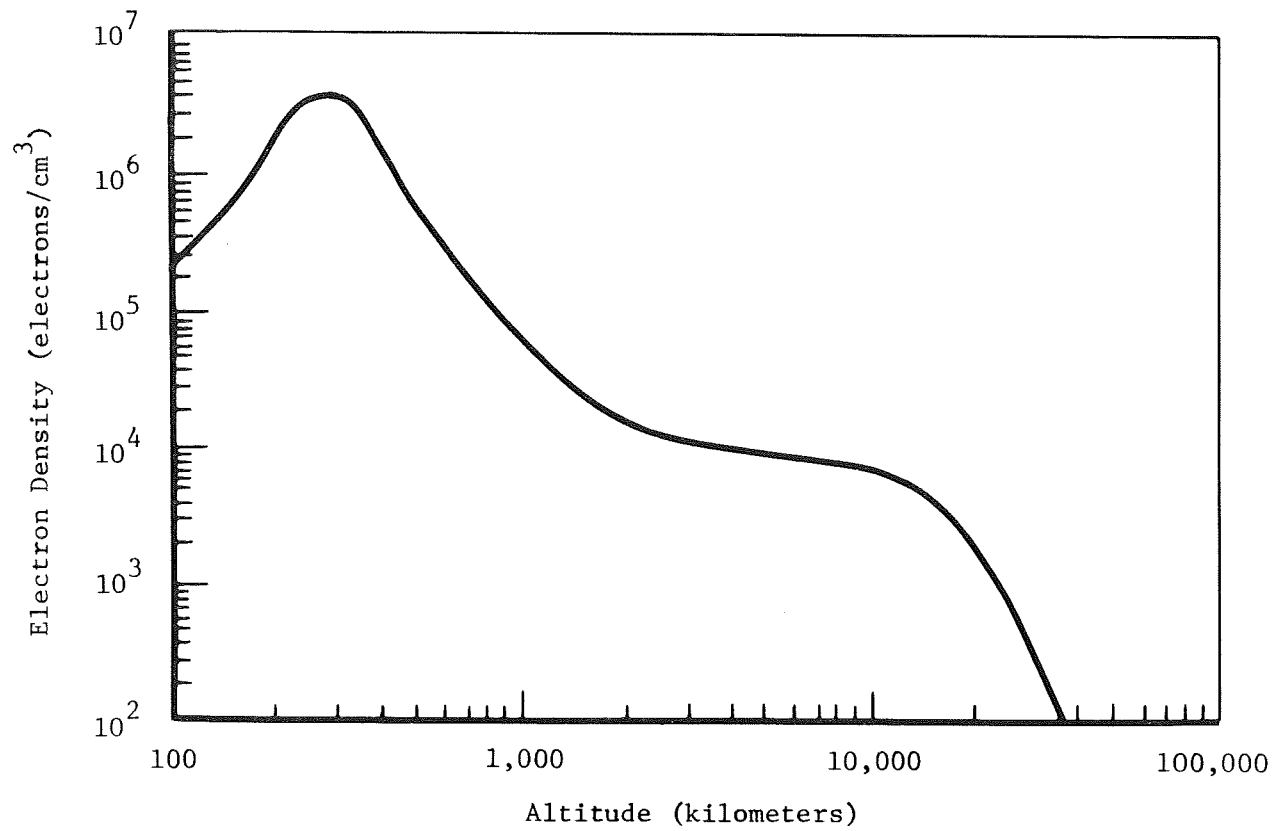


Figure 2: ELECTRON DENSITY VS ALTITUDE

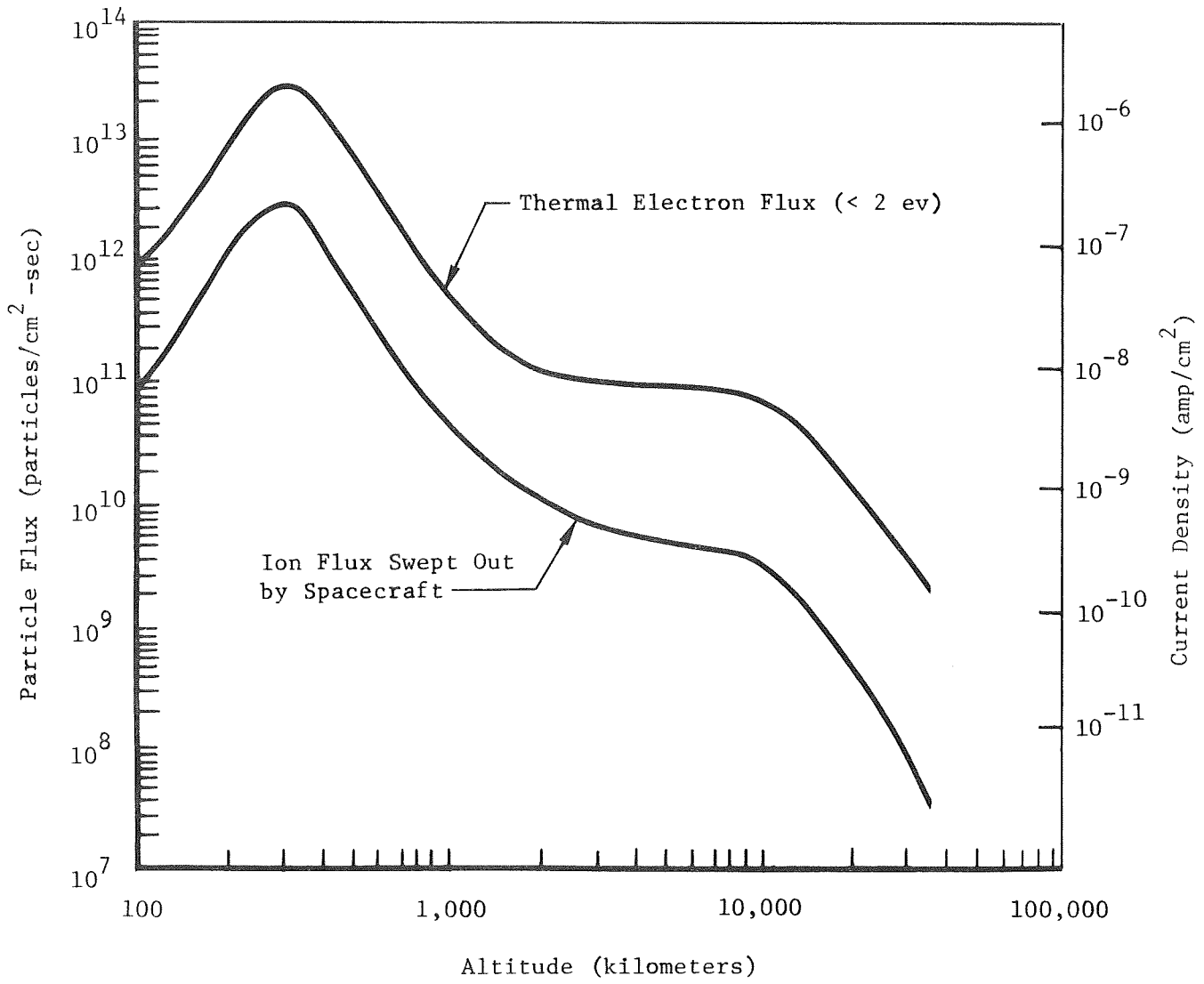


Figure 3: ELECTRON AND ION FLUX VS ALTITUDE

The polar regions, particularly the auroral peak at 65 to 67° geomagnetic latitude contain highly variable charged-particle phenomena. For example, 6000° K electrons can be found at altitudes as low as 540 NM. This temperature does not normally occur below 13,000 km in equatorial regions.

Another contributor to the solar array environment is the meteoroids, which travel at around 33 km per second with respect to the Earth, or some 17 km per second with respect to interplanetary space. Empirical equations have been developed to relate meteoroid flux to size.

The magnitudes and variations of phenomena occurring in the high voltage solar array environment are described in detail in Appendix 4.

3.0

LEAKAGE CURRENTS

Exposed conducting surfaces on a high voltage array which operates an ion thruster in Earth orbit can collect leakage current from (1) the natural space plasma, (2) the ion thruster exhaust, (3) nearby insulating surfaces which eject electrons during bombardment by photons, atoms, or ions, and (4) nearby exposed conductors via voltage breakdown on insulating surfaces. We first describe why leakage currents present a potential problem, and how power loss is affected by altitude, voltage and polarity (subsection 3.1). Then we discuss each type of leakage current individually (subsections 3.2 - 3.5).

3.1

Power Loss

3.1.1

Effect of Voltage, Altitude and Polarity

A solar array that is not completely insulated when operated in the ionosphere will lose some of its power output to electron or ion leakage currents (i.e. electrons or ions "leaking" from the plasma to the array). The greater leakage current and power loss occurs when all points on the array are positive relative to the surrounding plasma. This is because a positive-polarity array attracts electrons rather than the heavier, harder-to-collect ions.

The electrons attracted by an uninsulated 1,000-volt array having a positive polarity will fall through an average potential drop of 500 volts. The magnitude of the resulting leakage current depends on the density of plasma thermal electrons. The maximum current density from thermal electrons ($4.9 \mu\text{amperes}/\text{cm}^2$) occurs in the daytime at an altitude of 300 kilometers (Figure 3).

The array power consumed in collecting these electrons would be:

$$\begin{aligned}\text{Power loss} &= E_{\text{ave}} I_T \\ &= .00245 \text{ watts}/\text{cm}^2 \\ &= 2.45 \text{ milliwatts}/\text{cm}^2\end{aligned}$$

where E_{ave} = average potential through which thermal electrons falls
 I_T = current of collected thermal electrons

Since solar cells in Earth orbit generate about $14 \text{ milliwatts}/\text{cm}^2$, this represents a 17 percent power loss. Under similar circumstances a 16,000 volt array would lose as much power as it could generate.

Repeating the above calculation for a positive polarity array at different altitudes produced the curves in Figure 4. It is evident from these curves that the uninsulated array loses less power at altitudes above 300 kilometers. Similar curves were generated for a negative-polarity array which collects plasma ions as the spacecraft sweeps through them (Figure 4). Although the curves in Figure 4 are not intended to be design data, they do indicate that the ionosphere plasma is a potential problem in high-voltage arrays operating at altitudes below 1000 kilometers.

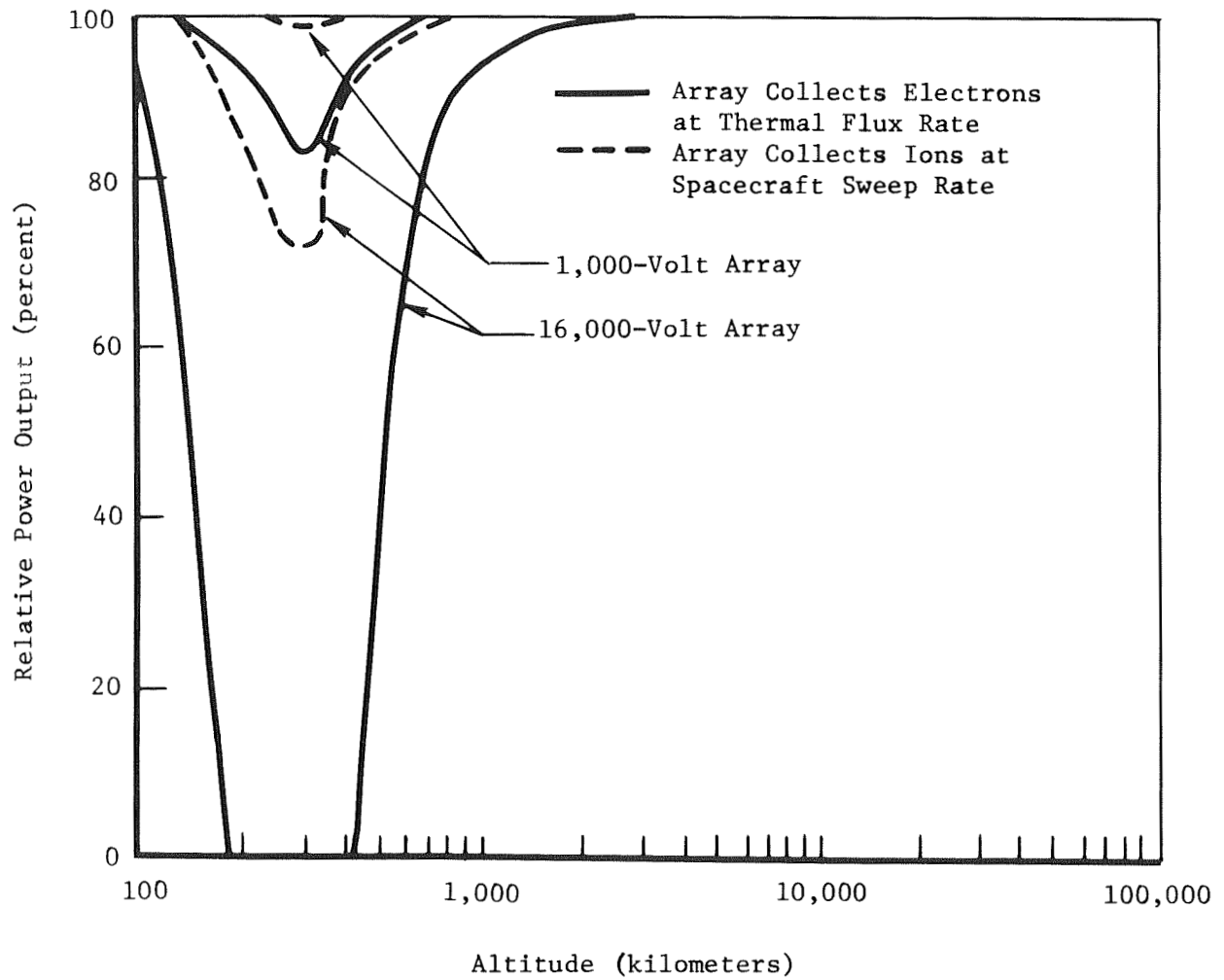


Figure 4: EFFECT OF PLASMA LEAKAGE CURRENTS ON ARRAY POWER OUTPUT

3.1.2 Effect of Operating an Ion Thrustor

When a solar array is powering an ion thrustor, only that part of the array which has a positive polarity with respect to the plasma will contribute to the thrust. Since situations can arise where only a fraction of the array has a positive polarity, the loss of useful power can be greater than indicated by Figure 4. As an example, consider a situation where the ion thrustor neutralizer emits electrons at the same rate that ions are accelerated into the exhaust beam. In order to maintain charge neutrality, the solar array must collect as many ions as it does electrons. This requires that most of the array have a negative polarity since ions are not collected as rapidly as electrons. Such an array is sometimes referred to as a "floating" array since (like an iceberg floating in water) part of it floats above the plasma potential (water-line) and part of it remains below.

For example, consider at 300 kilometers a floating array whose positive portion collects the flux of thermal electrons and whose negative portion collects the ion flux swept by the spacecraft. The collected ion-current density is only one-tenth as great as the collected electron-current density, so for charge neutrality, the positive portion of the array can only be one-tenth as great as the negative portion. In this condition only nine percent of the array delivers power usable in producing thrust. The remaining power is wasted in accelerating the electrons emitted by the neutralizer into the plasma (Figure 5).

The preceding example indicates that a serious thrust loss can occur at 300 kilometers when the neutralizer and ion-beam currents are equal. However, if the neutralizer emits an excess current equal to the electron current collected by the array, the entire array can attain a positive polarity with respect to the plasma and still maintain overall charge neutrality. Then the neutralizer, which is essentially at the same potential as the negative end of the array, attains a potential only slightly less than that of the plasma (Figure 6). As a result, very little power is lost in accelerating neutralizer-emitted electrons into the plasma. This phenomenon was confirmed during in-flight performance testing of the SERT I ion thrustor, when the difference between the potential of the plasma and that of the neutralizer was less than 10 percent of the ion-source voltage (Reference 3).

3.1.3 Effect on Solar Cell Operating Current

We have already seen that useful power can be wasted by accelerating electrons to an array where their kinetic energy is converted to heat upon impact. More useful power may be wasted because each solar cell could be required to carry a current different than its maximum power current.

Consider a completely uninsulated series-connected string of solar cells which collects electrons at all its surfaces from the plasma. If the string of cells is operating an ion thrustor, the collected electrons are re-emitted by the neutralizer which is connected to the negative end of the string. Consequently, the solar cells at the negative end of the string must carry the entire leakage current whereas the solar cells at the positive end of the string need only carry the leakage current they collect from the plasma. This means that all the solar cells do not operate at the same point on their current-voltage (I-V) curves, and each cell generates a different amount of power.

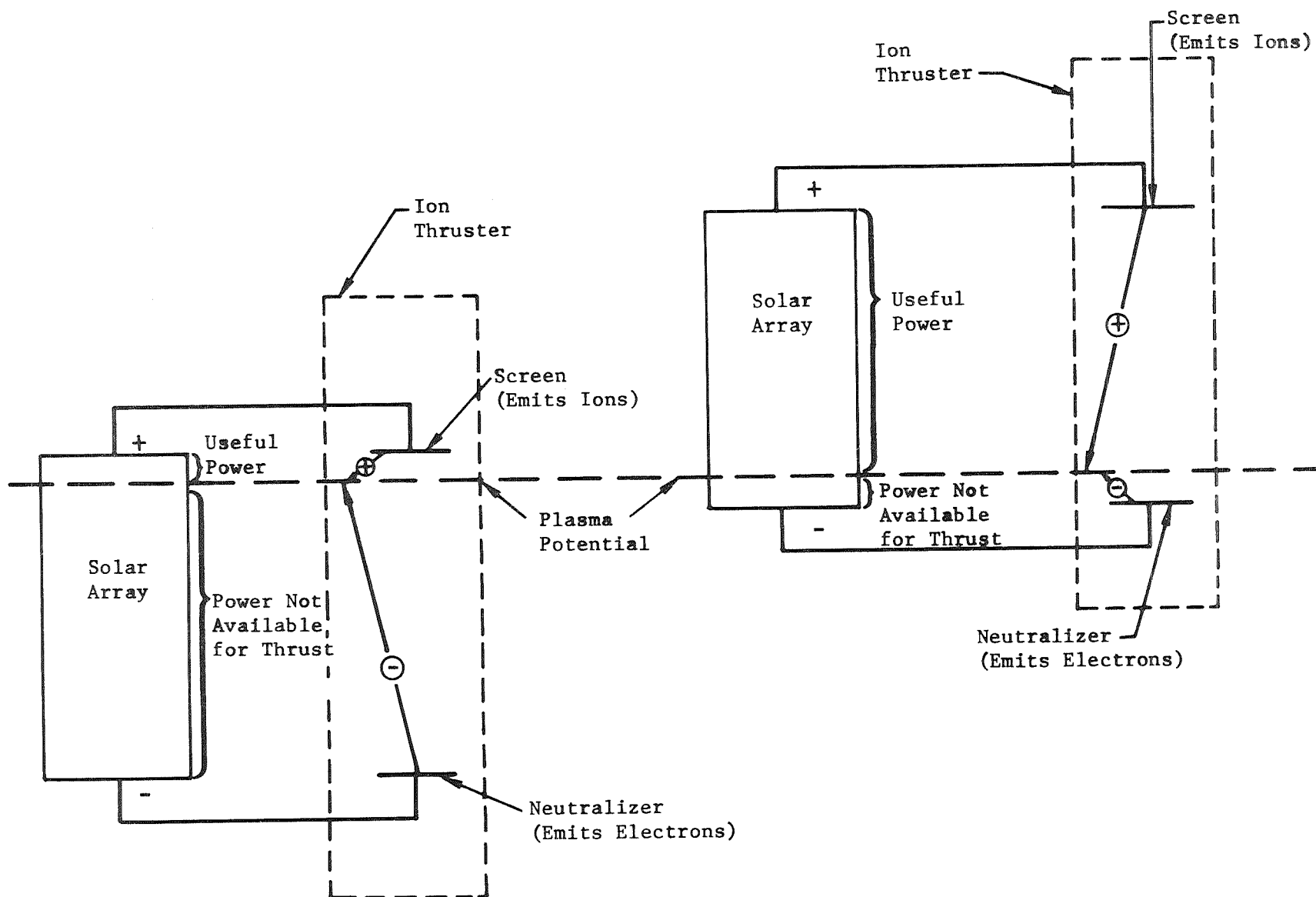


Figure 5: POTENTIAL OF A NEGATIVE-POLARITY ARRAY AND AN ION THRUSTER

Figure 6: POTENTIAL OF A POSITIVE-POLARITY ARRAY AND AN ION THRUSTER

Actually, only one cell in the string will operate exactly at maximum power. As a result, the useful power delivered to the ion thruster may be severely degraded.

To illustrate this we analyzed a situation where an array collects electrons uniformly from the plasma while operating a constant-current ion thruster which maintains its neutralizer at plasma potential. The result is shown in Figure 7 where ion-thruster power is plotted versus collected electron current density. The solar array was assumed to be designed such that, without the plasma leakage current, the array operates at maximum power. A complete discussion of the assumptions and calculations used in deriving the curve in Figure 7 is provided in Appendix 2.

An electrical designer should design his array so that most of the solar cells would operate at the maximum power point when carrying load current plus leakage current, providing this were the critical part of his mission, and providing he knew precisely how much leakage current he would have to handle. One approach is switching cells to change the number in parallel at different string locations so that more cells will operate near their maximum power point. Furthermore an ion thruster is not exactly a constant-current load, and its current variations should be considered in establishing the maximum-power voltage of the array.

3.2 Leakage Current from Natural Plasma

This section describes (1) a digital computer program which was developed to calculate the magnitude of the natural plasma leakage current, and (2) recommended future analysis and experimentation.

3.2.1 Completed Work

Presently available analytical techniques are not adequate to calculate the plasma leakage current to a high voltage solar array. Modern electric probe theory (References 4, 5), which is adequate for calculating leakage current to low voltage conductors with a simple geometry, is not applicable to complex array geometries involving high voltage. Although high voltage solar arrays have been experimentally tested for leakage current in a simulated space plasma (Reference 6), it is desirable to have good analytical data for comparison purposes. Therefore we programmed a digital computer to calculate the leakage current.

Description of Computer Program and Assumptions

The program numerically simulates the collection of electrons by a positive array having quartz-covered solar cells and exposed interconnectors. The array is assumed to be a positively-charged conducting plane partially covered by long, 2 cm-wide insulating strips (Figure 8). The gap between strips is 0.1 cm wide and 0.05 cm deep. The model analyzed consisted of the region between the center of one insulating strip and the center of an adjacent gap. The conductor is assumed to always have 500 units of positive charge distributed fairly evenly over its top surface.

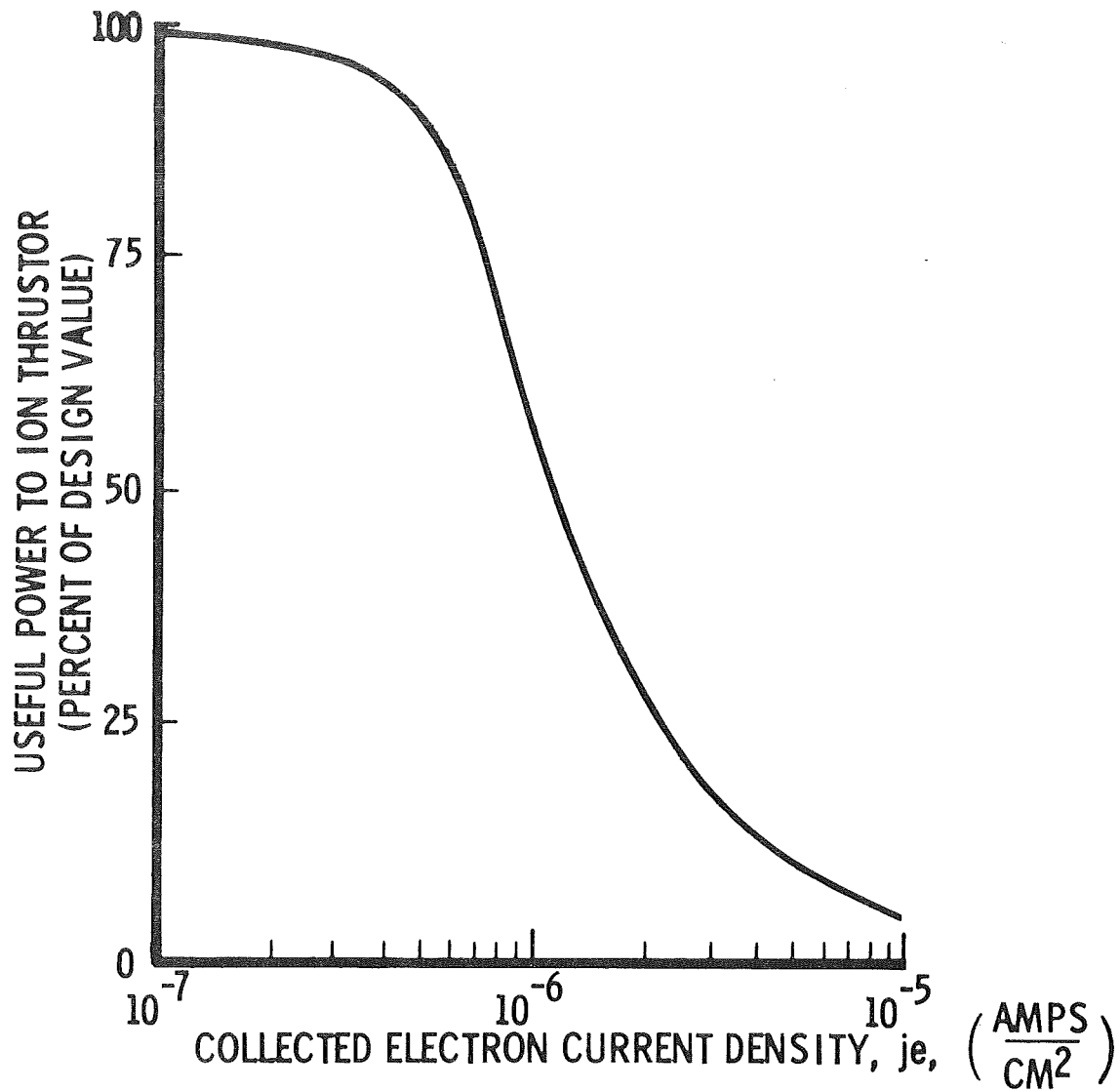


Figure 7: EFFECT OF LEAKAGE CURRENT ON POWER AVAILABLE FOR THRUST

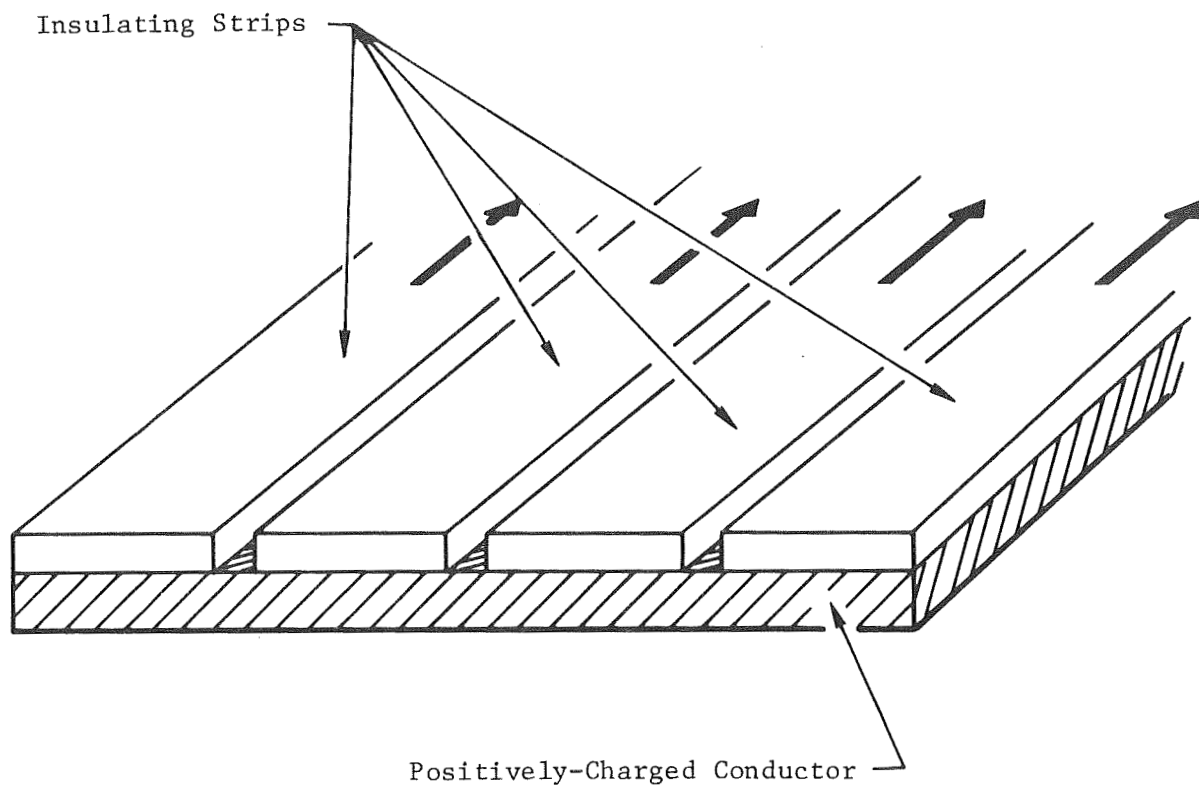


Figure 8: SOLAR ARRAY CONFIGURATION FOR COMPUTER MODEL

The computation starts at $t = 0$ with 450 units of bound negative charge distributed evenly over the insulating surface, and with the space above the strip and gap containing 2150 free individual units of negative charge having a random velocity distribution. The free negative charges are attracted to the uninsulated gap which contains 50 (i.e., 500 - 450) unneutralized units of positive charge. Motion of these free charges is solely dictated by the electrostatic forces produced by the positive charges on the conductor and the negative charges bound to the insulator surface. Electrostatic forces between free charges is neglected. Free negative charges which reach the conductor during a time interval Δt are assumed to be immediately erased so that the net positive charge on the conductor is not affected. Free negative charges which reach the insulating strip become bound. The surface and bulk conductivity of the insulation strip are assumed to be zero.

At the beginning of the next time interval, new free negative charges corresponding to those previously collected by the conductor and insulator, are introduced in the region above, with prescribed positions and velocities. In addition, 11.25 units of negative charge on the insulator are erased at the beginning of this second time interval. This erasure corresponds to an undeflected ion current arriving at the insulating surface. Iteration of 100 to 200 time intervals usually produces a fairly stable, steady state condition.

The computer program steps are listed in Appendix 1.

Results and Discussion

Computer leakage-current calculations made to date were for checkout purposes only, and corresponded to an unrealistic plasma environment. However, the important result, applicable to the ionospheric plasma, was that the electron current collected by the array at +3 kilovolts was roughly equal to the ion current density swept out by the array. Other significant results are: (1) the collected current was found to be proportional to $V^{3/2}$ where V is the voltage of the conductor relative to the undisturbed space plasma, and (2) more charge accumulated on the edge of the insulator surface than in the center. We did not analyze the case where ions cannot reach the covers due to their being reflected at the sheath. In such a case, the result that electron current equals ion current is not valid. Future computer runs can be made to correspond to a realistic plasma environment by changing selected input parameters. The use of a digital computer for numerically simulating the motion of charged particles has been used successfully by others (e.g., Reference 7) and increases our confidence in the validity of these results.

The program is not limited to electron collection at exposed interconnectors. The program with slight modifications, could be used to calculate either ion or electron leakage currents. Currents collected through pinholes in insulation could also be calculated, although a different technique may be required for a very small pinhole where the surface resistivity of the pinhole walls is important.

3.2.2 Future Analysis

The following proposed analysis will establish the magnitude of plasma leakage currents for the entire mission defined for this study:

1. Use the computer program just described to calculate ion and electron currents to exposed interconnectors on an array operated at different altitudes and different voltages. Plot the calculated leakage currents as a function of altitude for different voltage levels.
2. Repeat the above calculations for different size pinholes in the insulation, with the interconnectors insulated and uninsulated.
3. Repeat a few of the above calculations with the following refinements incorporated, one at a time, into the program: (1) Each free charge feels the electrostatic forces of all the other free charges; (2) a magnetic field influences the motion of free charges; (3) the surface and bulk conductivities of the insulation are assigned non-zero values. The results should indicate whether or not the refinements are necessary.

3.2.3 Future Experimentation

Verification of the computed leakage currents is desirable. A meaningful experiment could use the plasma source described by Burroughbridge (Reference 8), with a thin one square-foot metal test specimen completely insulated on one side and partially insulated on the other side. A sheet of aluminum with Kapton bonded to one surface could form the insulated side, and an array of 2 by 2-cm quartz covers bonded to the other surface could be the partially insulated surface. The test specimen and plasma source would have to be in a vacuum chamber. Various voltages between 2,000 and 16,000 volts, relative to the simulated plasma, would be applied to this test specimen and the resulting electron leakage current would be measured. The orientation of the test specimen relative to the plasma beam direction would be varied to determine the effect of streaming ions on the electron leakage current.

The test should be repeated with test specimens comprised of flat metal sheets covered with other insulating materials (e.g., Parylene, Teflon-FEP), and having purposely-induced defects (e.g., drilled holes).

Important considerations in the design of the complete experiment are:

1. Will the electron sheath around the test specimen be so thick that it extends to the ionization chamber of the plasma source to affect the electron current?
2. How large should the vacuum chamber be?
3. How should the plasma potential be established?
4. How low must the pressure in the vacuum chamber be to reduce ionization of neutral atoms outside the plasma source to insignificance?
5. Is differential vacuum pumping between the ionization chamber and the test volume necessary to reduce the density of neutral atoms in the test volume?

The principle equipment required is:

1. Plasma source (Reference 8)
2. Vacuum chamber, size and vacuum capability to be determined, but probably at least 6 feet long, 3 feet in diameter, and capable of 10^{-4} torr.

3.3 Electron Emissions from Solar Cell Covers

When photons, ions, or neutrals impinge upon quartz covers, electrons can be emitted by the covers and then attracted by strong electric fields to a nearby uninsulated interconnector. For an insulated array secondary emission has little importance.

3.3.1 Completed Analysis

Photoelectric Emission

The upper limit of photoelectric emission for metals in sunlight is about 10^{-8} amps/cm² (Reference 9). It thus appears that photoelectric emission is not a problem unless quartz for some unanticipated reason has a much larger quantum yield than metals.

Secondary Emission from Ions

The current density ($j_{e,i}$) of electrons emitted by solar cell covers as a consequence of ion bombardment depends upon the ion current density (j_i) and the secondary electron yield (γ_i):

$$j_{e,i} = j_i \gamma_i \quad (9)$$

The maximum value of j_i is about 5×10^{-7} amps/cm² and occurs at 300 kilometers as a result of the spacecraft orbital velocity (V_s). The electric fields from the interconnectors will undoubtedly shield the solar cell covers from at least some of the incoming ions, so that the expected ion current density will be less than this maximum value.

The value of γ_i depends upon the type of target material, the ionization potential and mass of the incoming ion, and the velocity of impact. For atomic oxygen ions (predominant ion at 300 km) incident on quartz with a kinetic energy of 5 ev (corresponds to spacecraft velocity) no published experimental data has yet been found. However, some experimental data (Reference 10) indicates that low energy (40 ev) helium ions incident upon No. 46 glass produce secondary electrons with a 25 percent efficiency (i.e., $\gamma_i = 0.25$).

Whether or not atomic oxygen ions will produce secondary electrons from quartz with a 25 percent efficiency is yet to be determined, however the first ionization potential of oxygen (13.6 volts) does exceed twice the work function of quartz (4.75 ev), which is the criterion for producing secondary electron emission by low energy incident ions.

It therefore appears that secondary electron emission from ion impact must be considered a potential problem for an uninsulated array until it can be shown that the covers are effectively shielded from incoming ions or that the secondary electron yield is much lower than 25 percent.

Secondary Emission from Neutrals

The current density of electrons ($j_{e,n}$) emitted by solar cell covers as a consequence of neutral bombardment depends upon the effective neutral current density ($j_n = N_n q v_s$) and the secondary electron yield δ_n :

$$j_{e,n} = j_n \delta_n \quad (10)$$

The maximum value of j_n at 200 km is about 10^{-3} amps/cm² and is primarily due to oxygen atoms striking the array as a result of spacecraft motion. Since these atoms are neutral, the electric fields from the interconnector will not shield the covers as in the case of incoming ions. Note that the effective neutral current density (10^{-3} amps/cm²) is about 2000 times greater than the maximum ion current density (5×10^{-7} amps/cm²). Unless δ_n is much less than δ_i , secondary electron emission by neutrals would be much greater than that due to ions.

It is concluded that secondary emission would be an important area of investigation preliminary to the design of an uninsulated array.

3.3.2 Future Work

The extent to which electron emission will enhance current flow to the array depends upon the electron yield of neutrals incident on given target materials. The objective of a useful test is to determine the electron yield of atoms and molecules striking materials at spacecraft velocities. The following materials, useful for high voltage arrays, are recommended for testing:

<u>Material</u>	<u>Thickness of 2 by 2 cm Specimens</u>
Quartz	6 mils
Kapton	2 mils
FEP Teflon	2 mils
Silver	2 mils

The apparatus used by Greene (Reference 11) in measuring secondary electron emission from molybdenum bombarded by helium, neon, argon, and hydrogen neutrals appears to be appropriate for the high voltage solar array work.

3.4 Ion Thrustor Effects

The high voltage solar array may degrade in power output because of: (1) the deposition of mercury atoms, emitted from the thrustor, onto the surface of the array; (2) an increase in local electron and ion density from ionization of mercury atoms by sunlight; and (3) attraction of electrons and ions, emitted from the thrustor, to exposed portions of the array. All three phenomena could contribute to leakage current collected by the array from the plasma, causing

added loss in electrical power output. Furthermore, deposited layers of mercury, if thick enough, could obstruct the sunlight, further reducing the power output from the solar cells.

Mercury Deposition

If mercury is deposited on the surface of the array, its high conductivity could enhance the current collection through pinholes in the cell covers and in the insulation. Thick layers (many Angstroms) of mercury would alter the optical properties of cell covers.

Reference 12 discusses the mercury condensation rates on solar panels. The rate at which a vapor condenses on a surface is determined by the difference between the arrival rate μ , and the desorption rate ν .

$$\frac{d\sigma}{dt} = \mu S - \nu$$

μ = the arrival rate particles/cm²-sec

ν = the desorption rate, p/cm²-sec

σ = the surface concentration of adsorbed species, particles/cm²

S = the sticking coefficient

The arrival rate depends on the geometry of the spacecraft and the ion thruster mercury emission rate. The desorption rate depends on the temperature of the surface and the desorption energy.

According to the Reference 12, no mercury will condense on an illuminated solar array in vacuum at one A.U. because the temperature of an illuminated array is so high that mercury evaporates faster than it condenses. However, it will be necessary to check the final spacecraft design to see if there are colder places where mercury can condense and cause trouble.

It would also be appropriate in the future to analyze the mercury condensation on cold solar panels as the ion thrusters are turned on after the spacecraft emerges from the Earth's shadow.

Ionization of Mercury

The density of ionized mercury atoms in the vicinity of the array depends upon the emission rate of neutral mercury atoms by the thruster as well as the velocity of the emitted atoms. An ion thruster having a one-ampere ion beam and a 90 percent utilization efficiency, would emit 7×10^{17} neutrals/sec, according to the following equation for neutral atom emission rate:

$$n_a = \frac{J}{q} \frac{(1 - n)}{n} \times 10^{-4} = \frac{I}{(\pi r^2) f} \frac{1 - n}{n} \times 10^{-4} \quad (11)$$

I = ion beam current, amps

J = ion beam current density, amp/cm²

r = thruster radius

q = electron charge, 1.6×10^{19} coulomb

n = propellant utilization efficiency

n_a = neutral particles/cm-sec

If the emitted particles have a thermal energy of 500°K (200 meters per second) and there are no collisions, the average density of mercury neutrals in a 10-meter radius hemisphere centered about the thruster nozzle is 8.3×10^6 atoms/cm³. Multiplying this density by the ionizing solar flux (4×10^{11} photons/cm²-sec) and the estimated ionization cross section of mercury (10^{-18} cm²), we get 3.3 ions/cm³-sec as the average ion production rate of mercury ions in the vicinity of the spacecraft, neglecting recombination. Since each ion only spends 0.05 seconds in the postulated hemisphere due to its 200 meter/second velocity, the average ion density is only 0.16 ions/cm³.

This average ion density is slightly less than the expected proton density at synchronous altitude and much lower than the ion density expected in low-Earth orbit. Thus, ionization of the neutral mercury is not expected to be significant.

More detailed calculations of mercury ion density should be made when the spacecraft is being designed, keeping in mind the distance between thruster and array, and the variation of ion density with distance from the thruster and with the emission angle.

It would be necessary to be less than one meter from the nozzle before the ion densities would approach those from other sources in a low-Earth orbit.

Leakage Current Between Array and Ion Beam

If the space plasma can sustain electric fields between exposed portions of the array and the ion thruster exhaust beam, electrons or ions emitted by the thruster could be attracted directly to the array. Whether or not the plasma can sustain electric fields over the required distances depends upon the altitude of operation and the distance and orientation of the array relative to the exhaust beam. The distance that electric fields will extend from an array with uninsulated interconnectors cannot be calculated from modern electric probe theory, however it is believed that this can be determined in the future from the computer program and experimentation described in Section 3.1. It appears unlikely that the plasma can sustain electric fields as far as several meters from the array at low altitude because of the high electron densities. However, the space plasma becomes less dense at altitudes near synchronous orbit, and electric fields between the array and the ion beam may be possible.

An upper limit of the possible leakage current at high altitude, for a 6 meter separation of array and ion exhaust, was obtained by assuming that the ion beam is a hot, thermionic-emitting sphere with a 15 cm radius, and the array is a concentric, spherical, conducting shell with a 6 meter radius. The electron current density (j_e) collected by the array can be calculated from the space-charge equation for spherical collectors (Reference 13):

$$j_e = 29.4 \times 10^{-5} \frac{V^{3/2}}{r^2 a^2} \quad (\text{amps/cm}^2) \quad (12)$$

where

V = voltage (volts of array relative to neutralizer)

$$a^2 = \gamma^2 - 0.6\gamma^3 + 0.24\gamma^4 - 0.074\gamma^5 + \dots$$

$$\gamma = \ln \frac{r}{r_0}$$

r = radius (cm) of outer sphere (array)

r_0 = radius (cm) of inner sphere (neutralizer)

Using the values $V = +3000$ volts, $r_0 = 15$ cm, and $r = 600$ cm we find that $r/r_0 = 40$, $a^2 = 2.94$ and $j_e = 3.63 \times 10^{-7}$ amps/cm².

Since this calculated value of j_e is for a worst-case geometry, the actual leakage current density can be expected to be far less, especially if the array is partially insulated.

It would be appropriate in the future to adapt existing digital computer programs, which numerically simulate current collection, to this current collection problem once specific array geometries are known.

3.5 Electrical Breakdown and Leakage Currents on Insulating Surfaces

Electrical breakdown on the insulation surface can occur unless outgassing operational procedures are used during test and deployment.

3.5.1 Completed Analysis

Breakdown strength on the surface of the insulating surface is a function of the voltage gradients, electrode geometry and surface resistivity at the gas-solid interface. The solar array ambient gas density at operational altitudes will be much below that which will allow impact ionization and electron avalanche. However, polymeric insulations will have occluded gas and moisture. Polyimides, for example Kapton, have approximately 1.3% absorbed moisture after storage at 50% relative humidity. This moisture is bound to the polymer chain and is released slowly in a space-vacuum environment. In addition to moisture, all components of air are available during the outgassing period. If the pressure at a surface reaches the critical value a flashover can occur.

Fused silica cell covers were studied in detail. The bulk resistivity of fused silica is 5×10^{18} ohm-cm and the surface resistance is 10^{16} ohms per square in air. When an interconnector is exposed to the plasma a current will flow along the edge of the cell cover to the interconnector. This current flow will be approximately 10^{-10} amps with 16 kV applied across 0.006 inch (0.015 cm) thick, 2 cm wide cover slips. However, much larger leakage currents are expected from the cover slip to the interconnector through the plasma and sheath region due to secondaries. Therefore, this relatively small current will relieve voltage gradients, but the effect of this leakage current on the plasma leakage current appears to be small.

The cover surface will be oxidized and ionized by the plasma, contaminated by the neutral mercury during operation, and also with hydrocarbons during fabrication and test. These factors would make the surface resistivity less than 10^{16} ohms/square. Conversely, space vacuum will remove contaminants and increase the resistance.

Although understanding of surface conductivity has increased significantly in the past 10 years available information does not enable reliable prediction of surface conductivity variation versus time into the mission (Reference 14).

3.5.2 Proposed Experiments

Objective: To establish design factors relating electrode separation outgassing, insulation surface breakdown and leakage currents.

Description of Test Samples:

Test samples must have the geometry, electrode and dielectric materials anticipated for the array. Electrode materials are silver, copper, molybdenum, aluminum, and tin-lead solder. Typical dielectric materials tested should be fused silica, polyimides, poly-p-xylylene, silicones, epoxy, and fluoro-ethylene-propylene.

Test Apparatus:

A space effects test facility would be required which includes the following:

- Ion source
- UV-optical monochrometer
- Electron-paramagnetic-resonance measurement apparatus
- Vacuum chamber 10^{-7} torr
- Array deployment simulator (to provide controlled rate of exposure of samples of environment)
- Mercury contamination chamber
- Direct voltage source, 0-32 kV
- Current, voltage and ionization detection apparatus

4.0 ENVIRONMENTAL EFFECTS

4.1 Chemical Effects of Plasma

The chemical effects of plasma are the most severe at 185 km (100 nautical miles) altitude where electrons and ions of oxygen, nitrogen, helium and other species prevail. As synchronous altitude is approached, the chemical effects of plasma cease to be significant. Oxygen atoms having a kinetic energy of about 4.3 electron volts are the significant component at 185 km. They oxidize surfaces of polymers, adhesives, and metals. They cannot reach the silicon of solar cells, and they do not affect quartz. Quantitative data on degradation of polymers and adhesives at 185 km is lacking; however, data from higher-pressure tests suggest plasma-resistant materials that need to be tested under more applicable conditions.

Completed Analysis

The search for better surface properties for materials has motivated extensive studies of the reaction of plasmas with both organic and inorganic surfaces. Many results of these laboratory studies are applicable to the anticipated operating environment of the high voltage solar array. However, the high voltage is unique in that it can (1) enhance or retard the rate of ion arrival depending on the polarity of elements relative to the external plasma, and (2) accelerate ions so that they penetrate deeper. With respect to polymer materials (epoxies, polyimides, polyesters, etc.), this latter effect has not been studied extensively in recent years.

The spacecraft encounters the most severe environment at its lower altitudes. For example, at 200 km (108 nautical miles), the density of particles is about 10^{10} cm^{-3} . With a satellite velocity of 7.4 km sec^{-1} , about $10^{16} \text{ atoms cm}^{-2} \text{ sec}^{-1}$ will be swept out by the spacecraft, and N or O atoms in the plasma at 200 km will be the most troublesome reactive agent. Nitrogen, helium, argon, and lighter species are not nearly so reactive as oxygen. Oxidation resistance is thus an important criterion in selection of materials. At higher altitudes, oxygen ion and atomic reactions with materials will progressively diminish and become less of a problem. Proton and helium ion species predominate at higher altitudes but their concentrations are very low at synchronous altitude.

Metals

Oxygen containing plasma will thicken the oxide on metal surfaces such as exposed solar cell interconnectors. We could find no quantitative data showing how a positive or negative bias enhances oxidation of metals in plasma. Information about the effects in metals from bombardment by ions other than oxygen and by neutral particles is available from sputtering and ion implantation experiments using non-reactive plasmas such as argon (Reference 15).

High energy penetrating ions can produce these defects or disturbances in metals, alloys, and other conductors:

1. Ions can impinge and backscatter depending on the angle of the incident ion trajectory.
2. Ions can penetrate and produce defects which enhance hole-electron combination.
3. Ions can form interstitial solutions which sometimes cause embrittlement, for example, with H^+ ions.
4. Ions can penetrate and replace some sites in the substrate lattice, forming a substitutional solution.
5. Ions can form in solid "clusters," where the surrounding atoms form a different ordered array.

Colligan studied the effect of ion energy on depth of penetration. Table 1 taken from his work, shows penetrations up to thousands of Angstroms. Such depths in metals are too shallow to compromise bulk mechanical or electrical properties. Local heating could affect insulator - metal bonds if ion bombardment rates were high enough; however, the ion arrival rates in the high voltage solar array will be orders of magnitude too low to produce significant heating.

It appears at this time that the plasma will produce only surface effects on metals on the high-voltage solar array. Experimental work with metals will become necessary only if the final array design is such that changes in metal surface characteristics such as reflections or emittance affect the performance of the high-voltage solar array.

Insulation

Polymer insulation may be required to protect solar cell interconnectors from the plasma at low altitudes. There also is the possibility that polymer insulation will be used to cover the entire front and back surface of the solar array. To avoid chemical attack by active plasma species, insulating materials should be chemically resistant to oxidation. The list in Appendix 3 indicates materials which can be considered. Candidate polymers for insulating the backside of the array, as well as acting as the solar cell substrate, are polyimide (Kapton) and polyethylene terephthalate (Mylar). Hanson (Reference 16) shows that polyimide is more stable to atomic oxygen than polyethylene terephthalate by a factor of 1.5.

The effect of atomic oxygen at low altitudes on polymer materials in general can be represented by the following sequence of reactions. R represents the remaining polymer chain.

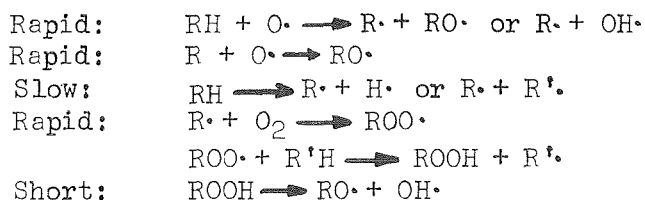


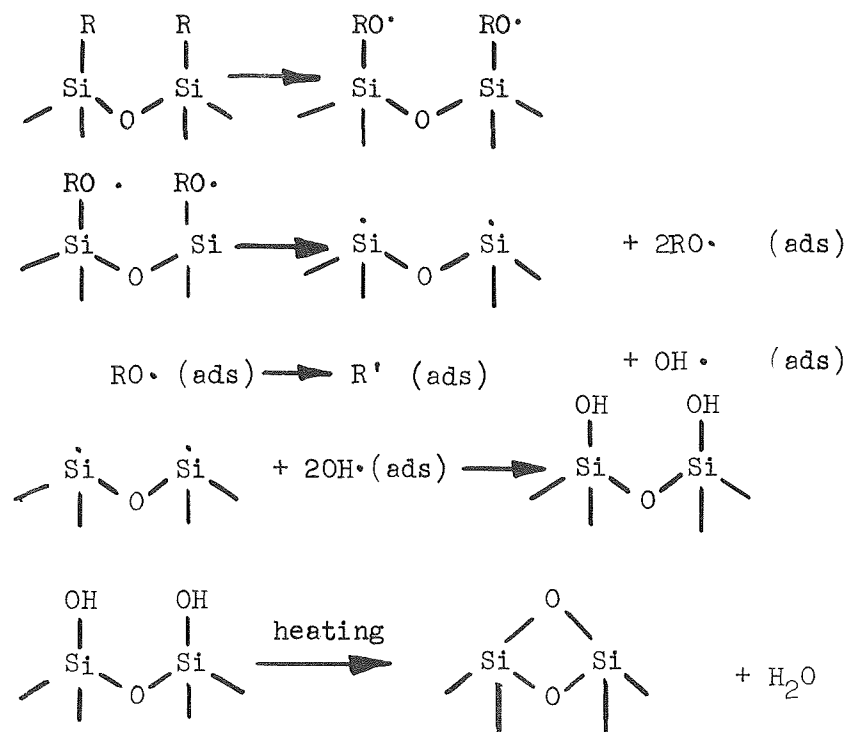
TABLE 1: PENETRATION DEPTH OF ACCELERATED IONS

Penetration depths normalized to 1 keV for various gas-metal combinations

Bombarding ion	Target Material	Energy Used (keV)	Depth/keV (A units)
Ne	Silver	60	1.7
H or H ₂	Aluminum	1-25	200
He	Aluminum	1-25	150
			80
H			40
H ₂			90
He	ZnS:Ag powder	20	50
Ne	Phosphor		25
N ₂			25
A			
Ce ¹³⁴ +Ce	Germanium	4	250
Kr ⁸⁵	Nickel	0.15	51,000
N ₂	Ilford C-2 Emulsion Film	20,000	6.5
He	Cu ₃ Au alloy	4	10
A			10
Xe			10
A	Tungsten	2	25
Rb ⁸⁶	Aluminum	30	37
Na ²⁴			61.7
Cs ¹³⁷			61.7
H ₂	Quartz	5-60	117
He			121
Ne			19
A			18
Kr			15
Li	Aluminum	1-2	10
A	Molybdenum		4.1
	Tungsten	1.7	5.0
	Platinum		3.2
A	Tungsten	1	4.75
He	Single crystal Silicon	30	300

The surface region (100-10,000 Å) of most polymers thus oxidizes rapidly, forming peroxy, hydroperoxy, or alkoxy groups. It is difficult to predict quantitatively with available data the extent of surface oxidation to be expected in the space plasma environment. The surface resistivity will probably drop because of increased electron density at the surface. This introduces the possibility for conduction paths generated by high voltages, promoting surface breakdown.

The surface oxidation predominates with hydrocarbon backbone polymers. With silicone polymers another type of atomic oxidation sequence can take place, as shown below.



This sequence is suggested by infrared measurements after atomic oxidation of dimethylpolysiloxane. The final result is SiO₂ on the surface of the silicone insulator or adhesive, a layer that should display high surface resistivity.

Surface resistivity data on materials oxygenated in vacuum are scarce. The degree of lowering of surface resistivity and its influence on surface conductivity and breakdown have not been investigated.

The effect of excited oxygen on various polymers is indicated in Table 2. Here rates of oxidation are expressed in grams/cm²-min x 10⁴ and the O atom concentration is estimated to be between 10¹⁶ and 10¹⁷ cm⁻³, a value considerably higher than will be found at altitudes above 100 nautical miles. Many polymers exhibit surface cracking when exposed to atomic oxygen at 1.0 torr for several minutes under mechanical stress. The cracks develop in the surface, and these will multiply. In a polyethylene surface, for

Table 2: EFFECT OF ATOMIC OXYGEN ON POLYMERS

	Rate of weight loss g. X 10 ⁴ /4.84 cm ² /min*
Low-density polyethylene	2.48
Irradiated low-density polyethylene (1 Mrad)	2.77
Irradiated low-density polyethylene (10 Mrad)	3.41
Irradiated low-density polyethylene (105 Mrad)	4.12
Chemically crosslinked low-density polyethylene	3.31
Low molecular weight highly branched polyethylene	3.26
High-density ethylene-butene copolymer	3.09
Polypropylene	3.45
Polybutene-	3.56
Chlorinated high-density polyethylene	5.00
Chlorinated polyethylene plus 10% polysulfide polymer	2.90
Natural rubber	3.39
Natural rubber-sulfur raw stock	1.20
Natural rubber-sulfur vulcanizate	0.16
Natural rubber-peroxide raw stock	2.99
Natural rubber-peroxide cured	1.67
Commercial hard rubber	2.71
Vulcanized ethylene-propylene rubber	0.20
Polystyrene	1.26
Poly-3-phenyl-1-propene	1.43
Poly-4-phenyl-1-butene	1.67
Polyvinylcyclohexane	2.28
ABS polymers, several types	2.68
Unplasticized poly(vinyl chloride) copolymer	4.71
Poly(vinyl fluoride)	2.54
Polytetrafluoroethylene	0.62
Perfluorinated ethylene-propylene copolymer	0.44
Poly(methyl methacrylate)	2.14
Polyimide	1.19
Polycarbonate	2.59
Poly(ethylene Terephthalate)	1.82
Nylon 6	2.77
Nylon 610	3.24
Formaldehyde polymers	5.77-7.85
Polysulfide (chloroethyl formal disulfide)	19.45
Cellulose acetate	5.00

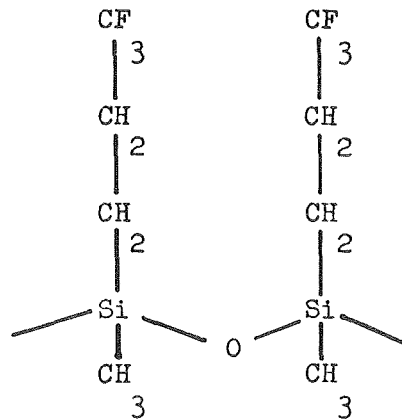
*Low Power, Tracerlab LTA-500A

example, the cracks range from 0.1 to 0.01 inches in size. However, in the high-voltage solar array the insulator materials may not be stressed after deployment at 100 nautical miles, nor is the oxygen pressure anywhere near one torr. Further analysis and testing is required after array materials have been selected and the mission profile has been established. The previous laboratory experiments have not been conducted at the applicable oxygen pressure and exposure time.

Other atomic and ionic species, such as N, H, and possibly NO, in the upper ionosphere, should produce no significant effects compared to those expected from atomic oxygen.

Adhesives

For a roll-out array, the adhesive between the solar cells and structure has to be flexible as well as inert to plasmas, and has to withstand cycling of temperature. These requirements eliminate many oxidation-resistant high performance polymers. The most promising elastomeric adhesives for this application are the inert fluorosilicones having the general formula



No polymer will be flexible at the lowest temperature expected; however, the fluorosilicones have about the best low-temperature characteristics presently available.

Adhesives used in the high voltage solar array are normally shielded from the plasma by the materials they are bonding together. However, if the final array design includes electrically stressed adhesives exposed to plasma, then the adhesives should be subject to the same selection and testing procedure as other polymer insulation.

Cell Covers

There appears to be no problem associated with chemical interaction of the plasma with SiO₂ solar cell covers. Quartz tubes are used for plasma reactors in the laboratory, and quartz appears to be quite stable in a variety of activated gas plasmas.

Future Analysis

The effect of the ionospheric plasma on polymer materials in vacuum can be measured reasonably well in the laboratory. Although the simulation experiments will probably involve plasmas of greater density than encountered in space even at 100 nautical miles, the result can be extrapolated to the long exposure times.

It will be important to take selected polymers which have been formed into model insulators and observe them for stress cracking and high voltage surface conductivity. This information will support quantitative predictions for mechanical and electrical reliability of insulators.

Proposed Experiments

The effect of oxygen and oxygen/nitrogen plasmas on polymer materials used as insulators, adhesives, and substrates in a high voltage situation needs investigation. Precise simulation of the space plasma environment may not be possible in the laboratory, however the result should be an accelerated worst-case material degradation measurement for lower altitudes. Data required for evaluating materials reliability and structural performance is outlined in Table 3. Specimens with and without mechanical defects should be tested in plasma at zero and higher voltages.

TABLE 3:

Characteristic	No Defects		Defects	
	No Voltage	Voltage	No Voltage	Voltage
Surface Resistivity				
Adhesion				
Stress Cracking				
Insulation Integrity				
Interconnectors				

Candidate substrate materials may need to be tested in their bonded configurations in an oxygen-plasma environment.

The plasma parameters can be varied to some extent to evaluate the effect of altitude. The resulting materials performance data will provide the design allowables necessary for final design.

Facilities Required

For materials evaluations the following facilities are needed:

- Radio frequency generator, 0-500 watts
- Impedance matching network
- Plasma reactor, including sample chamber
- Vacuum pumps
- Gas flowmeter, control devices, regulators, and pressure gauge.

4.2

Ultraviolet Effects

The effects of ultraviolet (UV) radiation on metals, semiconductors, and insulators has been summarized by Jaffee and Rittenhouse (Reference 17). Ultraviolet reflecting coatings have been developed for solar cell covers to prevent cell-to-cover adhesives from becoming opaque in space. Solar cells with integral glass and quartz covers avoid the problem of UV degradation of the cover adhesive. However, integral covers thick enough to protect cells for 5 years from synchronous orbit protons and electrons are not practical at this time (1970). Ultraviolet resisting paints are used where thermal emittance must be controlled on conventional solar cell arrays.

The high voltage solar array is more vulnerable to surface leakage on insulating surfaces than a low voltage array; hence, it is appropriate to examine the effects of UV light on insulating materials.

Completed Analysis

No extensive alteration of surface wettability, surface cracking, or of electrical characteristics results from UV interactions with polymers. The most serious UV effect may be the compromise of mechanical properties in bonded or other structures. These mechanical effects may ultimately be manifested only under high voltage stress. Insulators and other polymer components may lose modulus or become slightly more brittle after prolonged UV exposure. It may be possible to design the high voltage solar array in a manner that will avoid mechanical and electrical stresses in the surfaces of polymers exposed to UV. Any UV degradation investigation should obviously be based on the stresses that will probably be encountered.

Organic materials can receive ionizing doses of 10^8 to 10^{11} joules/kilogram-year when exposed to 100 to 1000 Å wavelength UV in sunlight in surface layers 10^{-6} to 10^{-7} meters deep. Such doses will in time severely damage the surface region of all known polymers particularly silicones. As a consequence of cross-linking-type reactions the elasticity of the polymer is in time reduced, and embrittlement can occur to the point where the surface will flake or fracture when under mechanical stress.

Films of commercial phenyl silicone, vinyl chloride, and methyl methacrylate undergo in a few days appreciable crosslinking when exposed to the UV of simulated space sunlight at 70°C. Such materials as polytetrafluorethylene and polyethylene terephthalate (Mylar) are severely discolored and lose significant mechanical strength and elongation or flexibility after exposure to the equivalent of a few weeks to space sunlight.

The substrate presents three aspects with respect to UV degradation:

The dark side of the substrate, which must present a high-emittance surface to space to keep the solar cells cool, would normally see little UV.

The substrate areas under the solar cells see no UV.

The substrate areas not covered with cells are exposed to UV unless protected. These areas can be weakened mechanically and perhaps electrically particularly if the array is re-rolled and re-deployed.

The exposed substrate material will be subject to UV degradation. Again, unless long term degradation adversely compromises substrate flexibility and modulus, there is no problem not already recognized for substrate polymers of conventional low-voltage arrays. If, however, the long UV exposure alters the polymer modulus, cracking may be encountered when the substrate is rolled up, altering high voltage stresses.

Future Analysis

Any analysis of the UV stability of materials should include all wavelengths between 100 and 1000 Å. Most of the available data on UV effects on polymers relate to wavelengths between 1000 and 3000 Å. Further testing is required to determine the effect of the lower wavelengths.

Candidate insulating materials should include polymers with UV stabilizing additives. Polymer degradation may be prevented or impeded by additives which serve as UV stabilizers. A suitable additive must (1) compete effectively for all the UV wavelengths--not just those observed on Earth and (2) the additives must themselves not interfere with the engineering properties of the materials.

"Blooming" or segregation of additives to the surface has been observed in a high vacuum. UV stabilizers have not yet been used in polymers for space; however, factors of 3 to 10 improvement in UV stability have been observed with current additives. A new class of UV stabilizing additives uses a nickel complex which rather than absorbing UV transfers the UV energy in a manner that avoids the effects of UV.

Opaque coating can also be considered if UV turns out to be a problem. Evaporated aluminum, a successful coating on a polyethylene terephthalate film, unfortunately presents a conductive surface.

Proposed Experiments

Ultraviolet testing is not critical with respect to establishing feasibility of the high voltage solar array. However, the ultraviolet 5-year resistance of any new electrically stressed polymers exposed to UV will have to be established prior to final design of the spacecraft.

Facilities Required

Combined vacuum and ultraviolet are essential in any simulated space environment tests for UV durability. An important UV degradation mechanism is the loss of gas freed from bonds by the UV photons. In ambient Earth-surface air pressure, the released gas, particularly if it is oxygen, immediately recombines with the surface, and the true degradation is not observed.

The required chamber, with ion pumps capable of achieving 10^{-10} torr of vacuum, is readily available. However, a solar simulator capable of producing ultraviolet radiation down to 100 Å is not available and may require development.

Ion Bombardment Effects on Cell Covers

Operation of the solar cell array at high voltage in a low Earth orbit (190 km) can result in ion interactions on the cover glasses, degrading the panel. It is anticipated that the cell covers will be bombarded with low energy ions (1 to 15 keV) at fluxes as high as 8×10^{10} ions/cm²-sec. Oxygen ions will be the predominant species, and their energy depends on electrostatic charge buildup on the surface of the covers. Calculations show that these ions could remove by sputtering the anti-reflection coating from the cell covers in as little as 4 to 5 months. Removing the anti-reflection coating reduces the light transmitted through the cover glass (or increases the reflectance loss) by about 3 percent.

The objective of further studies will be to verify the significance of the sputtering problem, and to develop techniques for minimizing it. This requires both analysis and experimental work. The analysis will include: (1) Development of a model for ionic bombardment species, energies, fluxes, and angles of incidence as a function of time and altitude; (2) calculation of the electrostatic charge buildup on the cell cover surfaces and its effect on ion energy; and (3) calculation of the rate of removal of the anti-reflection coating and the loss in cover transmission as a function of time in space. Experimental work will include: (1) measurement of sputtering yields (atoms removed/incident ion) for oxygen ions impinging on MgF₂; and (2) evaluation of techniques for minimizing sputtering.

5.0

INSULATION BREAKDOWN

High voltage gradients at voids in polymeric insulation and solar cell covers can degrade the performance of the array by promoting voltage breakdown with subsequent increased leakage current and power loss.

5.1

Completed Analysis

A voltage of 16 kV between the plasma and the array conductors will produce a gradient of 2700 V/mil (10^6 V/cm) in 6-mil array insulation. Voids and defects in the insulation generate local electric field gradients that are higher than exist in homogeneous insulation.

A field of 10^6 V/cm is within an order of magnitude of the intrinsic dielectric strength of the insulating materials considered. Will the intrinsic strength be achieved? The answer depends upon the dielectric strength, dielectric constant and conductivity of the insulation as well as its geometry. According to the Kilpatrick criterion, breakdown is possible across a 6 mil vacuum gap when fields exceed 3×10^5 V/cm. (Reference 18)

$$W_4 E_K^2 \text{EXP} (-K_{18} E_K) = K_{19} \quad (13)$$

or

$$E_K^3 \text{EXP} (-1.7 \times 10^5 E_K) = 1.8 \times 10^{14} / d \quad (14)$$

Where E_K = Field Strength, V/CM

d = Gap Width, cm

W_4 = Maximum Energy of a Particle at Electrode Surface, ev

$$K_{18} = 1.7 \times 10^5$$

$$K_{19} = 1.8 \times 10^{14}$$

In order to estimate the probability of approaching intrinsic breakdown of the insulation in the ionosphere, we must know the fields in the insulation in and near the surface regions. There is some confidence in our understanding of the surface region of silicon/vacuum and SiO_2 /vacuum, and hence, the initiation of breakdown in voids when the array is operated negative with respect to the plasma. However, with the array operating positive the plasma/insulation interface becomes most important. Mercury layers deposited by the thruster would simplify calculations in the interface problem, but it is still far from a classical cathode. Field emission theory cannot be applied to the plasma. For example, the cold emission from the plasma is important in predicting breakdown but emission data are not available. It is not known whether the inability of the plasma to support strong fields significantly affects its emissive properties.

A satisfactory qualitative understanding of the surface region of the plasma electrode is not presently available. ASTM test procedures do not apply. There is very little data on insulation breakdown strength in a vacuum and none in which the cathode is a dilute plasma.

We postulate that the plasma "electrode" will limit current and permit only non-destructive breakdown as observed by Riehl (Reference 19). Repeating Riehl's experiment for the insulation materials and thicknesses we are considering would be valuable.

The probability of gas-filled voids increases with increasing insulation thickness. Evacuated voids can be present also. The Kilpatrick criterion, with "d" being the diameter of void, can be used to estimate critical void sizes. This criterion depends upon void geometry, and can be applied to spherical voids. Using the diameter, the longest acceleration path in the void, for the gap width, gives $d = 0.0003$ inch (7.5×10^{-4} cm) for 10^6 volts/cm applied fields. The other vacuum gap criteria (Cransberg, Slivkov, and Maitland) give larger critical void sizes (Figure 9).

Very thin insulators, 10^{-5} inch (2.5×10^{-5} cm) can have breakdown strengths greater than intrinsic because of the finite probability of escape of uncollided electrons (Reference 20). However, there is no practical way to use this phenomenon because contact with a second layer reduces the escape probability. However, layered insulation would solve the void-size problem.

Emission Current

The emission current influences breakdown. When low, it provides a current limitation and when high, space charge increases the fields at the emitter, but also increases the retarding field in the dielectric. Fowler and Nordheim (Reference 21) analyzed the field emission current, j , from a metal cathode surface through the tunneling mechanism and obtained:

$$j = \frac{4 \sqrt{W_1/e\phi}}{(W_1 + e\phi)} \cdot \frac{e^3 E^2}{8 h e \phi} \exp \left(\frac{-8 \pi \sqrt{2m} (e\phi)^{3/2}}{3 h e E} \right) \quad (15)$$

where $e\phi$ = The Thermal Work Function of Electrode Materials

Thermal Work Function

Tin	4.38 ev
Lead	3.97 ev
Copper	4.89 ev
Aluminum	4.08 ev
Silver	4.73 ev
Molybdenum	4.20 ev

W_1 = The Fermi Level

E = Field Intensity at the Emitter

h = Planck's Constant

e = Electron Charge

m = Electron Mass

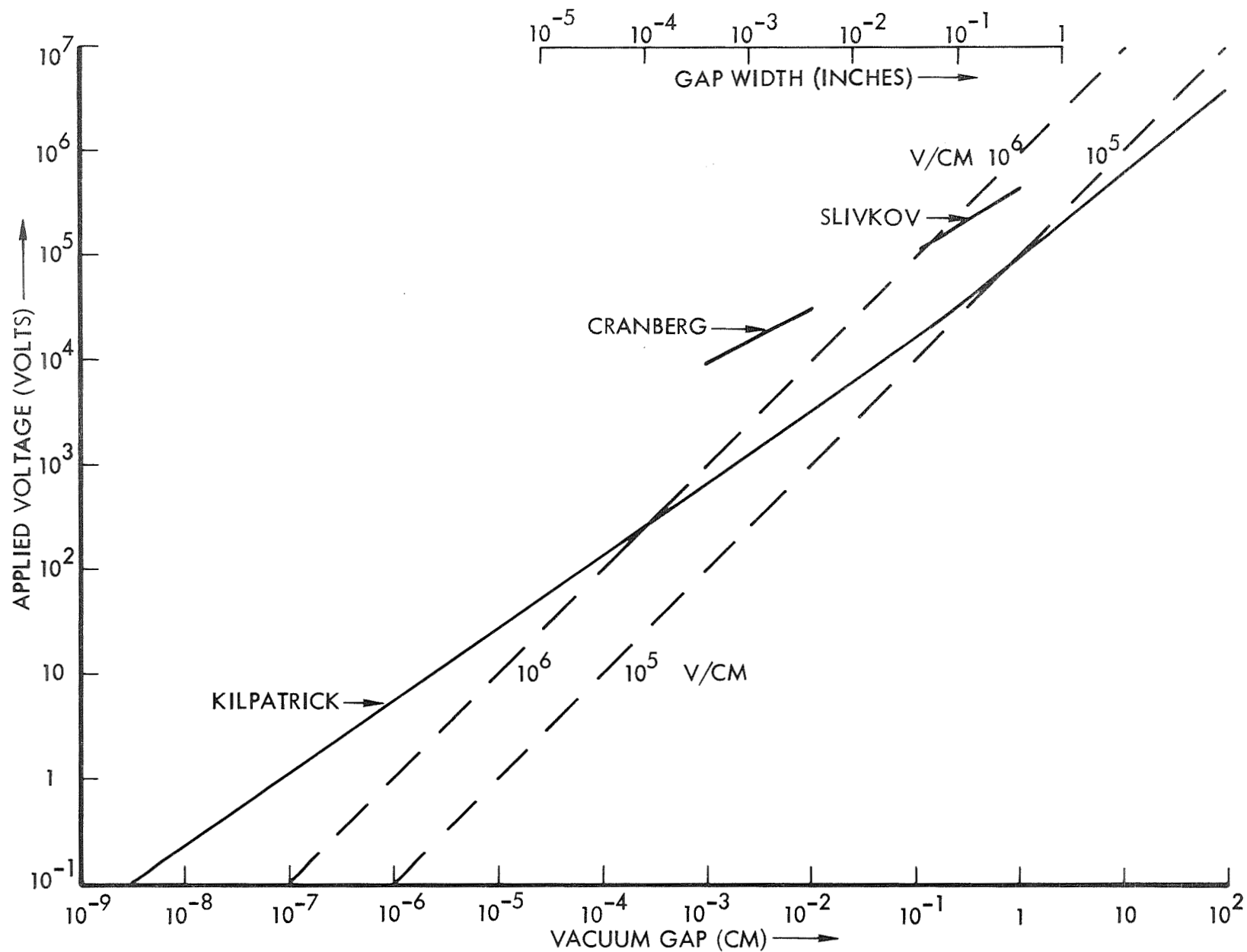


Figure 9: VACUUM GAP BREAKDOWN CRITERIA

DE-121734-1

Nordheim (Reference 22) corrected this expression taking into account the Schottky effect (Reference 23), which was confirmed by Dobrezow (Reference 24), obtaining the Fowler-Nordheim current j_{FN} .

$$j_{FN} = \frac{1.57 \times 10^{-6} E^2}{\phi t^2(x)} \exp\left(\frac{-6.83 \times 10^7 \phi^{3/2} f(x)}{E}\right) \quad (16)$$

where ϕ is in eV, E is in V/cm, and the functions $t(x)$ and $f(x)$ with the argument $x = 3.79 \times 10^{-4} \sqrt{E/\phi}$ are tabulated by Good and Muller (Reference 25). Kaminsky (Reference 26) gives an excellent summary of emission from real surfaces. It is clear that for applied fields greater than 10^6 volts/cm polarization fields become important and they must be considered. In analyzing Nordheim's correction one must be careful to distinguish the external applied field from the field at the emitter.

Non-uniformity of the emitter surface intensifies the field so that E is replaced by mE in the emission current expression. Values of m as high as 30 have been measured for Schottky emission (Reference 27). We are concerned only with electron discharges so the non-uniformity of the cathode is most important. Non-uniformity of the anode influences the character, stability, and duration of the discharge but not its initiation. Cell, grid, and interconnector surfaces will be important when they are negative with respect to the plasma. The effect of non-uniformity of the plasma as a cathode has not been established.

Effect of Mercury

The probability of neutral mercury from the thruster coating the array is analyzed elsewhere in this report. Were such a layer to form, it would provide a metallic sheet between the plasma and array insulation. This layer will be non-uniform because of the vapor pressure and surface tension (Reference 26) of mercury. The mercury patches would provide the largest conductive surface to the plasma and would be within a few volts of plasma potential below 10^4 kilometers altitude and within a few tens of volts of plasma potential at higher altitude in an equilibrium situation. It seems likely that only transient surges in the current, due to the instability of the sheath region in a streaming plasma, could possibly be large enough to start a discharge. We estimate that such currents will be under 1 amp/cm² in a 10^{-4} cm² local spot. This current would be too low to initiate a discharge since a typical requirement is 10^2 amp/cm².

Voids

Specifications for solar cell covers supplied by Optical Coating Laboratory, Inc. allow bubbles as large as 0.003 inch diameter in Corning 0211 Microsheet. Specifications for covers of Corning No. 7940 fused silica allow the following size bubbles.

<u>Cover Thickness, Inches</u>	<u>Maximum Bubble Diameter, Inches</u>
Greater than 0.025	0.015
0.015 to 0.025	0.010
Less than 0.006	0.003 open

Included bubbles of less than 0.005 inch are permitted in all cover thicknesses. Three bubbles of the maximum size specified are permitted for a 1 x 2 cm area.

Small quantities of air are entrapped in solar cell covers and other insulations during production. This air creates small pinholes or voids. Also small voids may appear when insulation surfaces are bonded together or when resins are used to impregnate open evacuated cavities. The gas in voids will be at near one atmosphere in pressure (References 19, 20, 27). Assuming that these voids are embedded or sealed within the insulation is the basis of a first analysis. A second analysis is based on the probability of an open void or pit being created by a micrometeoroid.

Closed Voids

An analysis was based on the following conditions:

1. Void diameter is 0.001 inch (0.0025 cm)
2. Void internal pressure is 760 torr
3. Thickness of insulation is 0.020 inch (0.051 cm)
4. Insulation dielectric constant is 4.0

Then

$$\begin{aligned} Pd &= 2.5 \times 10^{-3} \times 760 \\ &= 1.9 \text{ torr-cm} \end{aligned}$$

where P is pressure and d is spacing. As shown in the Paschen's law curve, (Figure 10), the ionization potential of residual gas within the void is 310 volts ac, or 440 volts dc.

The gas void within the dielectric can be modeled as three capacitors in series as shown in Figure 11.

$$V = V_I \left(1 + \frac{t_1}{t_2 E_1} + \frac{t_3}{t_2 E_3} \right) = 440 \left(1 + \frac{0.009}{0.001 \times 4} + \frac{0.010}{0.001 \times 4} \right) = 2530 \text{ volts}$$

where V is the applied voltage, V_I is the ionization potential, t and E are the thickness and dielectric constant of insulation as defined in Figure 11.

This analysis shows that the gas within the void will ionize when a voltage of 2530 vdc is impressed across this 20-mils-thick insulation. This is only 125 volts/mil operating voltage. The ionized gas will tend to enlarge the void. If the void breaks open, it will become evacuated and be an open void.

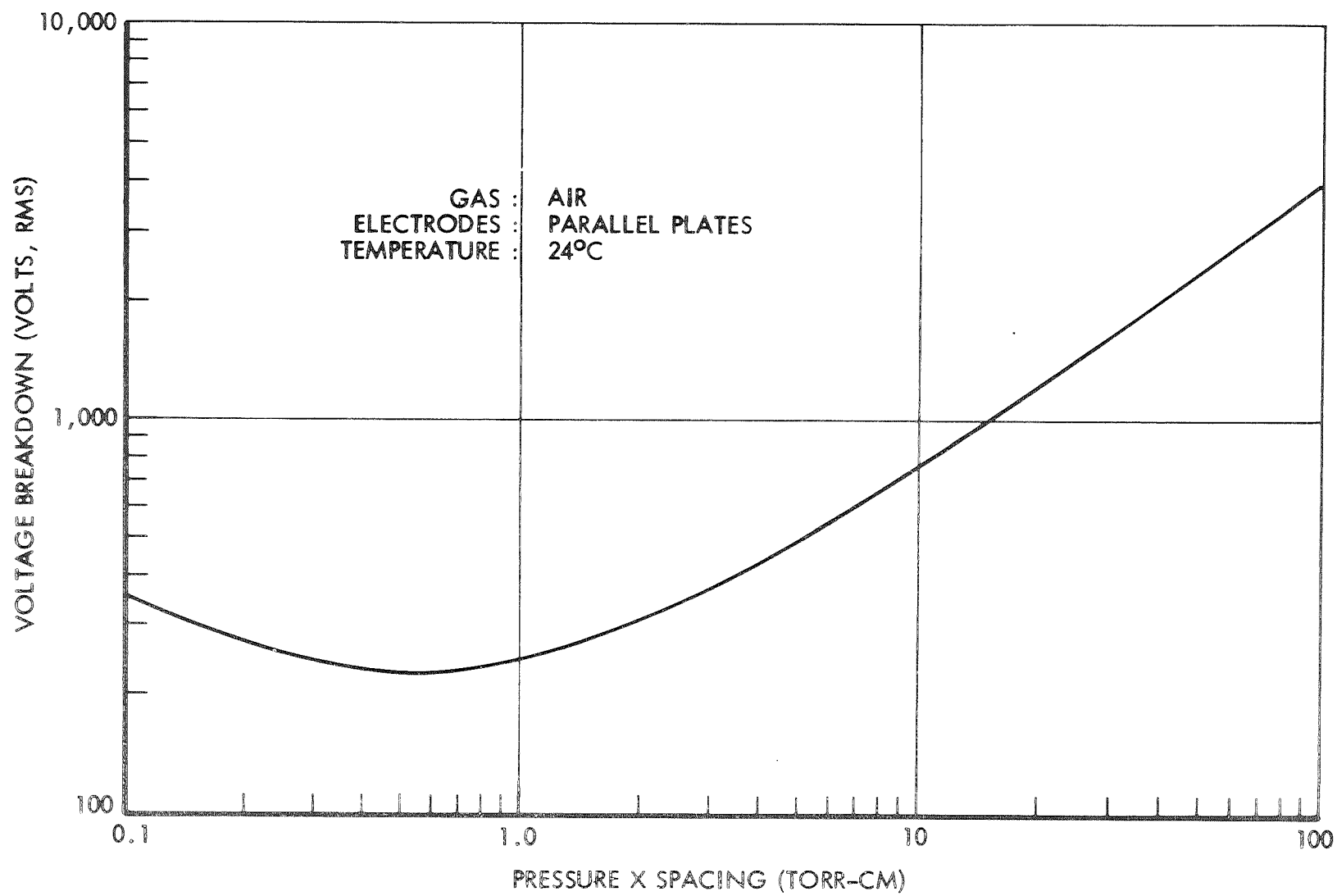
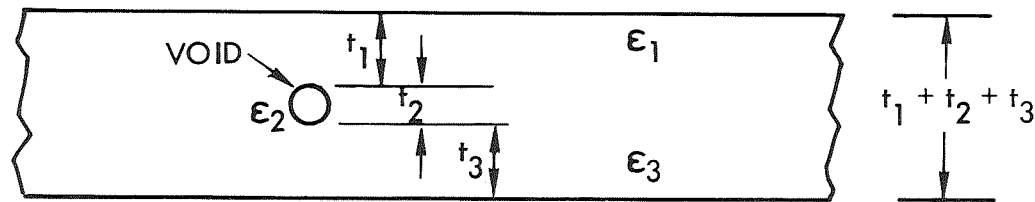


Figure 10: PASCHEN'S LAW CURVE



SCHEMATIC OF VOID IN INSULATION

$\epsilon_1 = \epsilon_3 =$ DIELECTRIC CONSTANT OF SOLID INSULATION = 4.0

$\epsilon_2 =$ DIELECTRIC CONSTANT OF GAS IN VOID = 1.0

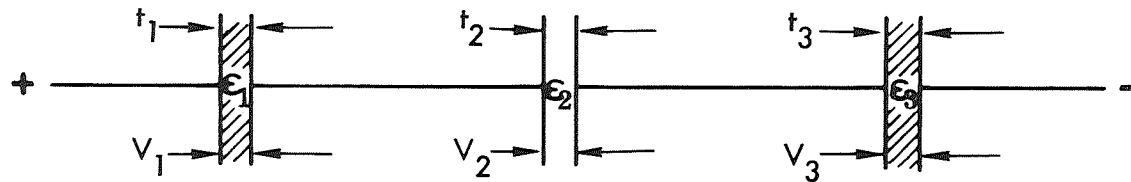
$t_1 + t_2 + t_3 =$ THICKNESS OF SOLID INSULATION = 0.020 INCH (0.051 cm)

$t_2 =$ THICKNESS OF VOID = 0.001 INCH (0.0025 cm)

$V =$ TOTAL IMPRESSED VOLTAGE

$V_1 =$ IONIZATION VOLTAGE WITHIN VOID = 440 VDC

$V_2 =$ VOLTAGE ACROSS VOID



EQUIVALENT CAPACITORS

Figure 11: MODEL OF VOID IN SOLID INSULATION

A gas-filled void next to an electrode can be analyzed in the same way as an embedded void. The simplified equation for ionizing potential is

$$V = V_I \left(1 + \frac{t_1}{t_2 C_1} \right) = 440 \left(1 + \frac{0.019}{0.001 \times 4} \right) = 2530 \text{ volts}$$

Initial pressure and spacing are assumed to be the same for the embedded void.

Open void.

If the spacing-pressure dimensions ($P \times d$) for the void or crack is less than 10^{-3} torr-centimeters, the probability of discharges within the void are negligible. This is because the mean free path is so great that gas ionization cannot occur unless several thousand volts are applied directly to the void. A closed void with air at 760 torr pressure would have to be smaller than 0.0005 mil (0.0013 cm) in diameter to have a Pd product of less than 10^{-3} . An open void would normally outgas in vacuum within 3 hours to a Pd of 10^{-3} .

The remaining insulation outside of the void will have an increased voltage gradient as a consequence of the void.

5.2 Future Analysis and Experimentation

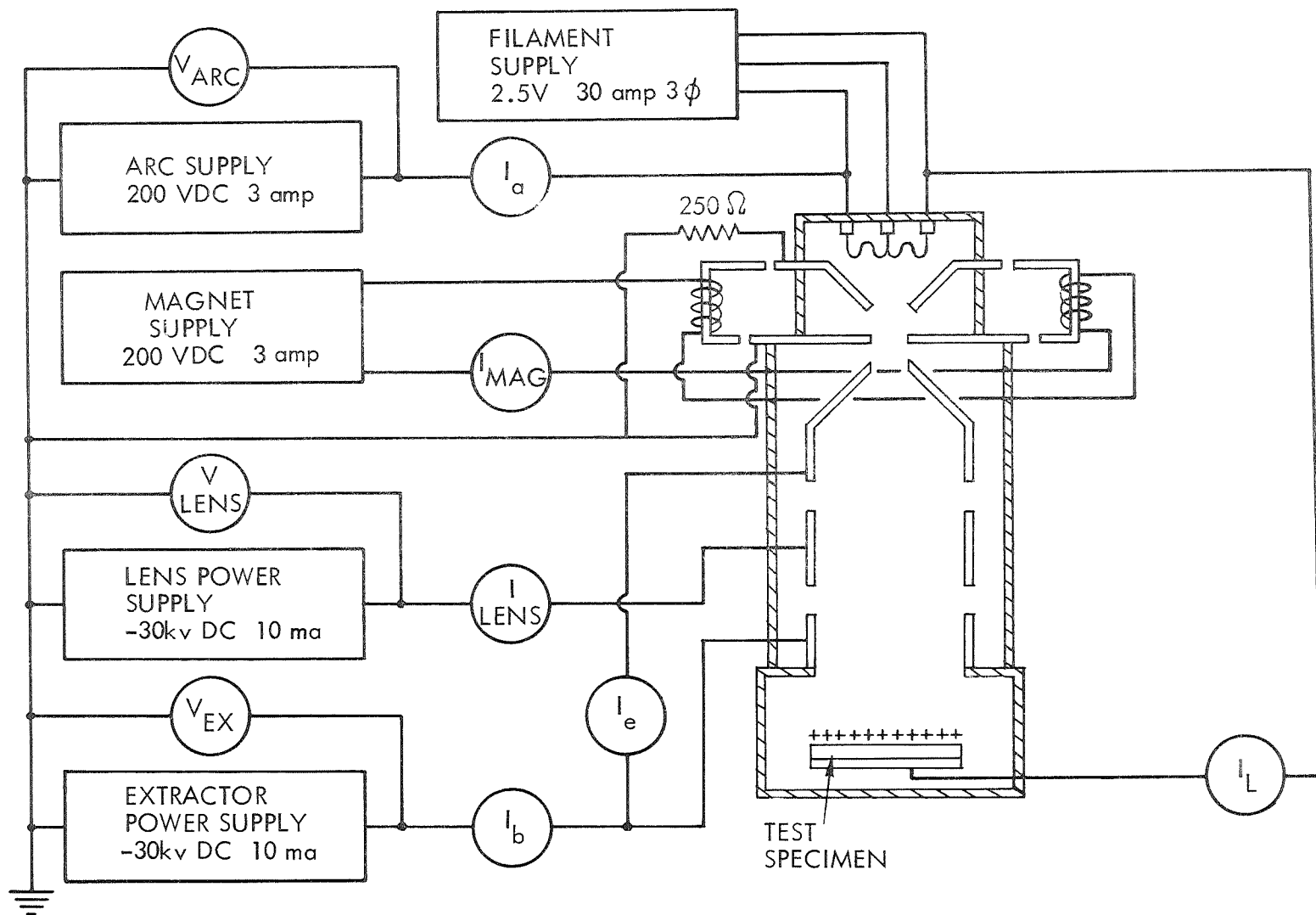
The determination of the capability of fused silica solar cell covers and other dielectric materials, requires measurement of the breakdown characteristics with current-limited power sources. The relationships between breakdown strength with metallic electrodes and those with the ionospheric plasma acting at an electrode are not yet known with assurance.

Two types of testing are required. The first will establish fundamentals using the duoplasmatron. The second will establish pertinent characteristics of a variety of insulations in a current-limited breakdown environment. Charge build-up on insulating surfaces of the array can be investigated with a duoplasmatron, which can deposit ions on polymer insulations and on solar cell covers. Polymers and cell covers with selected types of defects, such as voids and pinholes, can be placed within the ion beam and the leakage currents can be measured. Surface resistivity can also be measured with auxiliary electrodes.

Principle of Operation of the Duoplasmatron

The duoplasmatron has a chamber in which a constrained plasma is generated by electrons emitted into a gas within a magnetic field, and ions extracted from the plasma are focused by electric fields on the test specimen (Figure 12).

The electrons emitted from an oxide-coated cathode into the gas fill the arc region, maintaining an arc discharge between cathode and anode. This discharge is focused on the center of the anode by the intermediate electrode through the formation of a bubble-shaped equipotential (anode bright layer). The plasma formed by the discharge is additionally constrained by making the intermediate electrode and anode the poles of an electromagnet.



D2-121734-1

Figure 12: DUOPLASMATRON CHAMBER AND POWER SUPPLIES

This combined focusing action provides an extremely dense plasma with a high current density at the center of the anode. To prevent erosion, the anode has a small tungsten insert with a very small aperture. The plasma exudes through this aperture and is thus available for extraction to form an ion beam.

The extractor is held at a high negative potential to attract positive ions from this plasma. The extractor is shaped to produce a beam of ions which then passes through the einzel lens formed by the gaps between the lens electrode and its neighbors. The focal length of this lens is varied by adjusting the potential of the lens electrode relative to that of the extractor.

The bottom plate is held at the extractor potential to re-accelerate the beam into the target chamber.

Auxiliary Equipment

The duoplasmatron requires a vacuum pump and a gas feed system. The major gas load on the vacuum pump is the neutralized beam. Since 1.0 ma of beam produces about 0.2 micron-liters per second of gas flow, a pumping speed of 200 liters per second is required to maintain a vacuum of 10^{-6} torr in the absence of any other gas load.

Current-Limited Breakdown Apparatus

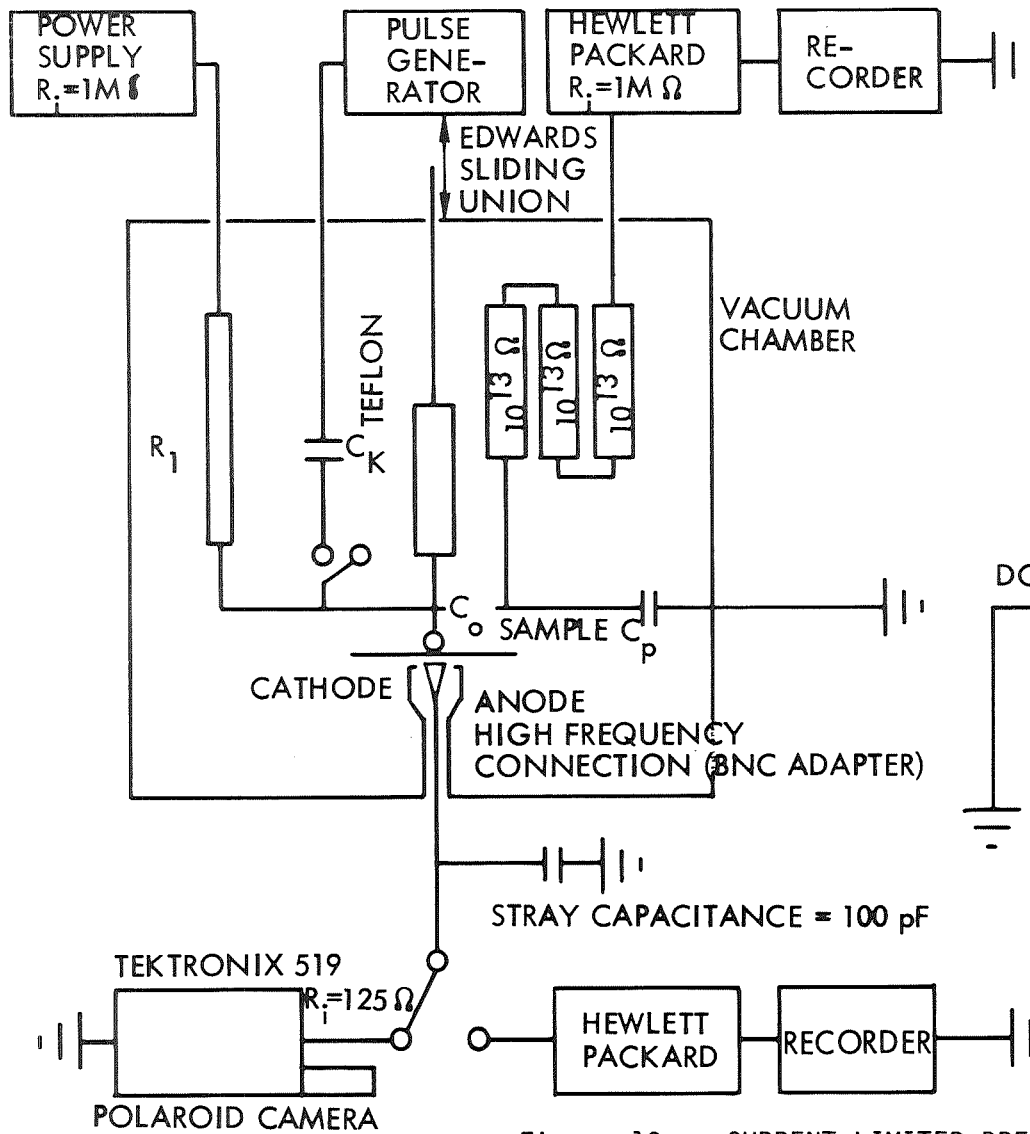
Many samples of cell covers and other insulating materials will have to be tested for dielectric strength. It is not likely that instrumentation like the duoplasmatron will be practical for any except basic studies. Simulation which provides a means of measuring dielectric breakdown under current limited conditions is necessary. For this, the work described in Reference 21 is applicable, and is summarized below.

Non-destructive breakdown (NDB) in Mylar films was observed in the laboratory using apparatus which limited the current available to the sample. NDB was observed at 6900 volts/mil (2.7×10^6 volts/cm), which is higher than the voltage gradients anticipated for the solar cell insulation. It is interesting that for current limited conditions NDB occurred only with metallic cathodes. Breakdown with non-metallic cathodes did not occur at voltages exceeding 15,000 volts/mil (6×10^6 volts/cm). The conclusion was that electron injection from a metallic cathode was necessary.

These tests were made in a vacuum chamber at 10^{-5} torr. The circuitry is shown in Figures 13a and 13b. Data were obtained both with and without illumination of the sample by the 3660 Angstrom line of a mercury lamp. Illumination reduced the NDB of a 0.16 mil thick sample from 7500 volts/mil to 7200 volts/mil. This information aids in the theoretical explanation of NDB, and indicates that the decrease in dielectric strength with illumination is not significant in the application of Mylar as an insulation.

Although limited, the current density still was 10^3 amps/cm² for a channel of approximately 4×10^{-4} cm² in these tests. Current density available

a. TEST APPARATUS



b. ELECTRICAL CIRCUIT

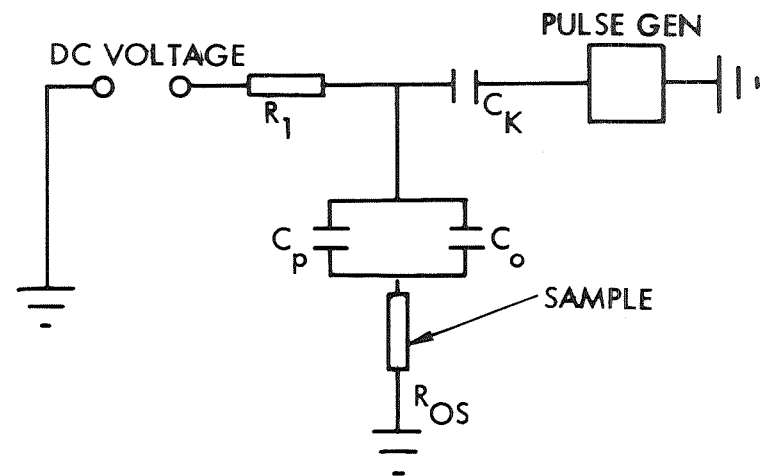


Figure 13: CURRENT LIMITED BREAKDOWN STUDY

from the plasma is less by a factor of 10^6 . It thus appears that the breakdown voltage for materials such as Mylar and Kapton can be very high when the ionospheric plasma is the cathode.

Shown in Figure 14 is another conceptual design of a fixture for testing insulating materials. The basic requirement of limiting the current to simulate a plasma source is achieved by using a high resistivity liquid as one electrode. Liquids with resistivities in the range 10^{11} to 10^{12} ohm-cm are dielectric grade castor oil, glyceryl tri-acetoxy-stearate and silicate-ester fluid. Using electrodes of these materials will limit current to about 10^{-6} amp/cm². Electrode liquids for higher or lower current densities are available.

Test Program for Insulating Materials

A test program is envisioned which will provide the data necessary for design of the insulation system used to operate in the hostile space plasma environment. However, to put the insulation requirements into perspective, examine the construction of the silicon solar cell. Shown in Figure 15 are the electrode system for a solderless solar cell and a metallized dielectric capacitor. The electrode systems are similar. These capacitors expose several square feet of insulation in each unit to possible breakdown. Since it is not practicable to use fault-free dielectrics an electrode system was developed which enables the capacitor to be self healing. When a fault occurs the high current density in the electrode at the fault vaporizes the metal and clears the fault. There are over a billion of these self healing capacitors in use in the telephone system. As shown in Figure 15, a nail can be driven into the capacitor with no ill effect. It is postulated that the silicon solar cell with silver-titanium contacts may now be self-clearing or can be made so with minor changes in the silver-titanium electrode. A micrometeoroid puncture would then cause only a momentary short circuit. A test program for determining dielectric strength and resistivity of dielectric materials under simulated operating conditions is summarized below.

<u>Typical Materials to be Tested</u>	<u>Specimen Description</u>
Polyimides (Kapton)	0.25, 1.0, 5.0 mils thick sheet
Poly-p-xylylene (Parylene)	0.1, 1.0, 5.0 mils thick deposited on electrodes
Silicone	0.5, 1.0, 5.0 mils thick deposited on electrodes
Fused Silica	Cover slips, 3.0, 6.0, 10.0 mils thick, with selected voids
Microsheet, 0211 Corning Glass	Cover Slips, 3.0, 6.0, 10.0 mils thick
Epoxy	0.25, 2.0, 5.0 mils thick sheet
Fluoro-ethylene-propylene (Teflon-FEP)	0.5, 1.0, 5.0 mils thick deposited on electrodes

The major items of apparatus required for this testing are:

- Duoplasmatron and auxiliary equipment (Figure 12)
- Current limiting dielectric breakdown test apparatus (Figure 13)
- Vacuum chamber, 1 cubic foot volume, capable of 10^{-6} torr vacuum.

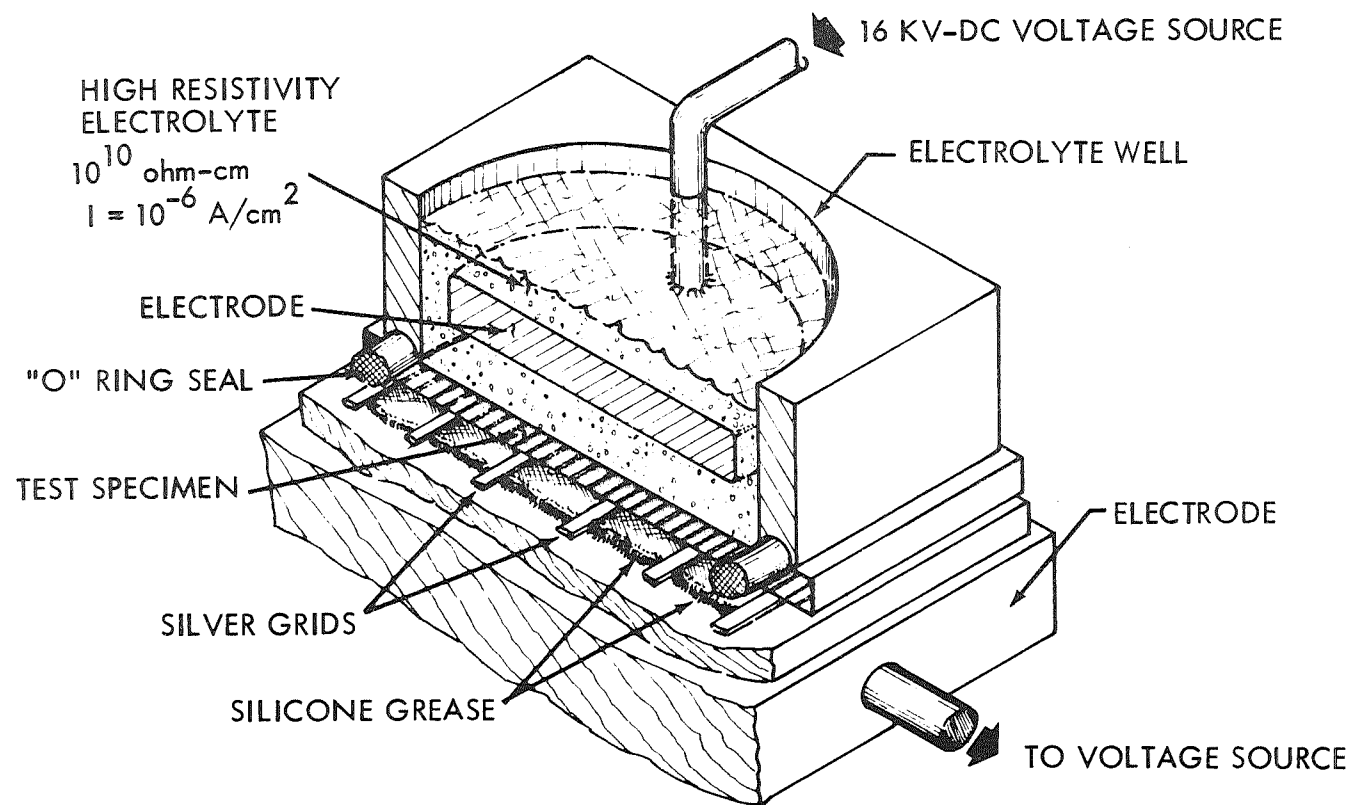
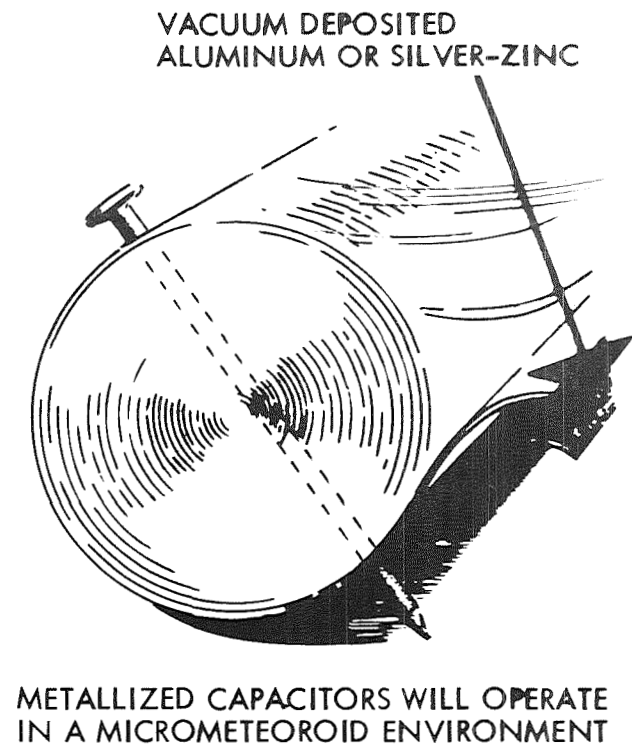
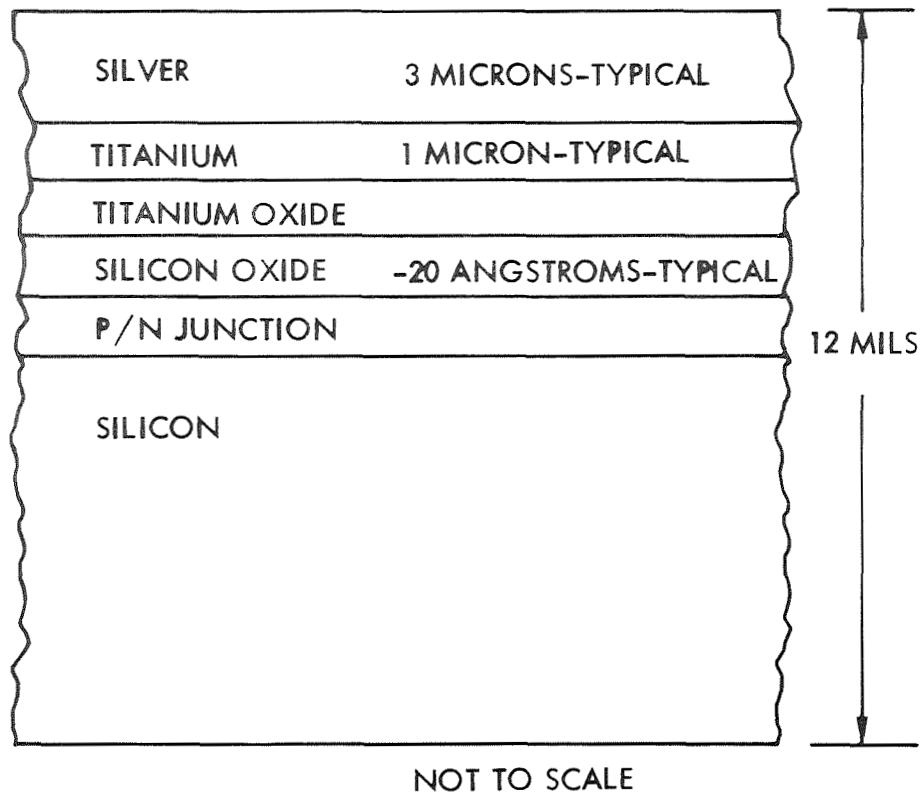


Figure 14: TEST JIG FOR INVESTIGATION OF CURRENT LIMITED BREAKDOWN



DR-121734-1

Figure 15: CROSS SECTION OF A TYPICAL SILICON SOLAR CELL SILVER-TITANIUM CONTACT

6.0

FABRICATION AND CONCEPTUAL DESIGNS

The previously described analysis of plasma leakage currents indicated that (1) the lowest power losses during flight through the ionosphere will be attained if the high-voltage solar array is completely insulated, (2) holes punctured in the insulation by micrometeoroids may not be self-enlarging, and (3) the power loss through such holes may not be significant. The last two conclusions require verification with further testing and analysis. However, the advantages of a totally insulated array appeared to be so significant that the conceptual-design effort was directed toward methods of making a practical insulated array.

An important new dielectric, Union Carbide's Parylene C, appears at this time to be the most promising insulator, and several conceptual designs are based on its use. However, Parylene C still needs much laboratory evaluation. Therefore, alternate conceptual high voltage solar array designs based on more conventional insulations are also provided.

The problems in fabrication which require development effort are related to insulation, safety, and electrical testing.

A fabrication flow diagram is shown in Figure 16 for a high voltage array. Shaded blocks indicate where fabrication of the high voltage array differs sufficiently from the low voltage array fabrication to warrant additional study and development.

6.1

Array Insulation

Insulating the array will be the most critical of the fabrication processes. Parylene appears at this time to be the most promising void-free material for insulating the array. Two Parylene materials available from Union Carbide are Parylene N and Parylene C. (Figure 17). Parylene N, the basic material, has dielectric qualities that are among the best. However, its mechanical characteristics are not so desirable, being brittle. Parylene C, with a chlorine atom substituted for one hydrogen on the benzene ring, has excellent dielectric qualities and also suitable mechanical properties for operation in space. Laboratory evaluation of Parylene is required to determine its stability in ultraviolet and its voltage breakdown and mechanical characteristics when applied to a high voltage solar array.

The Parylene C properties provided by Union Carbide are summarized in Table 4. It must be emphasized that the numbers shown are not directly applicable to design. For example, the 5,600 volts/mil for dielectric strength indicates a good insulation. However, the dielectric strength is measured during application of a ramp voltage changing at several hundred volts per minute. Also, the electrodes used in testing are very different from those on an array. The volume and surface resistivities quoted cannot be reliably used for design or analysis. These resistivities are normally measured in the laboratory with a low voltage and a short electrification time, usually 100 volts for one minute. Resistivities vary greatly with both voltage and time of electrification. With 16,000 volts applied the resistivity can be expected to be much lower than the values measured with low voltage. On the other hand, the time of electrification for the high voltage solar array is very long, causing the effective resistivity to be higher than that in the laboratory.

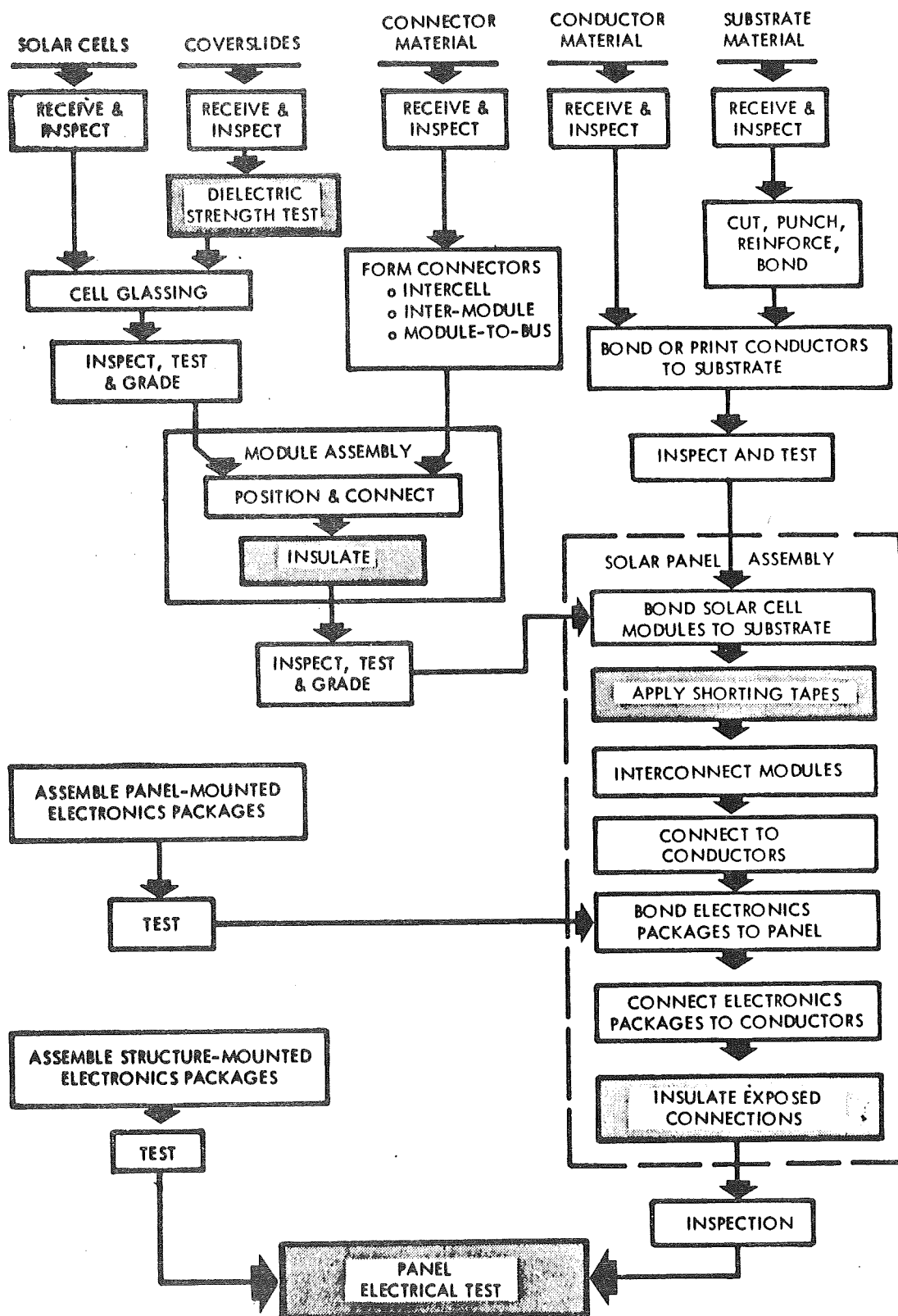
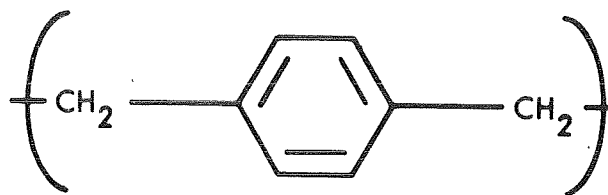
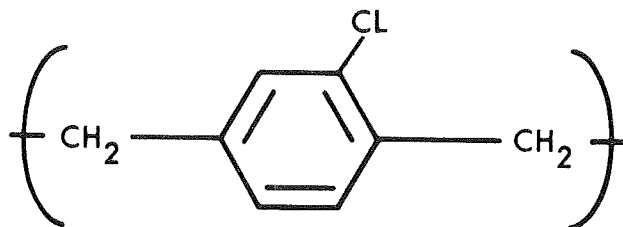


Figure 16: FABRICATION FLOW DIAGRAM



PARYLENE N



PARYLENE C

Figure 17: PARYLENE CHEMICAL STRUCTURE

<u>Characteristic</u>	<u>Value</u>	<u>Remarks</u>
Dielectric Strength (short time)	5,600 V/Mil	0.001 inch thick specimen
Volume Resistivity 23°C, 50% RH	8.8×10^{16} ohm/cm	
Surface Resistivity	10^{14} ohms/sq.	
Dielectric Constant	3.10	1,000 Hertz
Dissipation Factor	0.019	1,000 Hertz
Elongation to Break	200%	
Yield Strength	8,000 PSI	
Linear Coefficient of Expansion	$3.5 \times 10^{-5}/^{\circ}\text{C}$	

Table 4: SUMMARY OF PROPERTIES OF PARYLENE-C

The dielectric constant of Parylene is 3.1, a reasonably high value. A high dielectric constant is desirable because the insulation will be in series with the vacuum of space and the voltage gradients are inversely proportional to the dielectric constant and conductance. The dissipation factor of Parylene C is high compared to Parylene N and other low loss dielectrics. However, for the direct voltages of the solar array the dissipation factor is not critical. The mechanical characteristics appear adequate. "Elongation to break" is important because of the requirements of a roll-up array and the large temperature variations in an eclipsing orbit. The coefficient of expansion of Parylene is low in comparison with other organic coating materials, but is still high in comparison with fused silica with which it will be in contact.

The effect of thickness on voltage breakdown of Parylene is shown in Figure 18. Direct voltage was used by Union Carbide in obtaining the data, however the voltage was applied rapidly and breakdown occurred in seconds or minutes. Electrodes were metallic and current was not limited. Thus the test, although useful, cannot be correlated with the high voltage solar array operating configuration or environment. The Union Carbide data do suggest that 3 to 5 mils may be adequate insulation for the high voltage array.

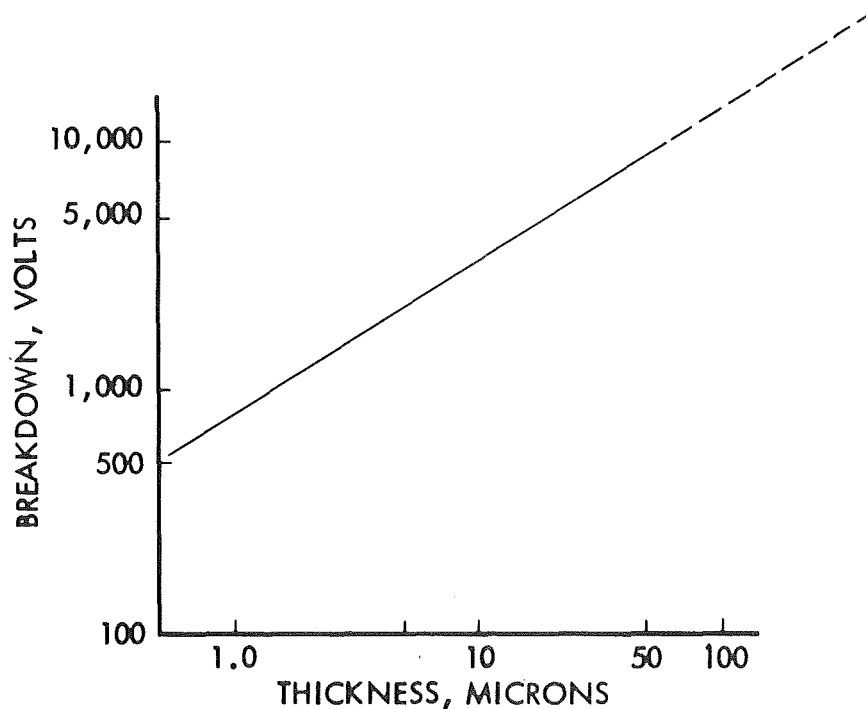


Figure 18: BREAKDOWN VOLTAGE OF PARYLENE C
VS POLYMER FILM THICKNESS

The Parylene deposition process developed by Union Carbide is shown in Figure 19. This process may provide a true pinhole-free conformal insulation. The Parylene polymer is deposited from vapor at about 0.1 torr pressure, at which the mean free path of the gas molecules in the deposition chamber is about 0.1 cm. Therefore, unlike vacuum metalizing, the deposition is not line-of-sight, and all sides of an object are encapsulated uniformly by the gaseous monomer. This produces a truly conformal coating that can flow around the cell connectors and coat the underside of the connectors, as well as the top side. It will also coat all exposed parts of the solar cells and solar array.

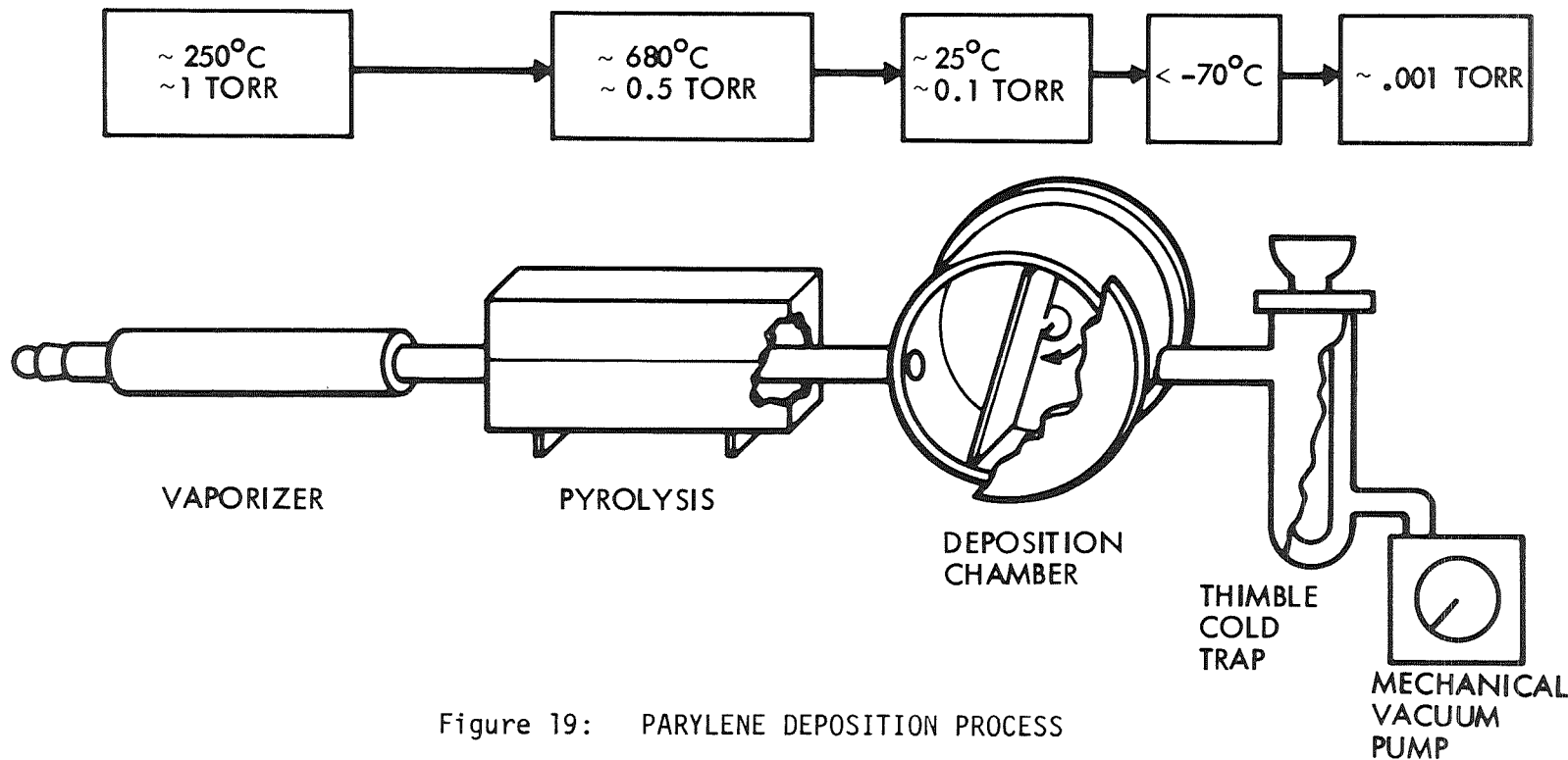
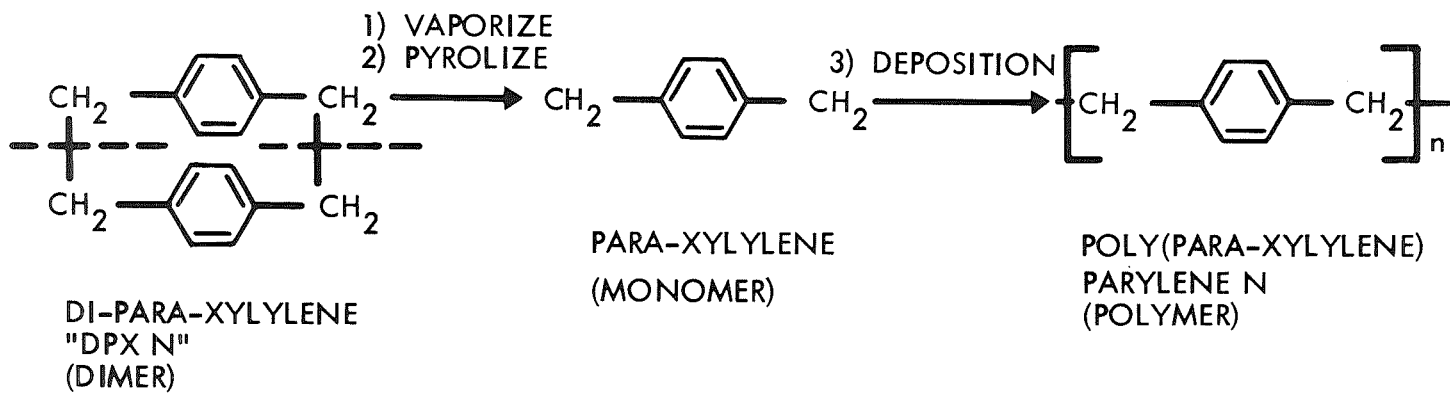


Figure 19: PARYLENE DEPOSITION PROCESS

Three approaches are postulated for the use of Parylene C. The first approach, and the most conventional, is to vacuum deposit the Parylene on completed modules of the solar array. Masks would be used to prevent deposition of polymer on the quartz cell covers. The Parylene covers all exposed areas with insulation. After deposition, the masks are removed leaving a panel that is 100 percent insulated.

The second approach is to build the array but leave off the cell covers. The entire panel is then coated with Parylene, and the covers are bonded on the Parylene. This approach eliminates masking and gives a continuous insulation over the entire panel.

The third approach is to use Parylene as an insulation and as a thermal control coating in place of cell covers. Extensive testing will be required to establish the durability of Parylene in space, but substantial savings are possible. For example, the cost of cell covers, cover-glass adhesives, and conventional installation of the solar cells can be over \$1,000,000 for a 320,000-cell array.

A conceptual design of a Parylene-insulated solar cell assembly is shown in Figure 20. The design is a space proven one, but having the addition of the conformal coating of dielectric. The submodule interconnector is expanded silver, coated with Parylene on all surfaces including the inner edges of the mesh openings.

Conventional Insulation

Another conceptual design uses silicone insulation in the critical area between cells (Figure 21). Both conventional cells and cells with wrap-around contacts are shown. Wrap-around contacts have possible advantages because interconnections can be printed or bonded to the substrate. Also the void problem may be simplified. Wrap-around contacts have not been produced in large quantities, are not flight-proven, and are not necessary for success. However, they are available and should be considered in a development program. As emphasized in the discussion of voltage stress, voids larger than a critical size are not acceptable. Void size, a function of both materials and configuration, needs to be controlled.

A conceptual design in which the array is assembled from insulated modules is shown in Figure 22. In this design the parallel groups of solar cells with protective fused silica covers are impregnated in thin-walled preforms. After inspection and test these modules are connected in the desired series and parallel configuration. This concept has been used successfully in other electronic assemblies.

6.2 Testing

Cell cover and substrate materials will have to be tested for dielectric strength. It will be necessary to use test methods which can be applied economically to large areas of substrate and large numbers of coverslides. Such tests can be American Society for Testing Materials (ASTM) tests, modified by the results of research and development tests made under simulated mission environment conditions.

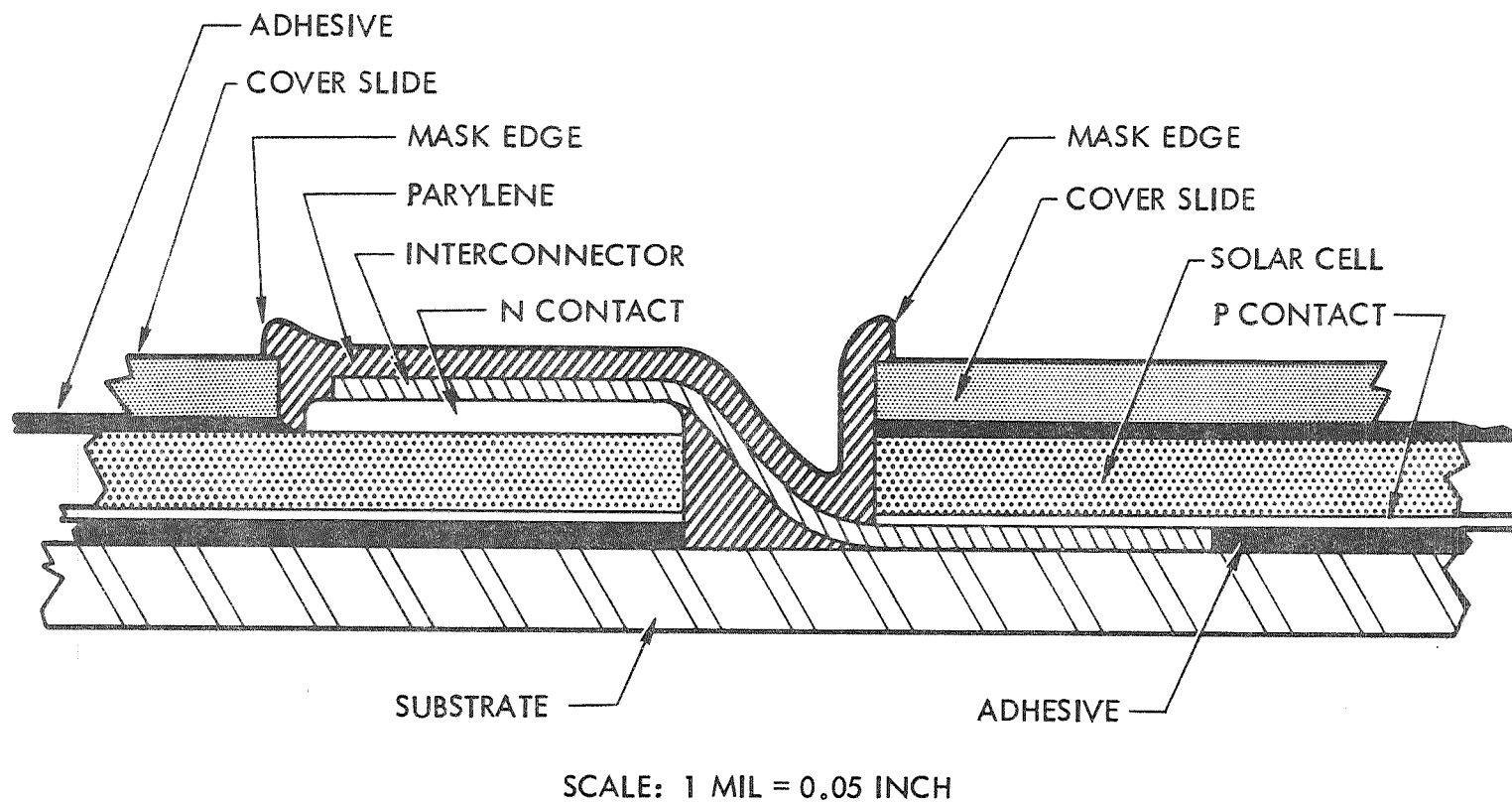
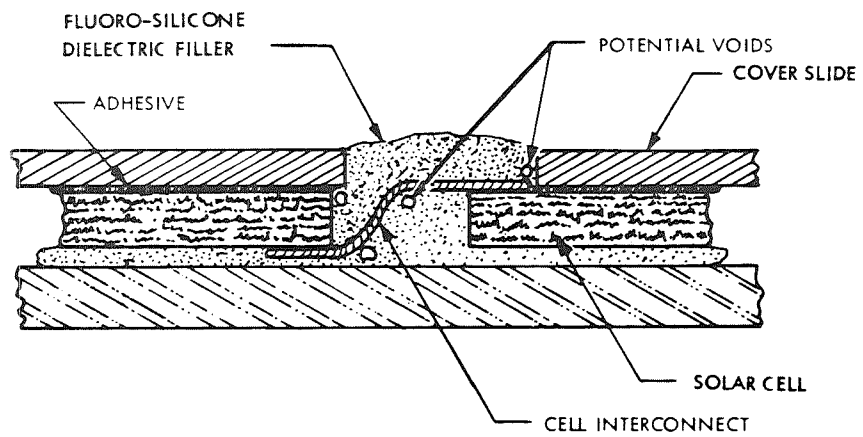


Figure 20: PARYLENE INSULATED SOLAR CELL ASSEMBLY

WITH CONVENTIONAL CONTACTS



WITH WRAP-AROUND CONTACTS

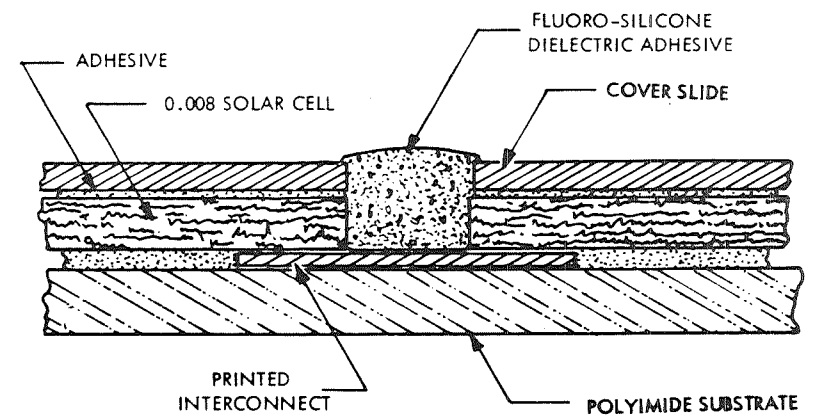
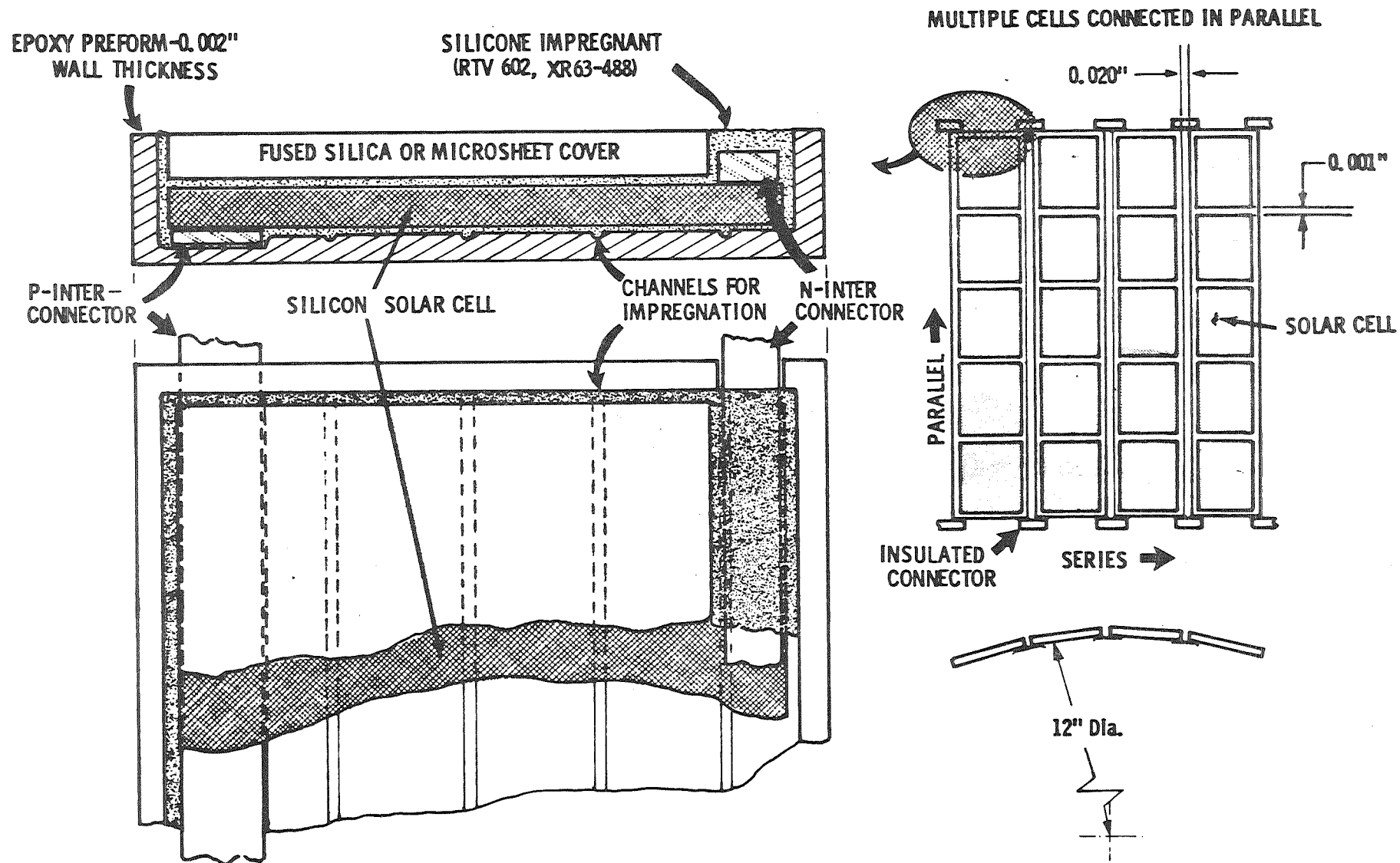


Figure 21: HIGH VOLTAGE SOLAR CELL INTERCONNECTIONS



102-121734-1

Figure 22: SOLAR CELL MODULE ENCAPSULATED IN THIN-WALLED PRE-FORM

Elements of the array can be tested functionally in a simulated ionospheric plasma. However, testing large-area panels in a simulated ionospheric plasma would be costly. Thus, an alternate means of simulating the plasma during tests for checking the fabrication process would be desirable. The plasma characteristic of interest here is its conductivity. A conceptual design of a plasma simulator (Figure 23) uses an electrolytic tank for testing large solar-cell panels. The conducting liquid can provide nearly the same voltage gradients in the dielectrics of the panel as the ionospheric plasma. Parameters to be measured are insulation resistance, voltage breakdown strength, electrical noise, and the effects of varying the conductivity of the operating medium.

6.3 Safety

The possibility of accidents from the high voltage can be minimized with safety interlocks and shorting devices. However, shorting of over 500 series-connected cells can be misleading, because variations within cells make the voltage drop in a long string of shorted solar cells non-uniform. Two approaches to this problem are: (1) Expose multiple terminals for shorting, and (2) short-circuit long strings of cells using conductive pressure sensitive tape such as Scotch X-1170.

Working safely with high voltages requires strict enforcement of documented procedures. Examples are The Boeing Company's Industrial Hazards Control Bulletins S-15, "High Electrical Potential Testing," and S-16, "Personnel Electrical Hazards."

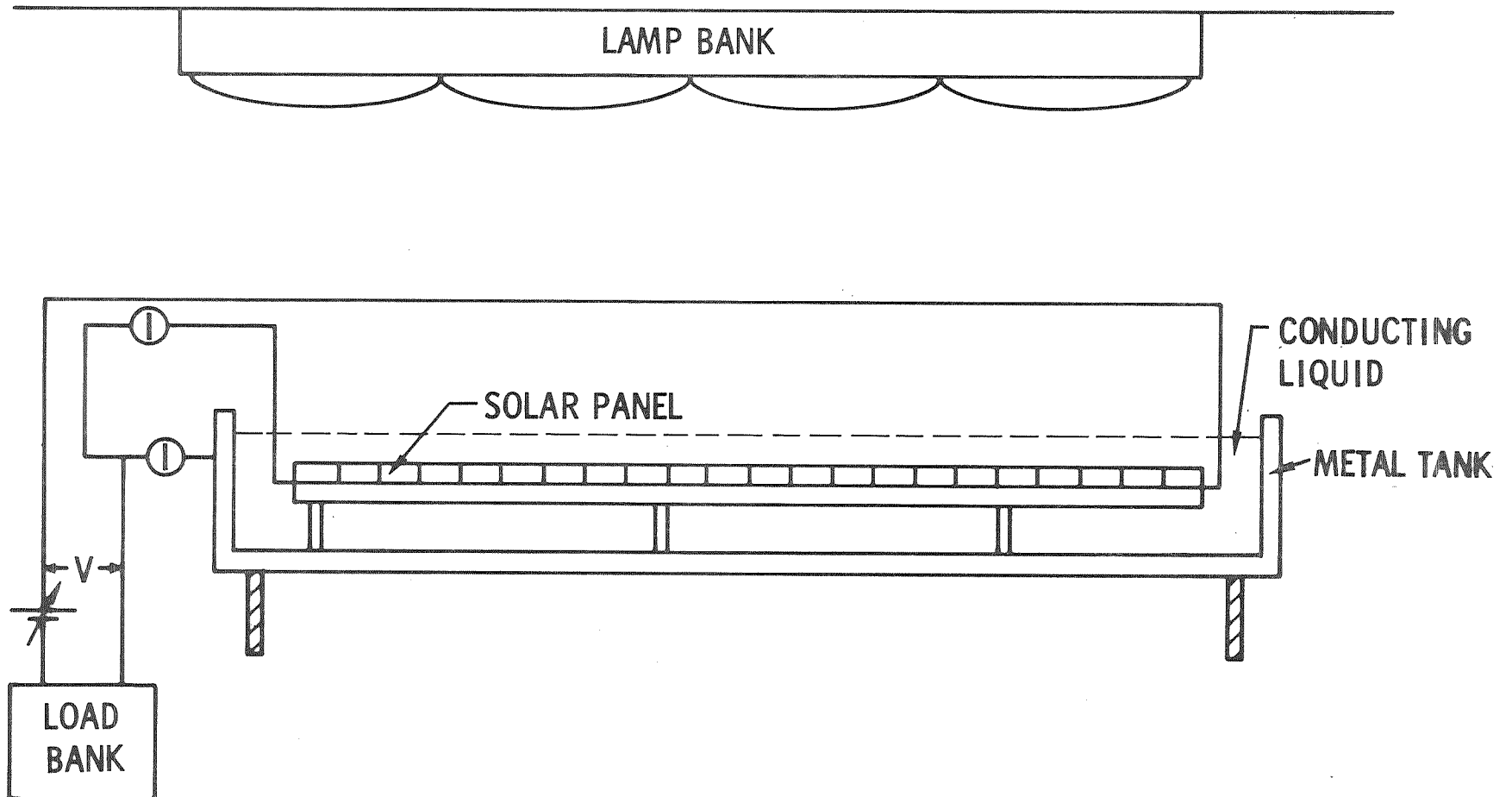


Figure 23: ELECTROLYTIC TANK TESTING OF LARGE HIGH VOLTAGE SOLAR PANEL

7.0

RELIABILITY ANALYSES

The high voltage solar array is assumed to consist of a string of 32,000 submodules each having 10 parallel cells and 2 shunting diodes. This design meets the requirements of 16,000 volts at 15,000 watts, assuming that each cell delivers 0.5 volts at 0.093 amp. To provide different voltage levels, the string of submodules is divided into voltage blocks.

Reliability analyses were conducted to estimate the failure risk associated with the design elements unique to the high voltage array application. Potential problems were identified and methods for achieving reasonable reliability levels were developed.

7.1

Summary

The major design elements of the high voltage solar array are:

- Solar cell submodule with shunting diode
- Submodule interconnector
- Busses
- Block-to-bus connectors
- Insulation

Other elements of the solar array such as structure, solar cell-substrate, cell-cover adhesive, and solar cell adhesives employ conventional materials and processes and have not been considered in this reliability analysis. The failure risks associated with these elements are negligible due to application of proven manufacturing and quality control techniques and procedures.

Table 5 presents the failure risks which were derived for the major design elements of the high voltage array.

The unique characteristics affecting reliability of the high voltage solar array design are:

- (1) The many solar cell submodules which must be connected in series to deliver the required voltages.
- (2) The insulation between positive and negative busses will be electrically stressed.
- (3) Insulation on the interconnector will reduce its flexibility.
- (4) New processes are required for application of insulation on exposed high voltage parts of the solar array, such as interconnectors, edges of the solar cells, and electrical terminals.

7.2

Analyses of Design Elements

Failure risks for the individual elements were calculated using failure rate data and mission time or cycles. The mission time used in the analyses was 5 years at synchronous altitude plus 3 months at low altitude. The total mission time was 46,000 hours. Thermal cycling effects were based on an average

Design Element	Function	Failure Mode	Failure Risk	Remarks
Solar cell sub-module with shunting diode	convert sunlight to electrical energy	Submodule Open circuit	1.0×10^{-32}	All cells in submodule and shunting diode fail open
		Open or short circuit failures causing power loss	4.5×10^{-5} (2.4×10^{-7})	Open and shorted cells, shorted diodes; 1.6% margin (1.8% margin). See note 2
Submodule-to-submodule inter-connector	Provide electrical continuity between submodules	Open failure	2.6×10^{-6}	3 parallel connectors between submodules
Electrical busses	Electrical conductor	Structural failure: short between busses	1.0×10^{-6}	Provide adequate spacing and insulation between busses - estimate
Insulation	Protect electrical conductors from environment; prevent shorts	Breakdown; voids	1.0×10^{-5}	Estimate
Block-to-bus connectors	Connect voltage blocks to busses	Open failure	3.7×10^{-5}	Redundant connectors

Note 1: Failure risk is defined as probability of not meeting 16 kV, 15 kW requirements
 2: Percent design margin is percent additional submodules

Table 5: RELIABILITY ANALYSIS SUMMARY-HIGH VOLTAGE SOLAR ARRAY

DE-121734-1

of 16 thermal cycles per day in low altitude orbits and 90 cycles per year at synchronous altitude, for a total of 1890 thermal cycles.

Effects of Cell Failures

Three basic modes of cell failure were identified:

- 1) open circuit failure
- 2) short circuit failure
- 3) degraded cell output.

We assumed that open and short circuit failures would occur at random and that the exponential time-to-failure model $R = e^{-\lambda t}$ was reasonably valid for predicting cell reliability. In this Model, R = reliability; λ = failure rate/hour; t = operating time in hours.

It was also assumed that the degraded cell output was a result of radiation or micrometeoroid damage. Radiation degradation was accounted for by using degraded solar cell operating characteristics in calculating the number of cells required to provide the required power. Degradation from micrometeoroid impact was accounted for by a cell failure rate attributable to this phenomenon. It was further assumed that micrometeoroid cell damage would be either an open or short circuit failure of the cell.

Open Circuit Failures

The effect of an open circuit failure of a solar cell is loss of cell power, reducing the power generating capability of the submodule. This changes the submodule V-I curve. The proposed design has two shunting diodes connected across each submodule to provide an alternate current path in the event that one or more cells fail open in that submodule. Loss of block power will occur only if all cells in a submodule fail open and the shunting diodes also fail open.

Short Circuit Failures

A short circuit failure of a solar cell results in shorting of the entire submodule with subsequent loss of submodule power. This mode may be compensated in design by providing extra solar cell submodules (Δn) so that the probability of more than Δn short circuit failures is less than or equal to the desired failure risk.

Solar Cell Failure Rate

The solar cell failure rate used in the reliability analyses accounts for failure of cells from thermal cycling, fracturing, manufacturing defects, and impact by meteoroids. Several sources were used in developing this failure rate. Figure 24 shows these cell failure rate predictions from these sources as a function of calendar time. Significant variations can be noted in the predicted solar cell failure rates.

It appears that a failure rate of 1.2×10^{-8} failures per hour is a reasonably conservative assumption, allowing for the effects of thermal cycling. This rate was then increased by 50 percent to account for cell failures from

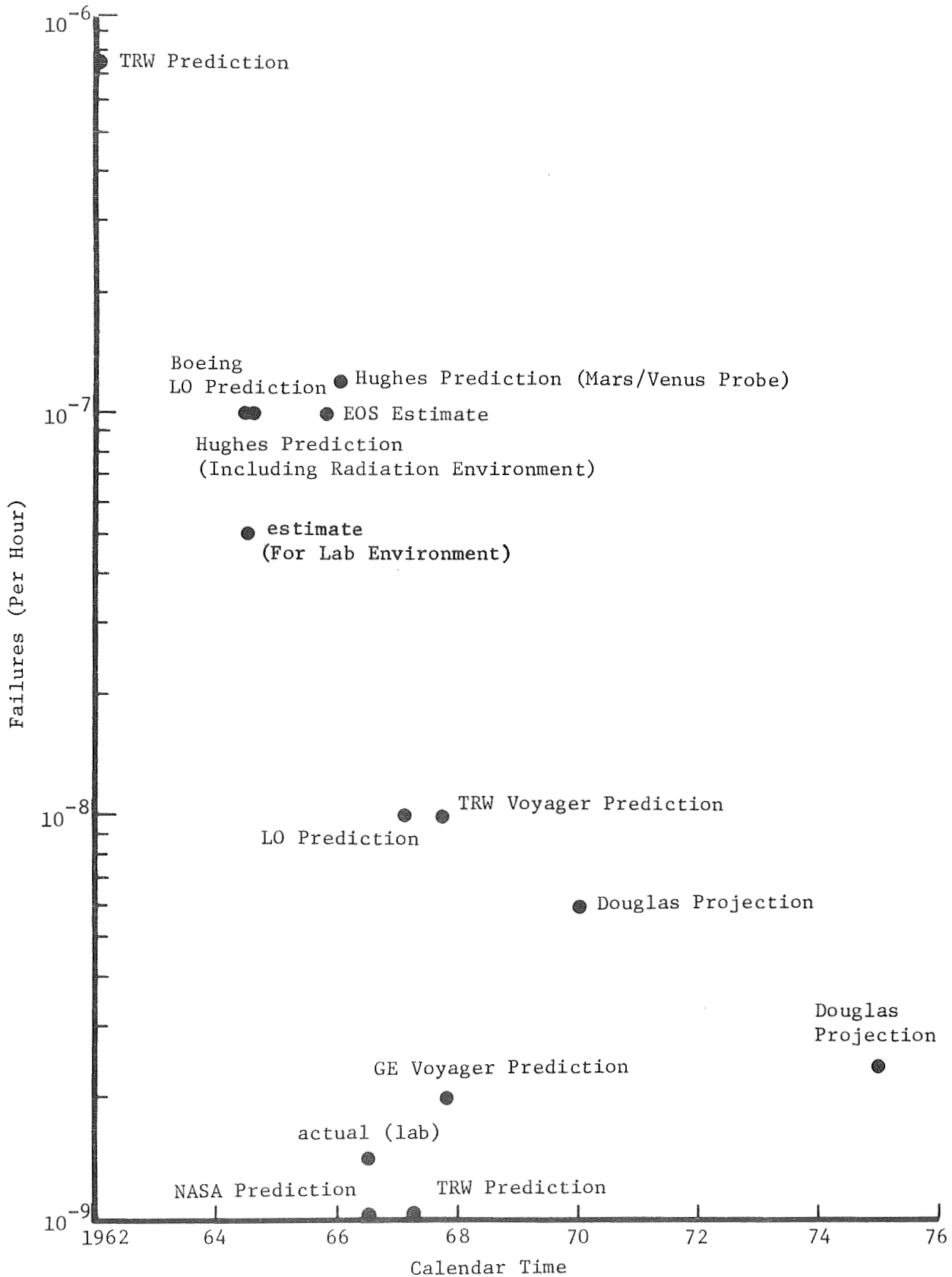


Figure 24: SILICON SOLAR CELL FAILURE RATES

meteoroid impacts. The meteoroids will erode the cover surface and occasionally puncture the cell. A puncture may or may not affect significantly the cell output. It is difficult to estimate a more precise meteoroid failure rate because of the many uncertainties in the masses of particles, the flux-size distribution, and the ultimate effect of a penetration on a solar cell (Reference 28).

Including allowances for thermal cycling and the meteoroid environment, a total solar cell failure rate for all causes was established at 1.8×10^{-8} failures per hour. Data indicate that cell shorts are much less likely to occur than opens (Reference 29). Assuming 70 percent of the failures are open circuit, and 30 percent are short circuit failures, the failure rate by mode of failure was established:

Open - 1.3×10^{-8} failures per hour

Short - 0.5×10^{-8} failures per hour

Effects of Shunting Diode Failure

Reviews of industry sources indicate that general purpose diodes have a predicted failure rate in the range $0.20 - 2.0 \times 10^{-8}$ failures per hour, (References 30, 31, 32). A conservative value of 2.0×10^{-8} was selected for the reliability analysis to account for thermal-cycling, radiation, and micro-meteoroid effects. We also searched for data on the most probable modes of failure. We found that 30 to 70 percent of general-purpose diode failures are open circuit. The average value of 50 percent was adopted, making an open or short circuit failure rate of 1.0×10^{-8} failures per hour. The probability of either an open or short circuit failure of a shunting diode was then calculated, using the exponential:

$$\begin{aligned} P_f &= 1 - e^{-\lambda_o t} \\ &= 1 - e^{-(1.0 \times 10^{-8})(4.6 \times 10^4)} \\ &= 0.00046 \end{aligned} \quad (17)$$

Open Circuit Failures

An open circuit diode failure will have no effect on array power output unless one or more cells in the same submodule also fail open. Cumulative expected array power loss from these failures was calculated as 0.00014 percent as shown in the following table:

Number of Open Circuit Cell Failures	Probability of Occurrence	Probability of Open Circuit Diode Failure	Combined Probability	Expected Array Power Loss (Watts)
1	5.944×10^{-3}	4.6×10^{-6}	2.73×10^{-6}	0.0180
2	1.777×10^{-5}		8.16×10^{-9}	0.0032
3	3.0×10^{-8}		1.38×10^{-11}	2.1×10^{-9}
4 - 10	Neg.		Neg.	Neg.
TOTAL				0.0212 Watts 0.00014%

The power loss calculations were based on:

- 0.4 volts per cell
- 40,000 submodules per array
- 0.30 volts per submodule with 1 cell open
- 10 volts per submodules with 2 cells open, no diode
- 40 volts per submodule with 3 cells open, no diode.

Diode Short Circuit Failures

A diode short circuit failure results in loss of submodule power. This failure rate is, therefore, added to the submodule failure rate due to solar cell failures to provide the expected number of submodules with degraded output or loss of power.

Submodule Failure Risk Calculation

The failure effect considered in this analysis is loss of power caused by either an open or short circuit cell failure or by a diode short circuit failure. The failure risk associated with submodule failures depends on the margin provided in design for these failures. The failure risk decreases as additional design margin in the form of extra submodules is provided. Figure 25 shows how the solar array failure risk is affected by this design margin. The failure risk was determined from tables of the cumulative terms of the Poisson distribution (Reference 33) where the failure risk (P_f) is expressed as:

$$P_f = 1 - \sum_{r=0}^x \left[\frac{e^{-n\lambda t} (n\lambda t)^r}{r!} \right]^{16/v} \quad (18)$$

where x = the number of surplus submodules provided per voltage block
 r = number of submodule failures
 n = number of submodules per voltage block including surplus
 λ = submodule failure rate
 t = operating time
 v = block voltage in thousands of volts

For illustration, voltage blocks of 1 kV, 2 kV and 4 kV were used in the analysis. Figure 25 shows that the design margin required for a given failure risk is inversely proportional to the size of the voltage block.

Failure Risk from Interconnector Failure

The primary failure mode of interconnectors is open circuit due to thermal cycling. Consideration was also given to the possibility of plasma current collected at the interconnector heating the interconnector, affecting its flexibility. Such heating turned out to be trivial.

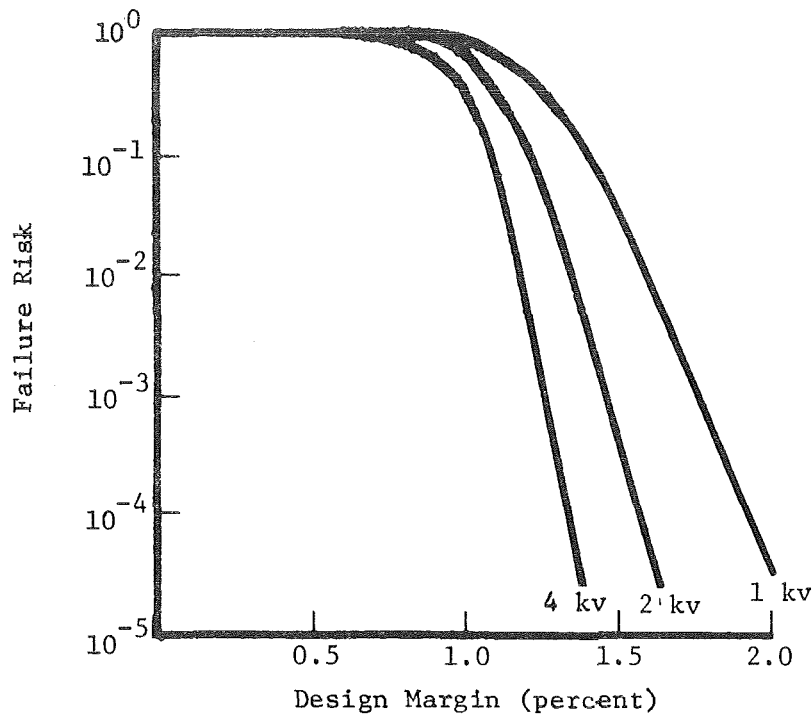


Figure 25: SOLAR ARRAY FAILURE RISK DUE TO SUBMODULE FAILURE

The results of thermal cycling tests conducted by the Applied Physics Laboratory of Johns Hopkins University on the OSCAR O-13 solar panels used on the TRANSIT program were used in developing a failure for interconnectors. These 250 thermal cycles indicated an increasing failure rate as thermal cycles accumulated. Extrapolating these data to the number of thermal cycles anticipated during the 5 year high voltage array mission resulted in the following failure rate:

<u>Mode of Failure</u>	<u>Failure Rate</u>
Solder connection failure	9.0×10^{-5} failures/thermal cycle
Torn tab or titanium silver pull-away	3.5×10^{-5} failures/thermal cycle

The extrapolation is almost one order of magnitude in number of thermal cycles (250 to 1890). Johns Hopkins had recommended a design fix to correct the failures which were experienced during the tests. This should reduce the failure rates shown. On the other hand, the insulated interconnectors in the high voltage array are less flexible, and thus may have a higher failure rate

in thermal cycling. For these reasons, the extrapolated failure rate was not adjusted to account for improvements in design.

Applying the above failure rates, assuming redundant solder connections on each interconnector tab, and redundant interconnectors between submodules, the failure probability due to interconnector failure was calculated as 1.226×10^{-9} /thermal cycle. Assuming 1890 thermal cycles per mission resulted in a failure probability of 2.32×10^{-6} . With 32,640 submodules in the array, the failure risk due to interconnector failure is 0.073 for the mission, a value too high for a mission reliability goal ≥ 0.99 . Adding a third interconnector between submodules brings the failure risk for the mission due to interconnector failure to 2.62×10^{-6} which is satisfactory.

The interconnector design being considered for the high voltage solar array is a continuous mesh interconnector soldered or bonded to each solar cell in the submodule. If one assumes that any one connection point on both edges of the interconnector is sufficient to provide electrical continuity between submodules, then the probability of failure will be significantly less than what was calculated above. However, the effect of insulating the interconnector on its flexibility is at this time unknown, and until further test data are developed the risk of failure is assumed to be the calculated value corresponding to three parallel interconnectors.

Failure Risk Due to Bus Failure and Block-to-Bus Connector Failure

It is assumed that failure of the array busses is unlikely. Aside from general structural failure of the busses and bus-to-bus shorts, no other failure modes exist. The risk of such failure is estimated as 10^{-6} , assuming that the design is good, that an adequate quality control program is maintained, and no gross defects are generated in manufacturing. The critical failure mode is open failure of the block-to-bus connectors, producing loss of block voltage.

The conceptual array design has eight 2000 volt blocks. Assuming redundant block connectors and redundant solder joints per connection point, the probability of failure per connection point, using the connector failure rate derived for the preceding analysis, is 1.23×10^{-9} /thermal cycle. The total failure probability, assuming 1890 thermal cycles and 16 interconnections is 3.72×10^{-5} . If a third interconnector is added at each connection point, the total failure probability is reduced to 1.3×10^{-9} .

Failure Risk Due to Insulation Failure

The problems in insulating solar cells and their interconnectors will be in obtaining uniform thickness without voids or discontinuities. The cover glass will insulate most of the cell surface, but there will be exposed edges, corners and interconnector attachment areas. Busses can be conventional Kapton insulated flat conductors. The required filling of intercell spaces with void-free dielectric could generate high mechanical stress with conventional designs. The problem that is anticipated is placing the filler material under the expansion joint on the solar cell. The filler material would reduce the effectiveness of the expansion joint and subsequently the flexibility of the panel.

It is extremely difficult at this time to predict a failure risk associated with insulation. No applicable quantitative data could be found. It appears that the reliability of insulating materials is affected by the design specifications for a given application. It appears to us that achievement of an insulation failure risk goal depends on developing a thorough insulating specification, accompanying documented processes, and quality control procedures.

8.0

CONCLUSIONS

The study of a high voltage solar array produced the following significant conclusions. Some of the conclusions are provisional in that further analytical and/or experimental verification is required.

Firm Conclusions

- o Generating spacecraft power at voltages between 2 and 16 kV directly with series connected silicon solar cells is feasible.
- o Our understanding of the space environment between 100 nautical miles altitude and synchronous-orbit altitude is adequate for high voltage solar array development.
- o Micrometeoroids in Earth-orbit space will penetrate 6 mil quartz covers on a 144 square meter array an average of six times per day.
- o The reliability goal of a 0.99 probability of design power being available after 5 years may be achieved by the high voltage solar array having submodules shunted with diodes, redundant connections, and about 1.8 percent extra series submodules to compensate for failures.

Provisional Conclusions - subject to indicated confirmation.

- o The high voltage solar array should be completely insulated unless a power loss can be tolerated. Confirmation requires computation of leakage current to the plasma from exposed conduction surfaces, confirmed by tests in simulated ionospheric plasma.
- o Quartz is a good insulation in a plasma environment. Other useful insulations, such as Union Carbide's Parylene C which can be vacuum deposited, need to be tested in simulated space environment to establish for design purposes long-term mechanical and physical characteristics (e.g., dielectric strength, surface conductivity, tolerable imperfections). Oxidation effects on polymer surfaces in an oxygen-containing plasma need to be established by test.
- o The ability of insulation to sustain non-destructive breakdown in a plasma environment is important. Instruments such as the Duoplasmatron, ionospheric plasma simulator, and current-limited dielectric tester, are useful in establishing insulation breakdown characteristics in plasma, as well as for exploring fields and current collection phenomena in plasma.
- o Insulation voids in the high voltage array may have to be restricted to 0.0003 inches in size (7.5×10^{-4} cm). Conventional fused-silica solar cell covers would contain too many and too big voids. However, the electric activity in a void in insulation which is stressed by a current-limited plasma dc source requires further research for full understanding.
- o Secondary electrons emitted from array surfaces as a result of ultraviolet or positive-ion bombardment can be important only if the solar array is not completely insulated.

- o Neutral mercury will not deposit on warm illuminated solar arrays in Earth orbit. Neutral mercury released by the ion thruster can be ionized by solar radiation; however, the mercury ions will be as numerous as the plasma ions only in synchronous orbit and only within one meter of the thruster.
- o Unique problems in high voltage solar cell array fabrication are insulation, cleanliness to prevent subsequent outgassing, personnel safety, and electrical testing. Functional testing in plasma of array elements during fabrication does not seem practical; however, electrolytic-tank testing can provide required confirmation of insulation quality. Evaluation of conceptual designs indicates the manufacturing problems can be solved.

9.0 GLOSSARY OF TERMS

- Solar array - The equipment required to supply the load at any of the required voltage levels. The array consists of solar cells connected in a series of voltage building blocks, reconfiguration switches, logic, fault protection and regulation circuits, and signal-power isolation devices.
- Submodules - a group of cells connected in parallel.
- Module - a group of series-connected submodules, with a switch for shunting.
- Shunting diode - a diode connected across each submodule, to conduct current in the same direction as flows through an illuminated submodule. The diode carries the current if solar cells fail open.
- Shunting switch - a power transistor connected across a module and operating in a switching mode.
- Block - a series-connected group of modules whose voltage is regulated to a specified level.
- Blocking diode - a diode in series with each block or module.

10.0 APPENDIX 1: COMPUTER PROGRAM FOR CURRENT COLLECTION

```

FORTRAN IV  MODEL 44  PS  VERSION 3, LEVEL 3  DATE  70022

C
C  NUMERICAL SIMULATION OF THE CURRENTS COLLECTED FROM A PLASMA BY A
C  TWO DIMENSIONAL ARRAY OF INSULATOR STRIPS ON A CONDUCTING SURFACE
C
C  BECAUSE OF SYMMETRY ONLY THE PLASMA PARTICLES IN ONE HALF ARRAY
C  CYCLE ( FROM THE CENTER OF AN UNINSULATED STRIP TO THE CENTER OF
C  AN INSULATED STRIP ) ARE COMPUTED
C
0001  COMMON X,Z,VX,VZ,CUR,CP,CU,XP,XM,A,AT
0002  DIMENSION X(50,43),Z(50,43),VX(50,43),VZ(50,43),CUR(50),QM(50)
0003  1,CL(50),XP(50),XM(50)
0004  1 FORMAT(10F8.4)
0005  2 FORMAT(10F8.1)
0006  4 FORMAT(/)
0007  5 FORMAT(90A4)
0008  6 FORMAT(1H1)
C
C  C=NORMALIZED NEGATIVE CHARGE ON PLASMA PARTICLES
C  CP=NORMALIZED POSITIVE CHARGE ON CONDUCTOR
C  CMI=NORMALIZED INITIAL NEGATIVE CHARGE ON INSULATOR SURFACE
C  DQM=NORMALIZED POSITIVE ION CURRENT
C  TEMP=NORMALIZED THERMAL VELOCITY
C  H=NORMALIZED THICKNESS OF INSULATOR
C  AKC=NORMALIZED WIDTH OF UNINSULATED REGION
C  COND=NORMALIZED CONDUCTIVITY OF CONDUCTOR
C  DT=NORMALIZED COMPUTATIONAL TIME STEP
C  DISK=0. FOR INITIAL RUN,=1. FOR ALL OTHER RUNS
C
0008  READ 1,C,CP,CMI,DQM,TEMP,H,AKC,COND,DT,DISK
0009  PRINT 6
0010  PRINT 1,Q,CP,CMI,DQM,TEMP,H,AKC,COND,DT
0011  H=.01*H
0012  KE=0
0013  KC=AKC
0014  KCP=KC+1
0015  IF(DISK)15,15,20
C
C  SETS INITIAL CONDITIONS
C
0016  15 A=C.
0017  AT=0.
0018  DO 19 I=1,50
0019  AI=1
0020  IF(1-KC)16,16,17
0021  16 QM(I)=C.
0022  GO TO 18
0023  17 QM(I)=CMI
0024  18 CUR(I)=0.
0025  CU(I)=C.

```

10.0 APPENDIX 1: COMPUTER PROGRAM FOR CURRENT COLLECTION (Cont.)

```

FORTRAN IV      MODEL 44  PS      VERSION 3,  LEVEL 3  DATE  70022

C
C      PUTS CHARGES IN CENTER OF EACH X INTERVAL ( X INTERVAL=.01*ONE
C      ARRAY CYCLE )
C
0026      XP(1)=.01*AI-.005
0027      XM(1)=.01*AI-.005
0028      DO 19 J=1,43
0029      AJ=J

C
C      DISTRIBUTES PLASMA PARTICLES UNIFORMLY IN SPACE
C
0030      X(I,J)=.01*AI-.005
0031      Z(I,J)=.01*AJ-.005

C
C      GIVES PLASMA PARTICLES A CRUDE VELOCITY DISTRIBUTION
C
0032      VX(I,J)=TEMP*(-1.)*(I+J)
0033      19 VZ(I,J)=-TEMP
0034      GO TO 82
0035      20 REWIND 1

C
C      READS THE RESULTS OF THE LAST RUN FROM THE DISK
C
0036      READ(1,5)X,Z,VX,VZ,CUR,QM,CU,XP,XM,A,AT
0037      PRINT 4
0038      PRINT 2,A
0039      GO TO 82
0040      80 PRINT 6
0041      82 PRINT 4
0042      CURT=0.
0043      CMT=0.
0044      CUT=0.

C
C      REDUCES NEGATIVE CHARGE ON INSULATOR SURFACE BY UNIFORM STEADY
C      POSITIVE ION CURRENT
C
0045      DO 83 K=KCP,50
0046      83 QM(K)=QM(K)-CCM

C
C      INTEGRATES TRAJECTORIES OF PLASMA PARTICLES BY SECOND ORDER RUNGE
C      KUTTA METHOD
C
0047      DTCP=D1*Q*QP
0048      DO 500 I=1,50
0049      KS=51-I
0050      DO 500 J=1,43
0051      XIJ=X(I,J)
0052      ZIJ=Z(I,J)
0053      VXIJ=VX(I,J)

```

10.0 APPENDIX 1: COMPUTER PROGRAM FOR CURRENT COLLECTION (Cont.)

FORTRAN IV MCDL 44 PS VERSION 3, LEVEL 3 DATE 70022

```

0054      VZIJ=VZ(I,J)
0055      DX1=DT*VXIJ
0056      CZ1=DT*VZIJ
0057      DVX1=0.
0058      DVZ1=0.

C
C      FIRST INTEGRATION STEP
C
C      PLASMA PARTICLES FEEL FIELDS FROM POSITIVE CHARGES ON CONDUCTOR
C      AND NEGATIVE CHARGES ON INSULATOR SURFACE IN ONE ARRAY CYCLE
C      ( E.G. 2 CM. ) CENTERED ON PLASMA PARTICLE INITIAL X POSITIONS
C
0059      DO 100 K=1,50
0060      XPK=XP(K)
0061      XMK=XM(K)
0062      DTQM=DT*Q*QM(K)
0063      DEN=(XIJ-XPK)**2+(ZIJ+H)**2
0064      DVX1=DVX1-DTQP*(XIJ-XPK)/DEN
0065      DVZ1=DVZ1-DTQP*(ZIJ+H)/DEN
0066      DEN=(XIJ-XMK)**2+ZIJ**2
0067      DVX1=DVX1+DTQM*(XIJ-XMK)/DEN
0068      100 DVZ1=DVZ1+DTQM*ZIJ/DEN
0069      DO 110 K=KS,50
0070      XPK=XP(K)
0071      XMK=XM(K)
0072      DTQM=DT*Q*QM(K)
0073      DEN=(XIJ-1.+XPK)**2+(ZIJ+H)**2
0074      DVX1=DVX1-DTQP*(XIJ-1.+XPK)/DEN
0075      DVZ1=DVZ1-DTQP*(ZIJ+H)/DEN
0076      DEN=(XIJ-1.+XMK)**2+ZIJ**2
0077      DVX1=DVX1+DTQM*(XIJ-1.+XMK)/DEN
0078      110 DVZ1=DVZ1+DTQM*ZIJ/DEN
0079      DO 120 K=1,KS
0080      XPK=XP(K)
0081      XMK=XM(K)
0082      DTQM=DT*Q*QM(K)
0083      DEN=(XIJ+XPK)**2+(ZIJ+H)**2
0084      DVX1=DVX1-DTQP*(XIJ+XPK)/DEN
0085      DVZ1=DVZ1-DTQP*(ZIJ+H)/DEN
0086      DEN=(XIJ+XMK)**2+ZIJ**2
0087      DVX1=DVX1+DTQM*(XIJ+XMK)/DEN
0088      120 DVZ1=DVZ1+DTQM*ZIJ/DEN
0089      DX2=DT*(VXIJ+DVX1)
0090      CZ2=DT*(VZIJ+DVZ1)
0091      CVX2=0.
0092      DVZ2=0.

C
C      SECOND INTEGRATION STEP
C

```

10.0 APPENDIX 1: COMPUTER PROGRAM FOR CURRENT COLLECTION (Cont.)

FORTRAN IV MODEL 44 PS VERSION 3, LEVEL 3 DATE 70022

```

C
C   PLASMA PARTICLES FEEL FIELDS FROM POSITIVE CHARGES ON CONDUCTOR
C   AND NEGATIVE CHARGES ON INSULATOR SURFACE IN ONE ARRAY CYCLE
C   ( E.G. 2 CM. ) CENTERED ON PLASMA PARTICLE INITIAL X POSITIONS
C
0093      DO 200 K=1,50
0094          XPK=XP(K)
0095          XMK=XM(K)
0096          CTQM=DT*Q*CM(K)
0097          DEN=(XIJ+DX1-XPK)**2+(ZIJ+DZ1+H)**2
0098          DVX2=DVX2-CTQP*(XIJ+DX1-XPK)/DEN
0099          DVZ2=DVZ2-CTQP*(ZIJ+DZ1+H)/DEN
0100          DEN=(XIJ+DX1-XMK)**2+(ZIJ+DZ1)**2
0101          DVX2=DVX2+CTQM*(XIJ+DX1-XMK)/DEN
0102      200  DVZ2=DVZ2+CTQM*(ZIJ+DZ1)/DEN
0103          DO 210 K=KS,50
0104          XPK=XP(K)
0105          XMK=XM(K)
0106          CTQM=DT*Q*CM(K)
0107          DEN=(XIJ+DX1-1.+XPK)**2+(ZIJ+DZ1+H)**2
0108          DVX2=DVX2-CTQP*(XIJ+DX1-1.+XPK)/DEN
0109          DVZ2=DVZ2-CTQP*(ZIJ+DZ1+H)/DEN
0110          DEN=(XIJ+DX1-1.+XMK)**2+(ZIJ+DZ1)**2
0111          DVX2=DVX2+CTQM*(XIJ+DX1-1.+XMK)/DEN
0112      210  DVZ2=DVZ2+CTQM*(ZIJ+DZ1)/DEN
0113          DO 220 K=1,KS
0114          XPK=XP(K)
0115          XMK=XM(K)
0116          CTQM=DT*Q*CM(K)
0117          DEN=(XIJ+DX1+XPK)**2+(ZIJ+DZ1+H)**2
0118          DVX2=DVX2-CTQP*(XIJ+DX1+XPK)/DEN
0119          DVZ2=DVZ2-CTQP*(ZIJ+DZ1+H)/DEN
0120          DEN=(XIJ+DX1+XMK)**2+(ZIJ+DZ1)**2
0121          DVX2=DVX2+CTQM*(XIJ+DX1+XMK)/DEN
0122      220  DVZ2=DVZ2+CTQM*(ZIJ+DZ1)/DEN
0123          XI(J)=XIJ+.5*(DX1+DX2)
0124          Z(I,J)=ZIJ+.5*(DZ1+DZ2)
0125          VX(I,J)=VXIJ+.5*(DVX1+DVX2)
0126      500  VZ(I,J)=VZIJ+.5*(DVZ1+DVZ2)
C
C   INTEGRATES TRAJECTORIES OF CHARGES ON CONDUCTOR BY SECOND ORDER
C   RUNGE KUTTA METHOD
C
0127      BTPPC=DT*QP*(P*COND
0128          DO 600 I=1,50
0129          KS=51-I
0130          XPI=XP(I)
0131          CXPI=0.
C

```

10.0 APPENDIX 1: COMPUTER PROGRAM FOR CURRENT COLLECTION (Cont.)

FORTRAN IV MODEL 44 PS VERSION 3, LEVEL 3 DATE 70022

```

C      FIRST INTEGRATION STEP
C
C      CHARGES ON CONDUCTOR FEEL FIELDS FROM OTHER POSITIVE CHARGES ON
C      CONDUCTOR AND NEGATIVE CHARGES ON INSULATOR SURFACE IN ONE ARRAY
C      CYCLE ( E.G. 2 CM. ) CENTERED ON CHARGE INITIAL X POSITIONS
C
0132      DO 520 K=1,50
0133          XPK=XP(K)
0134          XPK=XM(K)
0135          DTPMC=DT*QP*QM(K)*COND
0136          IF (I-K) 510,520,510
0137      510      DXP1=DXP1+CTPPC/(XPI-XPK)
0138      520      DXP1=DXP1-DTPMC*(XPI-XMK)/((XPI-XMK)**2+H**2)
0139          DO 530 K=KS,50
0140              XPK=XP(K)
0141              XMK=XM(K)
0142              DTPMC=DT*QP*QM(K)*COND
0143              DXP1=DXP1+CTPPC/(XPI-1.+XPK)
0144      530      DXP1=DXP1-DTPMC*(XPI-1.+XMK)/((XPI-1.+XMK)**2+H**2)
0145          DO 540 K=1,KS
0146              XPK=XP(K)
0147              XMK=XM(K)
0148              DTPMC=DT*QP*QM(K)*COND
0149              DXP1=DXP1+CTPPC/(XPI+XPK)
0150      540      DXP1=DXP1-DTPMC*(XPI+XMK)/((XPI+XMK)**2+H**2)
0151          DXP2=0.
C
C      SECOND INTEGRATION STEP
C
C
C      CHARGES ON CONDUCTOR FEEL FIELDS FROM OTHER POSITIVE CHARGES ON
C      CONDUCTOR AND NEGATIVE CHARGES ON INSULATOR SURFACE IN ONE ARRAY
C      CYCLE ( E.G. 2 CM. ) CENTERED ON CHARGE INITIAL X POSITIONS
C
0152      DO 560 K=1,50
0153          XPK=XP(K)
0154          XPK=XM(K)
0155          DTPMC=DT*QP*QM(K)*COND
0156          IF (I-K) 550,560,550
0157      550      DXP2=DXP2+CTPPC/(XPI+DXP1-XPK)
0158      560      DXP2=DXP2-DTPMC*(XPI+DXP1-XMK)/((XPI+DXP1-XMK)**2+H**2)
0159          DO 570 K=KS,50
0160              XPK=XP(K)
0161              XPK=XM(K)
0162              DTPMC=DT*QP*QM(K)*COND
0163              DXP2=DXP2+CTPPC/(XPI+DXP1-1.+XPK)
0164      570      DXP2=DXP2-DTPMC*(XPI+DXP1-1.+XMK)/((XPI+DXP1-1.+XMK)**2+H**2)
0165          DO 580 K=1,KS
0166              XPK=XP(K)

```

10.0 APPENDIX 1: COMPUTER PROGRAM FOR CURRENT COLLECTION (Cont.)

```

FORTRAN IV      MODEL 44  PS      VERSION 3,  LEVEL 3  DATE  70022

0167             XMK=XM(K)
0168             DTPMC=DT*CP*QM(K)*COND
0169             DXP2=DXP2+DTPPC/(XPI+DXPI+XPK)
0170             580 DXP2=DXP2-DTPMC*(XPI+DXPI+XMK)/((XPI+DXPI+XMK)**2+H**2)
0171             600 XPI=XPI+.5*(DXPI+DXP2)

C
C   REFLECTS TRAJECTORIES OF PLASMA PARTICLES BACK INTO COMPUTED
C   REGION ( X=C TO .5 ) IF ANY LEAVE
C
0172             DO 740 I=1,50
0173             DO 740 J=1,43
0174             IF(X(I,J))710,720,720
0175             710 X(I,J)=-X(I,J)
0176             VX(I,J)=-VX(I,J)
0177             GO TO 740
0178             720 IF(X(I,J)-.5)740,740,730
0179             730 X(I,J)=1.-X(I,J)
0180             VX(I,J)=-VX(I,J)
0181             740 CONTINUE

C
C   COLLECTS CHARGES IF THEY PASS THE PLANE OF THE INSULATOR SURFACE
C
0182             DO 850 I=1,50
0183             DO 850 J=1,43
0184             IF(Z(I,J))750,800,800
0185             750 L=100.*X(I,J)+1.
0186             IF(L-KC)760,760,770

C
C   CHARGES CONTRIBUTE TO CURRENT TO CONDUCTOR IF THEY ARE IN THE
C   UNINSULATED REGION
C
0187             760 CUR(L)=CUR(L)+Q
0188             CURT=CURT+Q
0189             GO TO 780

C
C   CHARGES ARE PUT IN THE CENTER OF THE X INTERVAL ON WHICH THEY LAND
C   IF THEY ARE IN THE INSULATED REGION
C
0190             770 QM(L)=QM(L)+Q
0191             QMT=QMT+Q
0192             780 A=A+1.
0193             AT=AT+1.
0194             IA=A

C
C   THE LABELS OF THE COLLECTED CHARGES ARE ASSIGNED TO NEW CHARGES
C   WITH PRESCRIBED POSITIONS AND VELOCITIES
C
0195             X(I,J)=.01*A-.005
0196             Z(I,J)=.5

```

10.0 APPENDIX 1: COMPUTER PROGRAM FOR CURRENT COLLECTION (Cont.)

```

FORTRAN IV      MCDL 44  PS      VERSION 3, LEVEL 3  DATE  70022

0197              VX(I,J)=TEMP*(-1.)*(IA+J)
0198              VZ(I,J)=-TEMP
0199              IF(A-50.)800,790,790
0200              790 A=A-50.
C
C              COUNTS THE CHARGES THAT LEAVE THE VICINITY OF THE ARRAY
C
0201              800 IF(Z(I,J)-1.)850,810,810
0202              810 L=100.*X(I,J)+1.
0203              CU(L)=CU(L)+Q
0204              CUT=CUT+Q
0205              A=A+1.
0206              AT=AT+1.
0207              IA=A
C
C              THE LABELS OF THE ESCAPED CHARGES ARE ASSIGNED TO NEW CHARGES
C              WITH PRESCRIBED POSITIONS AND VELOCITIES
C
0208              X(I,J)=.01*A-.005
0209              Z(I,J)=.5
0210              VX(I,J)=TEMP*(-1.)*(IA+J)
0211              VZ(I,J)=-TEMP
0212              IF(A-50.)850,820,820
0213              820 A=A-50.
0214              850 CONTINUE
C
C              AT=NORMALIZED TOTAL CHARGE COLLECTED
C              CUR(K)=NORMALIZED TOTAL CHARGE COLLECTED BY EACH UNINSULATED X
C              INTERVAL
C              CURT=NORMALIZED TOTAL CHARGE COLLECTED BY UNINSULATED REGION
C              CM(K)=NORMALIZED CHARGE ON EACH INSULATED X INTERVAL
C              GMT=NORMALIZED TOTAL CHARGE COLLECTED BY INSULATED REGION
C              CU(K)=NORMALIZED TOTAL ESCAPED CHARGE THROUGH EACH X INTERVAL
C              CUT=NORMALIZED TOTAL ESCAPED CHARGE
C              XP(K)=POSITIONS OF THE POSITIVE CHARGES ON THE CONDUCTOR
C
0215              PRINT 4
0216              PRINT 2,AT,CURT,GMT,CUT
0217              PRINT 4
0218              PRINT 2,(CUR(K),K=1,KC),(CM(K),K=KCP,50)
0219              PRINT 4
0220              PRINT 2,(CU(K),K=1,50)
0221              PRINT 4
0222              PRINT 1,(XP(K),K=1,50)
0223              KE=KE+1
C
C              CHANGE THE NEXT FORTRAN CARD DEPENDING ON HOW MANY 3 MINUTE TIME
C              STEPS THERE ARE IN THE ALLOWED COMPUTATION TIME
C

```


10.0 APPENDIX 1: COMPUTER PROGRAM FOR CURRENT COLLECTION (Cont.)

```

FORTRAN IV      MODEL 44 PS      VERSION 3, LEVEL 3      DATE 70022
0224              IF (KE- 2)80,900,900
0225              900 CONTINUE
0226              REWIND 1
                  C
                  C      STORES THE RESULTS ON THE DISK TO BE USED IN THE NEXT RUN
                  C
0227              WRITE(1,5)X,Z,VX,VZ,CUR,QM,CU,XP,XM,A,AT
0228              STOP
0229              END

```

11.0 APPENDIX 2: DETERMINATION OF NET ACCELERATING VOLTAGE PRODUCED BY A SOLAR ARRAY OPERATING AN ION THRUSTOR

Statement of Problem

Assume that a solar array operates an ion thruster at a constant ion beam current in the ionosphere. Determine how the net accelerating potential produced by the array is affected by given densities of electron and ion currents collected from the plasma.

Basic Approach

We assume that at least part of the solar array has a positive potential relative to the plasma and collects electrons from the plasma with a uniform current density of ρ_e . The voltage output of each cell is then determined as a function of its position along the length of the array. From this information, the voltage gradient is determined as a function of position. The length of the positive portion of the array is then determined as a function of (1) excess neutralizer current (I_{excess}), (2) electron current density (ρ_e) collected by the positive portion of the array, and (3) ion current density (ρ_i) collected by the negative portion of the array. The total voltage produced by the positive portion of the array is then calculated by integrating the voltage gradient over the positive portion of the array.

The resulting voltage is the net accelerating potential which operates the ion thruster and depends upon I_{excess} , ρ_e and ρ_i .

Assumed Array Characteristics

The solar array (Figure 26) is composed of N_s rows connected in series to form a string L -cm long. Each row contains N_p cells connected in parallel so that the string is W -cm wide.

The cells are silicon solar cells with the I-V characteristic shown in Figure 27.

The negative end of the array is connected to the neutralizer and the vehicle skin.

The currents which flow between the array, thruster, vehicle skin, and plasma are shown in Figure 28.

Mathematical Representation of Solar Cell I-V Curve

If the array did not collect electrons from the plasma, each solar cell would operate near the maximum power point shown in Figure 27. When the array collects electrons from the plasma, the cells must carry more than the current at maximum power. Therefore the cells may operate at currents between maximum power current (0.125 amp) and short circuit current (0.149 amp). The voltage of the cells consequently varies between maximum power voltage and zero. In order to calculate the total array voltage it is necessary to represent mathematically the relationship between cell current and cell voltage in the region between maximum power and short circuit current.

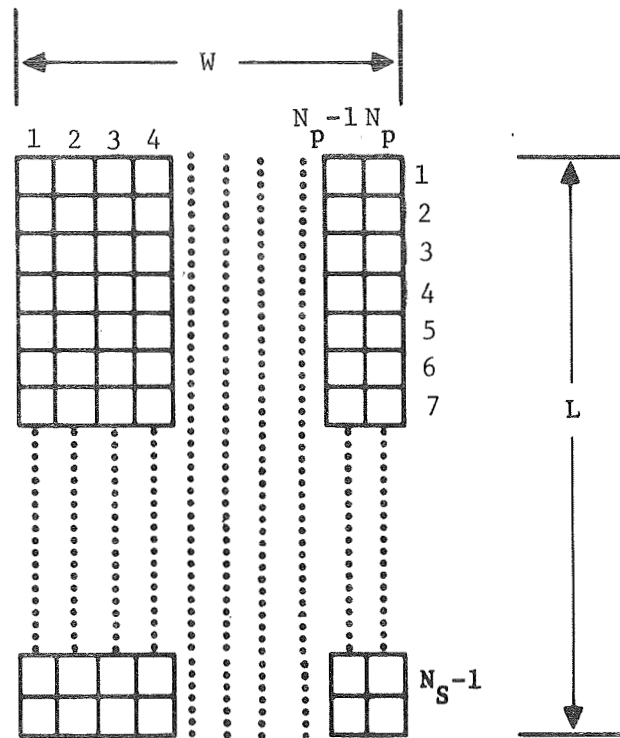


Figure 26: SOLAR ARRAY CONFIGURATION

Cell Characteristics:

Heliotek
N/P
10 ohm-cm
 $\eta = 10.3\% @ 30^\circ\text{C}$
Bare Cell
2x2 cm x 0.012-inch

Cell Temperature:

55°C

Light Intensity:

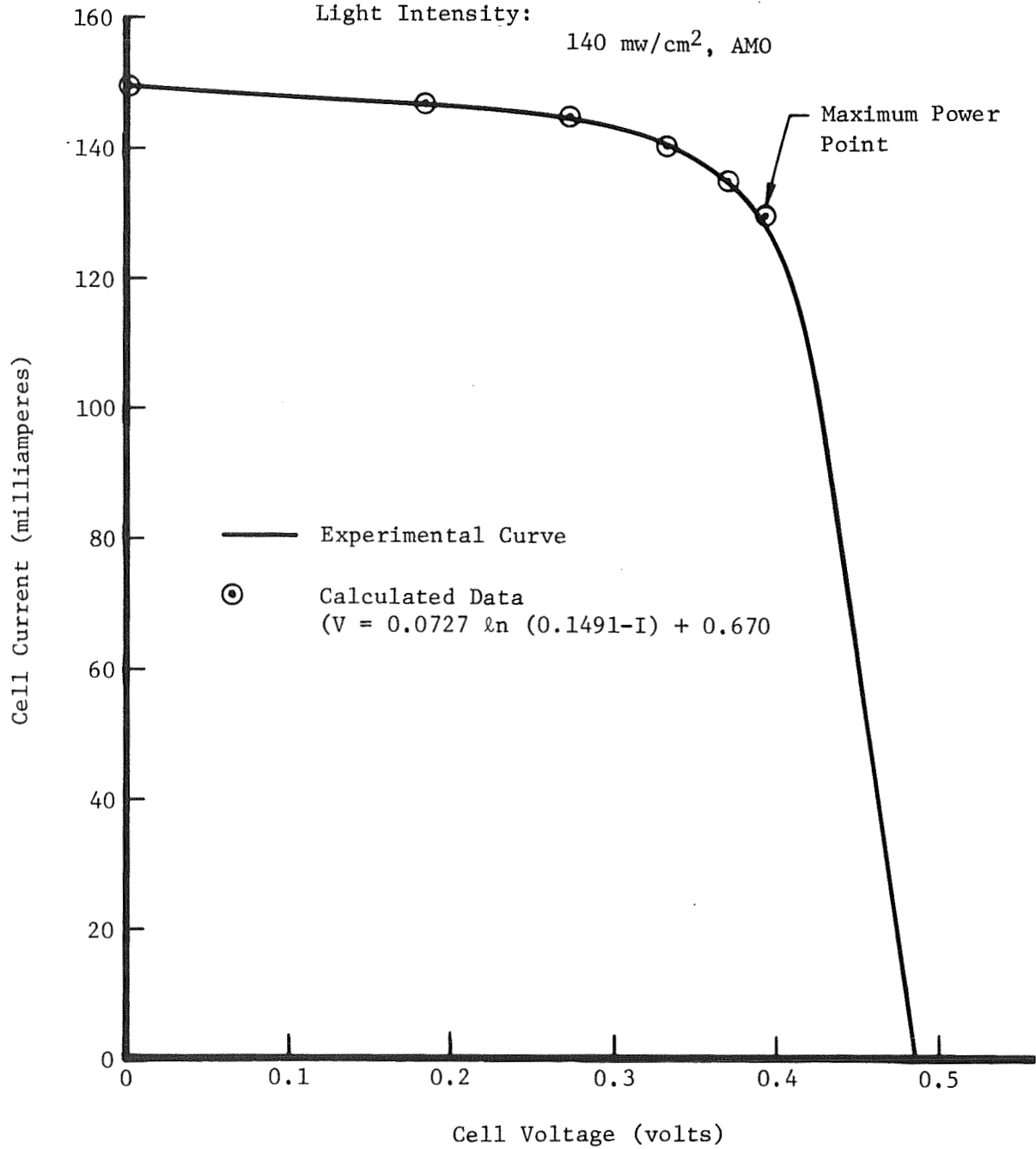
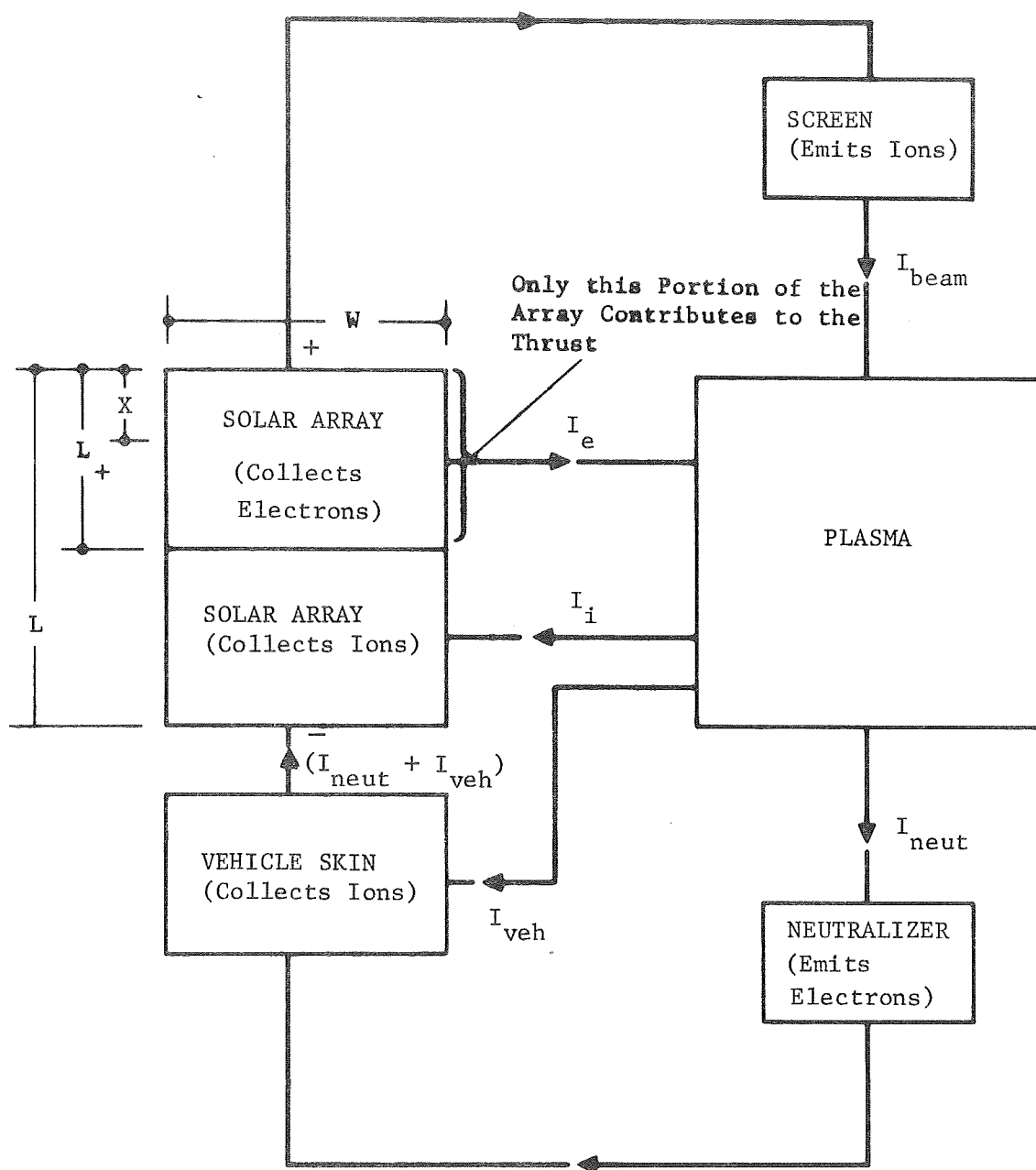
140 mw/cm², AM0

Figure 27: I-V CURVE FOR A SILICON SOLAR CELL



Arrows indicate direction of positive current flow

Figure 28: CURRENT FLOW BETWEEN ARRAY, THRUSTOR, AND PLASMA

A very good fit to the I-V curve in Figure 27 for the region between maximum power and short circuit current is attained with the following equation:

$$V = C_1 [\ln (C_2 - I)] + C_3 \quad (19)$$

where

$$C_1 = 0.0727$$

$$C_2 = 0.1491$$

$$C_3 = 0.670$$

The data points shown in Figure 27 were calculated from Equation 19.

In order to calculate the relationship between the voltage and current of a row of N_p parallel-connected cells we make the substitutions

$$V = V_{\text{row}} \quad \text{and}$$

$$I = \frac{I_{\text{row}}}{N_p}$$

in Equation 19 to get

$$V_{\text{row}} = C_1 [\ln(C_2 - I_{\text{row}}/N_p)] + C_3 \quad (20)$$

Distribution of Current in the Array

If the array did not collect electrons from the plasma, each row of N_p parallel-connected cells would carry a current equal to the ion beam current:

$$I_{\text{row}} = I_{\text{beam}} \quad (21)$$

However, if the cells did collect electrons from the plasma at a uniform current density of ρ_e , the current carried by a given row of cells would depend upon how far the row was located from the most positive end of the array:

$$I_{\text{row}} = I_{\text{beam}} + \rho_e Wx \quad (22)$$

where W is the width of the row and x is the distance of the row from the most positive end of the array (see Figure 28).

If the entire array is positive, then Equation 22 is valid for the entire length of the array. If only part of the array is positive, then a different expression for I_{row} is required for the remainder of the array. Providing I_{row} never becomes so large that the row voltage drops to zero, the remainder of the array will attain a negative potential and the expression for row current becomes:

$$I_{\text{row}} = I_{\text{beam}} + \rho_e WL_+ - \rho_i W(x - L_+) \quad (23)$$

where ρ_1 = ion current density collected by the array from the plasma

L_+ = length of positive portion of the array

This general situation, where there exists both positive and negative portions of the array, is shown in Figure 28. Note that in this situation, the vehicle skin also becomes negative and collects ions from the plasma. When part of the array and vehicle become negative, the ion engine loses thrust because only the positive portion of the array contributes to the net accelerating potential of the ion engine.

The value of L_+ is determined by the equilibrium condition that the net current flow from the plasma to the array-thruster system is zero:

$$I_{\text{neut}} - I_{\text{beam}} + I_{\text{veh}} + I_1 - I_e = 0 \quad (24)$$

$$\text{where } I_e = \rho_e W L_+ \quad (25)$$

$$I_1 = \rho_1 W (L - L_+) \quad (26)$$

$$I_{\text{veh}} = \rho_{\text{veh}} A_{\text{veh}} \quad (27)$$

ρ_{veh} = ion current density collected by the vehicle skin from the plasma

A_{veh} = effective ion collection area of vehicle skin

The quantity $(I_{\text{neut}} - I_{\text{beam}})$ represents the excess electron current emitted by the neutralizer:

$$I_{\text{excess}} = I_{\text{neut}} - I_{\text{beam}} \quad (28)$$

Substituting Equations 25, 26, 27, and 28 into Equation 24 and rearranging we get:

$$L_+ = \frac{I_{\text{excess}} + \rho_1 W L + \rho_{\text{veh}} A_{\text{veh}}}{(\rho_e + \rho_1) W} \quad (29)$$

There are two different conditions under which Equation 29 is not valid:

- (1) When the entire array is positive, $L_+ = L$ and the neutralizer current is given by $I_{\text{excess}} = \rho_e W L$
- (2) When the current in one of the rows becomes so large that the row voltage drops to zero. This occurs when the individual cells carry 0.149 amperes (short circuit current) or $I_{\text{row}} = (N_p)(0.149 \text{ amp})$.
Under this condition:

$$N_p (0.149 \text{ amp}) = I_{\text{beam}} + \rho_e W L_+$$

or

$$L_+ = \frac{N_p (0.149 \text{ amp}) - I_{\text{beam}}}{\rho_e W} \quad (30)$$

The potential of the remainder of the array and the vehicle skin adjusts approximately to that of the plasma and does not collect a net current from the plasma.

In this case the excess neutralizer current is given by

$$I_{\text{excess}} = N_p (0.149 \text{ amp}) - I_{\text{beam}} \quad (31)$$

The current distribution in the array as a function of distance along the array is shown in Figure 29 for the three cases:

$$(1) \quad L_+ = L ; (\text{Entire array positive}) \quad (32)$$

$$(2) \quad L_+ = \frac{I_{\text{excess}} + \rho_1 WL + \rho_{\text{veh}} A_{\text{veh}}}{(\rho_e + \rho_1) W} ; \quad (33)$$

(Part of array positive and remainder negative)

$$(3) \quad L_+ = \frac{N_p (0.149 \text{ ma}) - I_{\text{beam}}}{\rho_e W} ; \quad (34)$$

(Part of array positive, and remainder at plasma potential)

Distribution of Voltage in the Array

The voltage output of any row of cells in the entire array is given by Equation 20 and is repeated here:

$$V_{\text{row}} = C_1 \ln (C_2 - I_{\text{row}}/N_p) + C_3 \quad (20)$$

where

$$C_1 = 0.0727$$

$$C_2 = 0.1491$$

$$C_3 = 0.670$$

$$N_p = \text{number of parallel-connected cells in the row.}$$

The current through a row in the positive portion of the array is a function of where the row is located as indicated by Equation 22 which is repeated here:

$$I_{\text{row}} = I_{\text{beam}} + \rho_e Wx \quad (22)$$

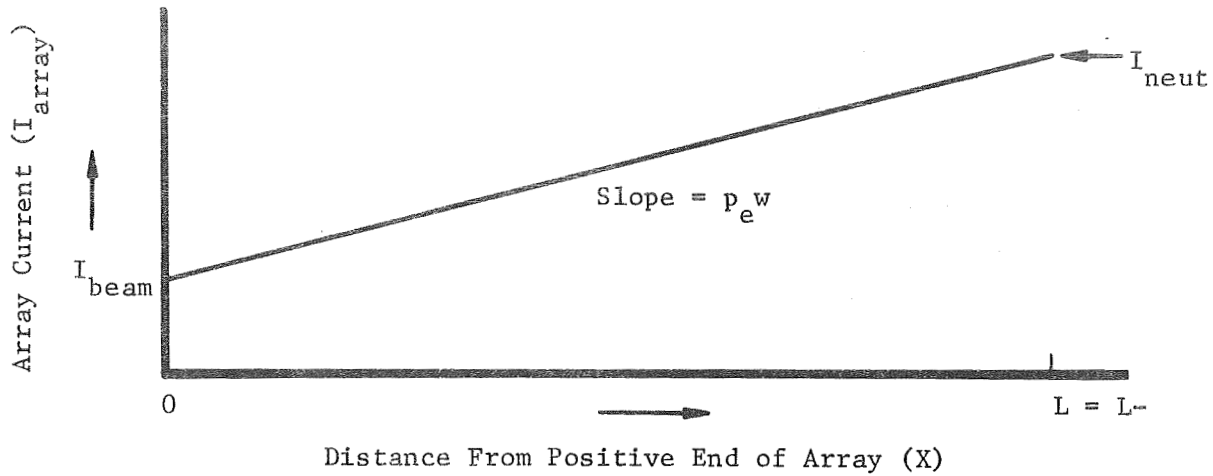
Substituting Equation 22 into Equation 20 we get row voltage as a function of position in the array:

$$V_{\text{row}} = C_1 \ln \left[C_2 - (I_{\text{beam}} + \rho_e Wx)/N_p \right] + C_3 \quad (35)$$

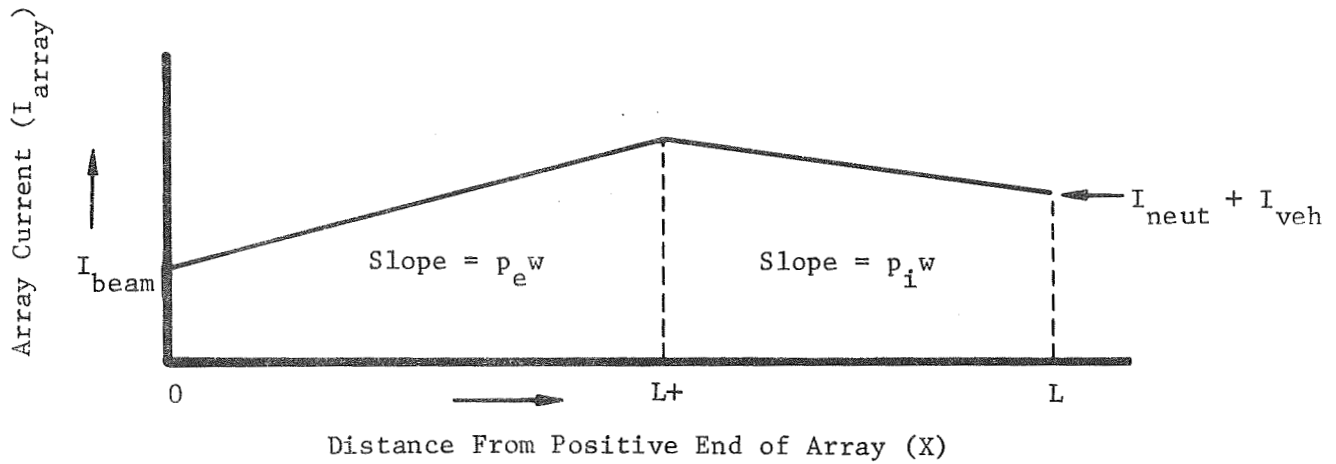
The voltage gradient $\left(\frac{dV}{dx}\right)_+$ at any place along the positive portion of the array is the row voltage divided by the cell length:

$$\begin{aligned} \left(\frac{dV}{dx}\right)_+ &= -\frac{(V_{\text{row}})}{(\text{cell length})} \\ &= -\frac{V_{\text{row}}}{L/N_s} \end{aligned} \quad (36)$$

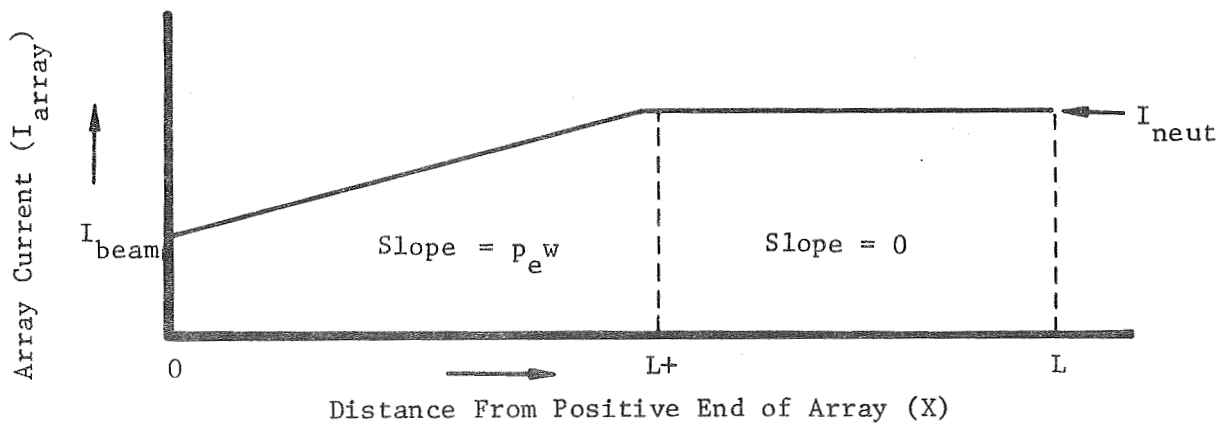
where L is the array length and N_s is the total number of rows connected in series.



(a) Entire array is positive



(b) Part of array is positive, remainder is negative



(c) Part of array is positive, remainder is at plasma potential

Figure 29: CURRENT VARIATION ALONG LENGTH OF SOLAR ARRAY

Substituting Equation 35 into Equation 36 we get

$$\left(\frac{dV}{dx}\right)_+ = \frac{N_s}{L} C_1 \ln \left[C_2 - (I_{\text{beam}} + \rho_e Wx)/N_p \right] + C_3 \quad (37)$$

Calculating Net Accelerating Voltage

The net accelerating voltage which operates the ion thruster is simply the voltage output of the positive portion of the array. To calculate this total voltage we need to integrate the voltage gradient given in Equation 37 along the length of the positive portion of the array:

$$V_{\text{net accel}} = \int_0^{L_+} \left(\frac{dV}{dx}\right)_+ dx \quad (38)$$

Substituting (37) into (38) we get:

$$\begin{aligned} V_{\text{net accel}} &= \int_0^{L_+} \left\{ \frac{N_s}{L} C_1 \ln \left[C_2 - (I_{\text{beam}} + \rho_e Wx)/N_p \right] + C_3 \right\} dx \\ &= \frac{N_s}{L} \left\{ \left(\frac{C_1 N_p}{\rho_e W} \right) \left[(U_2 \ln U_2 - U_2) - (U_1 \ln U_1 - U_1) \right] + C_3 L_+ \right\} \quad (39) \end{aligned}$$

where $U_2 = C_2 - \frac{1}{N_p} (I_{\text{beam}} + \rho_e W L_+)$

$$U_1 = C_2 - \frac{1}{N_p} I_{\text{beam}}$$

The net accelerating voltage ($V_{\text{net accel}}$) can be calculated from Equation 32. To do this it is necessary to know:

- (1) N_s , the number of rows in series
- (2) N_p , the number of cells in a row
- (3) ρ_e , the electron current density collected by the array (amps/cm²)
- (4) I_{beam} , the ion beam current (amp)
- (5) W , the width of the array (cm)
- (6) L , the length of the array (cm)
- (7) L_+ , the length of the positive portion of the array (cm)

The value of L_+ can be determined from Equation 32 if it is assumed that the neutralizer current emits an excess electron current equal in magnitude to the electron current collected by the array:

$$I_{\text{excess}} = \rho_e W L \quad (40)$$

$$L_+ = L \quad (41)$$

The value of L_+ can be determined from Equation 34 if it is assumed that the neutralizer current emits an excess electron current just large enough to make some of the cells in the array operate at their short circuit current point:

$$I_{\text{excess}} = (N_p)(0.149 \text{ amp}) - I_{\text{beam}} \quad (42)$$

$$L_+ = \frac{I_{\text{excess}}}{\rho_e W} \quad (43)$$

The value of L_+ can be determined from Equation 33 if it is assumed that the neutralizer emits an excess electron current which is less than the two limits described in the two preceding paragraphs:

$$0 \leq I_{\text{excess}} < \left\{ \begin{array}{l} \rho_e WL \\ \text{or} \\ (N_p)(0.149) - I_{\text{beam}} \end{array} \right\} \text{ whichever is smaller} \quad (44)$$

$$(N_p)(0.149) - I_{\text{beam}} \quad (45)$$

$$L_+ = \frac{I_{\text{excess}} + \rho_i WL + \rho_{\text{veh}} A_{\text{veh}}}{(\rho_e + \rho_i) W} \quad (46)$$

Note that in order to calculate L_+ in the last case, it is necessary to know the ion current density (ρ_i) collected by the negative portion of the array and the ion current density (ρ_{veh}) collected by the vehicle skin. The vehicle skin collection area (A_{veh}) is also required.

Summary of Procedure

- (1) Determine how much excess neutralizer current will be emitted. If you assume that the neutralizer emits the maximum possible, the neutralizer current is given by Equation 40 or Equation 42, whichever is smaller.
- (2) Calculate the length (L_+) of the positive portion of the array from Equation 41, Equation 43, or Equation 46, whichever is the appropriate one for the value of excess neutralizer current being used.
- (3) Calculate the net accelerating voltage from Equation 39 using the values of I_{excess} and L_+ determined in the two preceding steps.

Sample Calculation #1

Let $N_s = 7,500$
 $N_p = 40$
 $\rho_e = 4.86 \times 10^{-6} \text{ amps/cm}^2$
 $\rho_{\text{veh}} = \rho_i = 4.95 \times 10^{-7} \text{ amps/cm}^2$
 $I_{\text{beam}} = 5 \text{ amperes}$
 $W = 90 \text{ cm}$
 $L = 16,000 \text{ cm}$
 $A_{\text{veh}} = \frac{1}{10} WL = 1.44 \times 10^5 \text{ cm}^2$
 $I_{\text{excess}} = 0$

Since $I_{\text{excess}} = 0$, we use Equation 46 to determine L_+ :

$$L_+ = \frac{0 + (4.95 \times 10^{-7})(90)(1.6 \times 10^4) + (4.95 \times 10^{-7})(1.44 \times 10^5)}{(4.86 \times 10^{-6} + 4.95 \times 10^{-7})90}$$

$$= 1.63 \times 10^3 \text{ cm}$$

We calculate the net accelerating voltage from Equation 39:

$$V_{\text{net accel}} = \left(\frac{7.5 \times 10^3}{1.6 \times 10^4} \right) \left\{ (.670)(1.63 \times 10^3) - \left(\frac{(.0727)(40)}{(4.86 \times 10^{-6})(90)} \right) \left[(U_2 \ln U_2 - U_2) - (U_1 \ln U_1 - U_1) \right] \right\}$$

$$\text{where } U_2 = .1491 - \frac{1}{40} \left[5 + (4.86 \times 10^{-6})(90)(1.63 \times 10^3) \right] = 0.006$$

$$U_1 = .1491 - \frac{1}{40} (5) = 0.0241$$

$$V_{\text{net accel}} = 271 \text{ volts} \quad \leftarrow$$

Sample Calculation #2

Same as Sample Calculation #1 except let I_{excess} be at its maximum value. The maximum value that I_{excess} can attain is $\rho_e W_L$ or $(N_p)(.149) - I_{\text{beam}}$, whichever is smaller.

$$\rho_e W_L = (4.86 \times 10^{-6}) \times (90) \times (1.6 \times 10^4) = 7.00 \text{ amps}$$

$$(N_p)(.149) - I_{\text{beam}} = (40) \times (.149) - 5 = 0.96 \text{ amps}$$

Therefore $I_{\text{excess}} = 0.96$ amps is the maximum neutralizer current. This is the value of excess neutralizer current which is just large enough to make some of the cells in the array operate at their short circuit current. L_+ is therefore given by Equation 43:

$$L_+ = \frac{I_{\text{excess}}}{\rho_e W} = \frac{0.96}{(4.86 \times 10^{-6}) \times (90)} = 2.2 \times 10^3 \text{ cm}$$

The net accelerating voltage is obtained from Equation 39:

$$V_{\text{net accel}} = \left(\frac{7.5 \times 10^3}{1.6 \times 10^4} \right) \left\{ (6.70)(2.2 \times 10^3) - \frac{(.0727)(40)}{(4.86 \times 10^{-6})(90)} \left[(U_2 \ln U_2 - U_2) - (U_1 \ln U_1 - U_1) \right] \right\}$$

where

$$U_2 = .1491 - \frac{1}{40} \left\{ 5 + \left[(4.86 \times 10^{-6})(90)(2.2 \times 10^3) \right] \right\} = 0.000043$$

$$U_1 = .1491 - \frac{1}{40} (5) = 0.0241$$

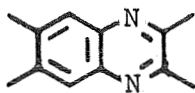
$$V_{\text{net accel}} = 334 \text{ volts} \quad \leftarrow$$

This calculation was repeated at different values of the collected electron current density, ρ_e , to obtain the curve plotted in Figure 7.

APPENDIX 3

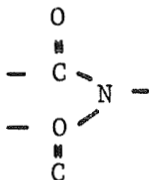
Plasma Resistance Materials---Organic

1. Polyquinoxalines

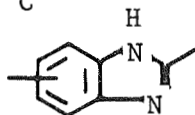


2. Epoxies

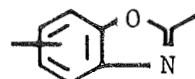
3. Polyimide



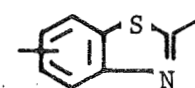
4. Polybenzimidazole



- Polybenzoxazole

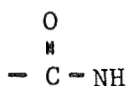


- Polybenzothiazole

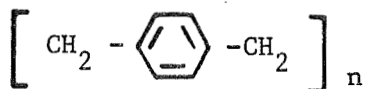


5. Mixed polyamide-imide

6. Polyamide



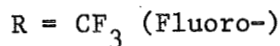
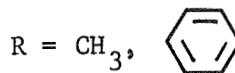
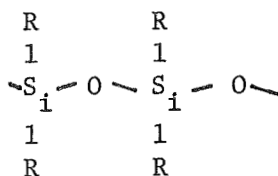
7. Poly=p-xylylene



8. Ladder polymers

9. Aromatic and pseudo-aromatic polymers

10. Silicones and fluorosilicones



Plasma Resistant Materials---Inorganic



Noble metals

Ceramics

13.0 APPENDIX 4: HIGH VOLTAGE SOLAR ARRAY SPACE ENVIRONMENT MODEL

TABLE OF CONTENTS

13.1 FOREWORD

13.2 INTRODUCTION

13.3 DESCRIPTION OF ENVIRONMENT

13.3.1 Earth's Magnetic Field

13.3.2 Neutral Atmosphere

13.3.3 Solar Spectrum

13.3.4 Auroral and Polar Storm Particles

13.3.5 Ionosphere

13.3.5.1 Sources of Information - Various Ionospheric Regions

13.3.5.2 Altitude Dependence of Ionosphere Parameters

13.3.5.3 Seasonal and Diurnal Variations

13.3.5.4 Geomagnetic Latitude Variations

13.3.5.5 Plasmaphere

13.3.6 Magnetosphere

13.3.6.1 Solar Wind and Storm Variations

13.3.6.2 Trapped Radiation

13.3.6.3 Solar Flare Activity

13.3.7 Meteoroids

13.4 ENVIRONMENTAL MODEL

13.4.1 Geomagnetic Field

13.4.2 Neutral Atmosphere

13.4.3 Solar Spectrum

13.4.4 Auroral and Polar Storm Particles

13.4.5 Ionosphere

13.4.6 Magnetosphere

13.4.7 Meteoroids

13.1 FOREWORD

This appendix summarizes the model of the space environment developed at Boeing for the High Voltage Solar Array Study.

The complete model was published earlier in Boeing document D2-12133-1.

13.2 INTRODUCTION

A high voltage solar array, traversing the region from 100 nautical miles to synchronous altitude, will encounter the natural environment present in the Earth's magnetosphere. Occasionally, solar activity will compress the Earth's magnetosphere to expose a synchronous-altitude satellite to the bow shock region. A complete description of the environment throughout the region of interest would be lengthy; hence we will restrict our description to those parameters that significantly influence the operation of a high-voltage solar array.

The ionosphere, a critical environment in the design and operation of the solar array, requires a comprehensive description in this model environment. The neutral atmosphere, in conjunction with the radiation, is the source of the ionosphere, and at low altitude the neutral atmospheric density is great enough to affect the electrical properties of the ionosphere. The spatial distribution of the ionosphere is strongly influenced by the Earth's magnetic field. These interrelationships require that the environmental description include several parameters of secondary importance.

Micrometeoroids may penetrate the insulation of the solar array, leading to damaging discharge phenomena. Thus a description of the micrometeoroid impact rate is provided.

High energy ionizing radiation, mainly protons and electrons, degrade the solar cells in the array. These particles are trapped in the Earth's magnetic field and also come from the sun and from the galaxy in the form of cosmic rays. The high voltage solar array, while traversing from 100 nautical miles to synchronous altitude, will go through the dense proton and electron regions of the Van Allen belts. Existing models of this natural radiation environment, developed by NASA and the Air Force and updated by Dr. Vette, are proposed for solar-cell degradation studies.

This environmental model does not include the solar-array and spacecraft environmental components coming from outgassing, ion propulsion thruster operation, and open-tube transmitters.

13.3 DESCRIPTION OF ENVIRONMENT

13.3.1 Earth's Magnetic Field

The Earth's magnetic field, produced by currents in the Earth's core is modulated by mineral deposits in the Earth's crust, currents in the ionosphere, and the motion of the trapped charged particles in the radiation belts. At high altitudes the solar wind compresses the Earth's magnetic field into a cavity termed the magnetosphere. The magnetic field, measured near the surface of the Earth, shows long-time-constant variations of the order of 10^{-7} Tesla (100 gamma) per year, and short time variations associated with solar activity.

Because a large contribution to the Earth's magnetic field is made by fields which originate in the Earth, a dipole or multipole representation of the Earth's magnetic field is useful. A tilted dipole representation of the field gives the

surface field to within 30%, and to within 10% if an off-center dipole is used (Ref. 34). Jensen and Cain have used 1960 data to fit the Earth's magnetic field with a multipole expansion that is about 1.0 percent accurate (Ref. 35). At distances beyond a few Earth radii from the Earth's surface the higher-order terms in the multipole expansion fall off and the dipole becomes the dominant term.

Beyond 6 Earth radii the influence of the solar wind pressure, as well as the trapped particle ring currents, distort the dipole-like field, confining it into the teardrop-like magnetosphere. Here strong variations related to local time and solar activity dominate the magnetic field description. Mead has developed a model which represents the Earth's field at high altitudes (Ref. 36).

13.3.2 Neutral Atmosphere

The neutral atmosphere above 100 nautical miles has a density so low that the atmospheric components separate diffusively. Hence the upper atmosphere is believed to be in diffusive equilibrium. At this height the principle components are molecular and atomic oxygen and molecular nitrogen. The density of each component decreases with increasing height according to the barometric law.

The use of the barometric law requires a knowledge of the scale height for each component, and thus the temperature. Some difficulty has been encountered in obtaining a consistent picture of the upper atmosphere's density and temperature characteristics in the diffuser and above. However, the neutral atmosphere is of secondary importance in the operation of the high-voltage solar array, so the standard atmosphere of 1962 and the 1966 supplement is adequate for this study. (Ref. 37, 38).

13.3.3 Solar Spectrum

The solar electro-magnetic spectrum seen by the Earth's atmosphere ranges from x-rays to radio-frequencies. The infrared, visible, and near ultraviolet radiations have been studied for many years and are well defined. The x-ray and radio emissions, which depend strongly on solar activity, have been studied only recently. A recent compilation of the solar spectrum by Malitson gives a complete description of the solar spectrum with variations during different types of solar activity (Ref. 39).

13.3.4 Auroral and Polar Storm Particles

The auroral zone particles excite the lower ionosphere, enhancing electron densities and temperatures in the topside ionosphere geomagnetically poleward of the F2 trough. The response of the ionosphere is discussed in the next section. The highly variable fluxes of the auroral-zone electrons and protons preclude a simple description of their behavior. However, for considerations of their direct influence upon the spacecraft, peak fluxes and typical spectra will suffice. The spectrum becomes generally harder as we move from the pole toward sub-auroral latitudes (around 60°). The peak auroral fluxes occur in a narrow latitude band centered in the visible auroral zone (above 60 to 69° geomagnetic). The spectra measured in the 65° to 69° zone was adopted for the high-voltage solar array study. Electric fields as intense as 180 mV/m have been observed perpendicular to the magnetic field in the vicinity of bright auroral arcs

13.3.5 Ionosphere

The natural ionosphere is the most significant component of the space environment model; hence, it requires a more comprehensive analysis. The detailed variations of the ionosphere, are the subject of current research, beyond the scope of this effort.

The most important ionosphere parameters for this high-voltage array study are the variations with altitude of the peak electron density and daytime electron and ion temperatures.

In order to describe the structure of the ionosphere it is convenient to list the ionospheric regions where relative maxima of electron density occur. Table 6 presents the nomenclature used in ionospheric literature and typical values of the parameters. Table 7 provides typical values for ionosphere components for sunspot numbers of 0 and 100. The D and E ionosphere regions, described adequately in references 40, 41, and 42, are below the lowest altitude at which the high-voltage array will be attributed (100 nautical miles or 185 km).

13.3.5.1 Sources of Information for Ionospheric Regions

There is no single experiment which measures directly the density, temperatures and the composition of the ionosphere from 185 km to synchronous altitude. Furthermore there is not yet available a complete theory of the ionosphere for extrapolating reliably the results of experiments to spatial and temporal regions not probed. Thus our best sources of information on the ionosphere are those experiments which are giving the broadest coverage. The altitude regions explored by the major experiments are:

<u>Altitude</u>	<u>Experimental Technique</u>
185 km - F_2 peak	Ionosondes, rockets
F_2 peak - 1000 km	Topside ionosondes, satellites, rockets
185 km - 6000 km	Incoherent scatter
$2 R_e - 6 R_e$	VLF and ULF whistlers
$2 R_e - 7 R_e$	Plasma Probes

All of these experiments can yield the electron density directly.

An excellent detailed description of the use of radio waves to measure the refractive, reflective and transmissive properties of the ionosphere is given by Rawer and Suchy (Ref. 43). They also present an excellent summary of the information obtained from the ionosonde data prior to the satellite era. Examples of their data appear in Figures 30 through 31.

Just as ground-based ionosondes provide density in the bottomside ionosphere, the satellite-based topside ionosondes are the workhorse of electron density determinations in the topside ionosphere. While the topside ionosondes provide

TABLE 6: NOMENCLATURE USED IN IONOSPHERE LITERATURE

f_o	= ordinary critical frequency
f_x	= extra-ordinary critical frequency
f_H	= gyro-frequency for a magnetic flux density B (commonly B = H)
V_{ei}	= collision frequency of electrons with ions
V_{en}	= collision frequency of electrons with neutrals
V_{in}	= collision frequency of ions with neutrals
N_e	= electron concentration
N_i	= ion concentration
N_{max}	= maximum electron concentration in an ionospheric layer
N_{max}	= $(\pi m/e^2) f_o^2 = 1.2404 \times 10^4 f_o^2 \text{ cm}^{-3}$ (f_o in MHz)
	= $(\pi m/e^2) (f_x^2 - f_x f_H) = 1.204 \times 10^4 (f_x^2 - f_x f_H)$ (f_x f_H in MHz)
f_H	= $(e/2\pi mC) B = 2.7994 B \text{ MHz}$
α	= recombination coefficient (rate = $\alpha N_e N_i = \alpha N_e^2$)
β	= attachment-like coefficient (rate = βN_e)
q	= ionization rate
	simple theory $dN_e = q - \alpha N_e^2 - \beta N_e$
R	= sunspot number
h	= altitude
h'	= virtual height
D_a	= ambipolar diffusion coefficient
T_n	= temperature of neutral atoms
T_e	= temperature of electrons
T_i	= temperature of ions
R_e	= radius of Earth

TABLE 7: REPRESENTATIVE VALUES OF IONOSPHERE PARAMETERS

Quantity	Unit	IONOSPHERE					
		<u>D</u>	<u>E</u>	<u>F₁</u>	<u>F₂</u>	<u>Topside</u>	<u>Plasmosphere</u>
Layer height	km	80	115	170	300	300-1000	10^3 - 4×10^4
Neutral density	cm^{-3}	10^{15}	10^{12}	2×10^{10}	10^9	10^9 - 10^6	10^6 - 10^1
Behavior	--	Regular	Simple Theory		Diffusion	Geomagnetic Control	Geomagnetic Activity Control
Noon N_{max} (R=0)	MHz	600	1.4×10^5	2.4×10^5	6×10^5	6×10^5 - 2×10^4	2×10^4 - 1×10^2
(R=100)	MHz		1.9×10^5	3.6×10^5	2×10^6	2×10^6 - 6×10^4	6×10^4 - 1×10^{-1}
q (R=0)	$\text{cm}^{-3} \text{sec}^{-1}$		500	700	100	< 100	--
(R=100)	$\text{cm}^{-3} \text{sec}^{-1}$		1000	1500	300	< 300	--
$\alpha N_{\text{max}} + \beta$ (R=0)	sec^{-1}	$> 10^{-3}$	4×10^{-3}	3×10^{-3}	10^{-4}	10^{-4} - 10^{-7}	--
$\alpha N_{\text{max}} + \beta$ (R=100)	sec^{-1}	$> 10^{-3}$	4.5×10^{-3}	3.9×10^{-3}	4×10^{-4}	4×10^{-4} - 10^{-7}	--
V_{ei}	sec^{-1}	--	10^3	10^3	10^3	10^3 -30	10 - 10^{-3}
V_{en}	sec^{-1}	10^7	3×10^4	1.2×10^3	12	10 - 10^{-8}	
Da (R=0)	cm sec^{-1}				3×10^{-10}		
Da (R=100)	cm sec^{-1}				2×10^{-10}		
Noon T_n (R=0)	K°	180	350	600	850	900	900
Noon T_n (R=100)	K°	180	350	1000	1400	1400	1400
Noon T_e (R=0)	K°			600	2600	3000	3000 - 10^4
Noon T_e (R=100)	K°			1000	3000	3500	3500 - 5×10^4
Noon T_i (R=0)	K°			600	1000	1 - 3×10^3	3×10^3 - 10^4
Noon T_i (R=100)	K°			1000	1500	2 - 3.5×10^3	3.5×10^3 - 5×10^4

D2-121734-1

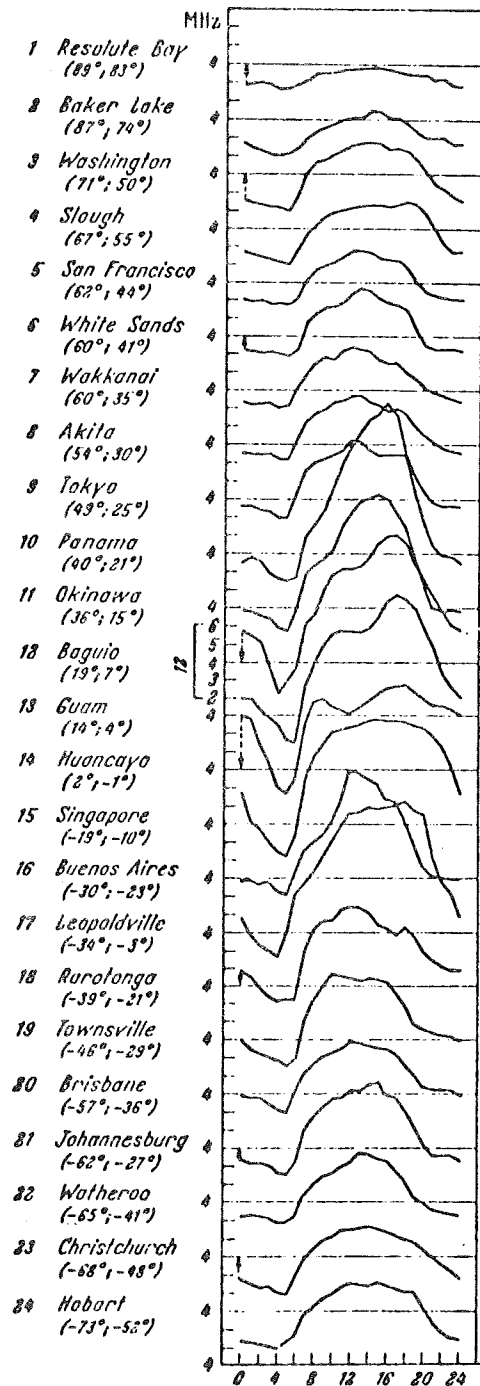


Figure 30: MEAN DIURNAL VARIATION OF f_oF_2 FOR EQUINOX MONTHS
(Magnetic Inclination I and Geomagnetic Latitude λ in Brackets)

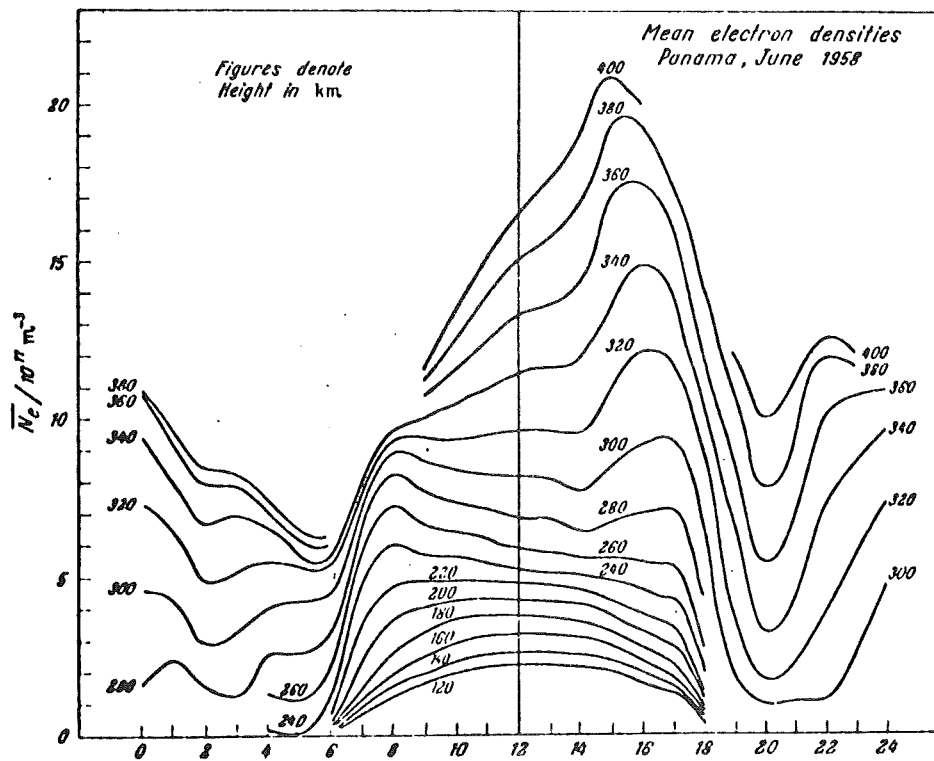
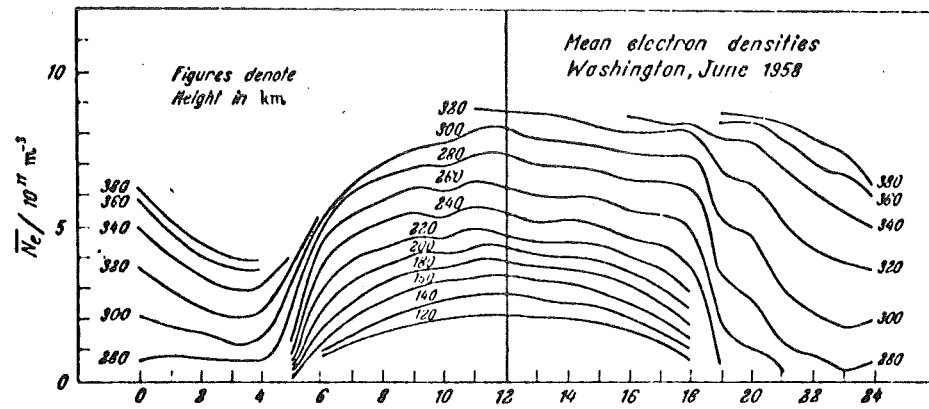
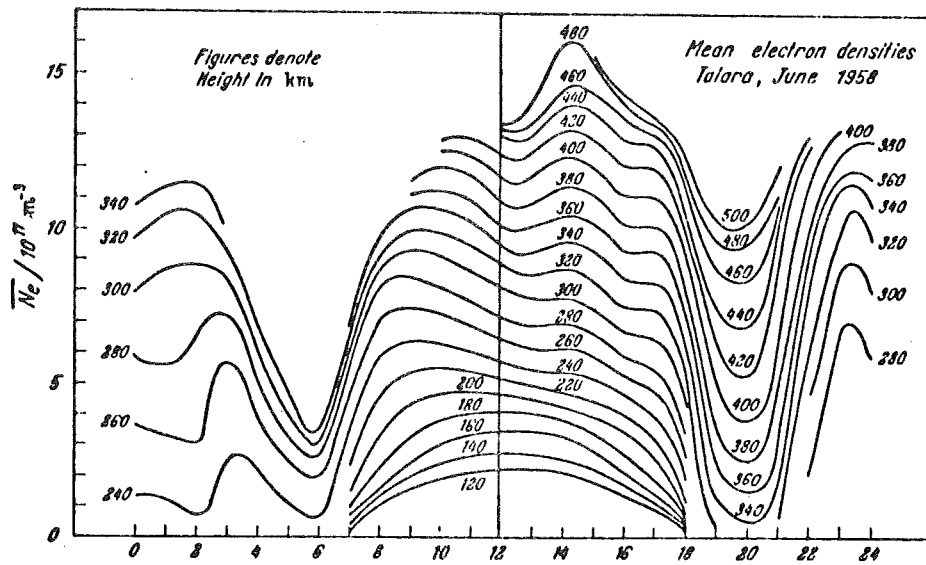
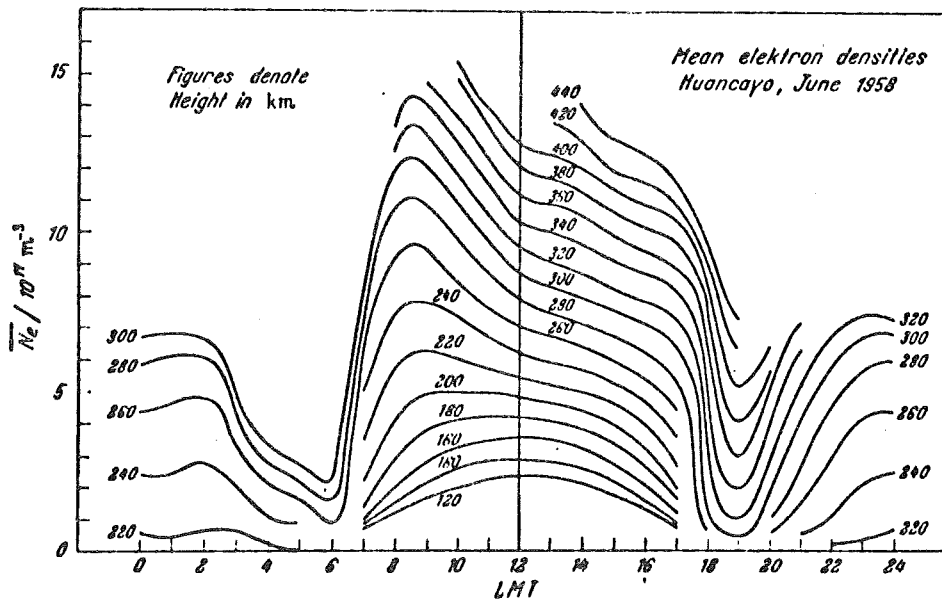


Figure 31: DIURNAL VARIATION OF THE MEAN ELECTRON DENSITY (June 1958)

(Reference 43)



c) Talara, I = 13°



d) Huancayo, I = 2°

Figure 31: DIURNAL VARIATION OF THE MEAN ELECTRON DENSITY (June 1958)

rapid geographic coverage, the ground-based ionosondes produce local time dependence at many selected sites. Typical topside ionosonde data appear in Figures 32 through 34. A world map of $f_o f_2$ is shown in Figure 35.

The overlap provided by the increasing number of incoherent Thomson scatter results for the bottomside and topside ionosphere have facilitated greatly the separation of geomagnetic and local time dependences. Improved world maps and profiles are being compiled by Environmental Science Services Administration (ESSA) and are available through the World Data Center (WDC). The usefulness of Thomson scatter in obtaining directly density, electron temperature, and electron/ion temperature-ratio profiles was recently reviewed by Evans (Ref. 44). He also shows how to determine composition and magnetic field directions, and describes techniques for improving the spatial and temporal resolution of the measurements.

The understanding of the F region and topside ionosphere increased substantially since 1960. Chapman's review, the session summaries, and the concluding remarks by Evans, Bauer and Chapman given at the NATO Advanced Study Institute in April 1965 are particularly useful (Ref. 45). Geomagnetic control was then well established and the importance of drift (Ref. 46,47), photoelectrons (Ref. 48,49), and geomagnetic tail currents (Ref. 50) was strongly suggested.

The plasmasphere has been examined with VLF whistler-propagation techniques and the results have been compared with data from plasma probes on eccentric Earth-orbiting satellites (Ref. 51,52,53). Recently the analysis of ULF (about 1.0 Hz) whistlers (Ref. 54,55) has provided plasma densities out to 8 Earth radii.

The best theoretical description of the plasmasphere is perhaps given in Angerami's thesis (Ref. 56). As is pointed out by Kenney et al (Ref. 55) the quiet-time plasmasphere extends beyond synchronous altitude and the densities are highest during the sun's quiet times. The ULF whistlers are important in that they are observed more frequently at quiet times, while the VLF whistlers occur most frequently during disturbed conditions.

Probes on ATS satellites at synchronous altitude have shown that (i) extra-plasmaspheric plasma at synchronous altitude is characterized by directed flow (normally toward the magnetosphere boundary) and (ii) during moderate storms, the magnetosheath plasmas appear at synchronous altitude (Ref. 57). Thus the penetration of the bow shock and admission of the solar wind to synchronous altitude during a large storm is possible.

13.3.5.2 Altitude Dependence of Ionosphere Parameters

The electron density increases up to the F2 peak and then decreases monotonically to the edge of the plasmasphere in the non-polar ionosphere and into the geomagnetic tail in the polar ionosphere. The decoupling of the polar ionosphere in the vicinity of the auroral zone is already apparent at 1000 km altitude. Above the F2 peak the sub-auroral altitude dependence is characterized by diffusive equilibrium in the geomagnetic field, while the polar ionosphere has flow to and from the tail. The envelope of all altitude profiles is the model for our study. Thus as we rise upward, this envelope represents the peak densities under a variety of conditions, transferring from solar control at the subsolar point to geomagnetic control at about 15° latitude near the F2 peak, and then

(Reference 45)

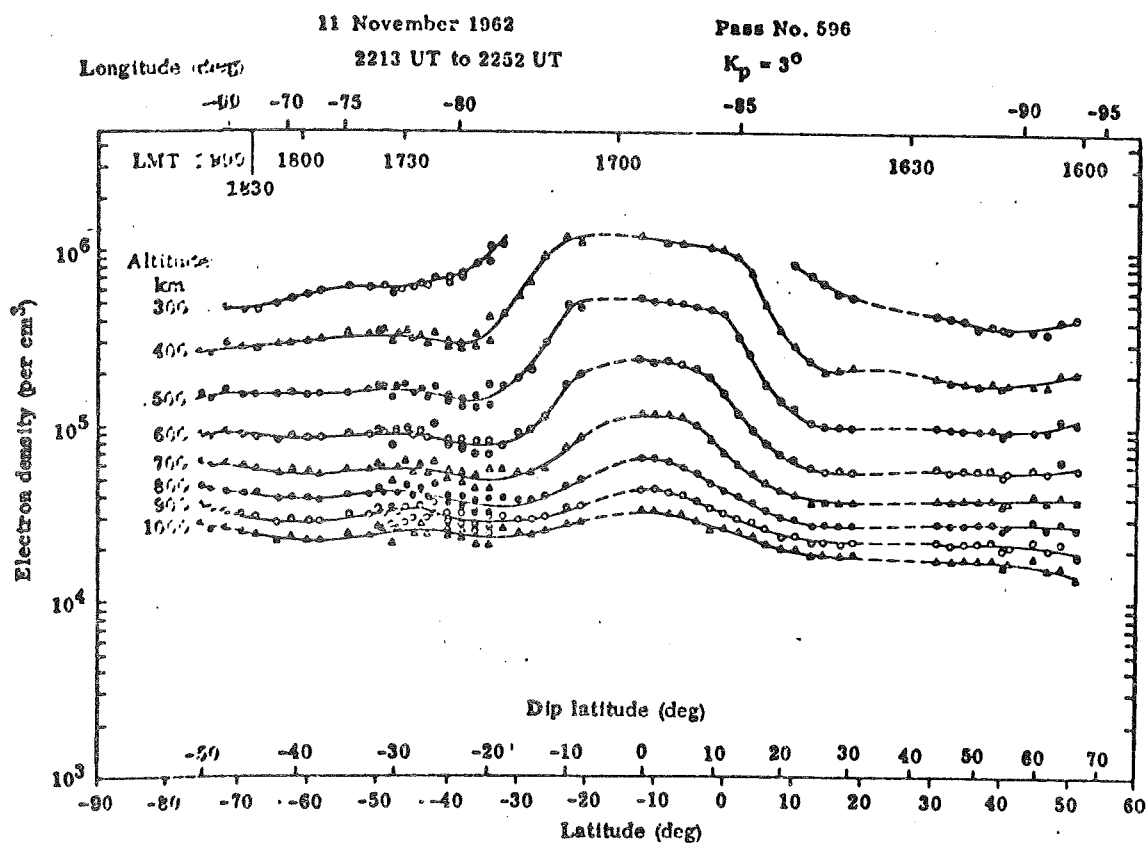


Figure 32 : LATITUDINAL VARIATIONS OF ELECTRON DENSITY IN THE TOPSIDE IONOSPHERE (11 November 1962)

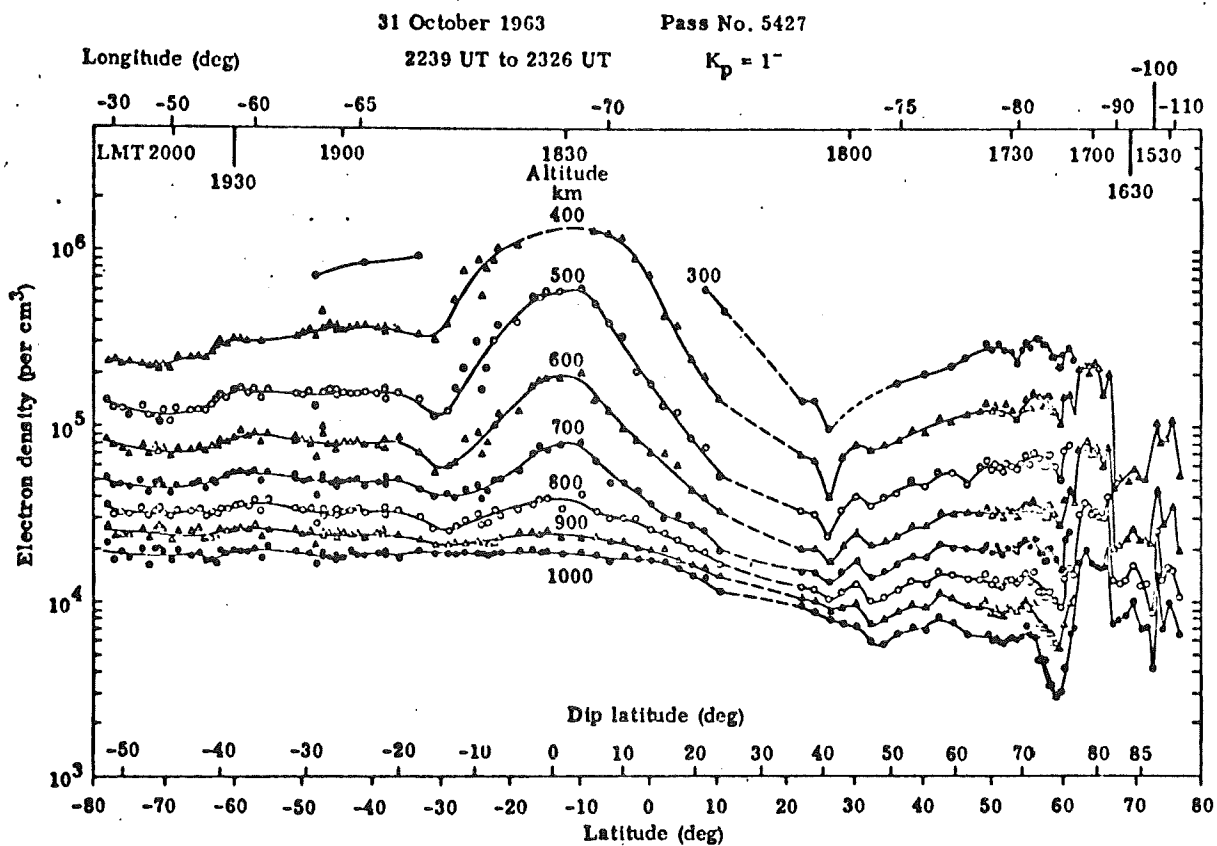
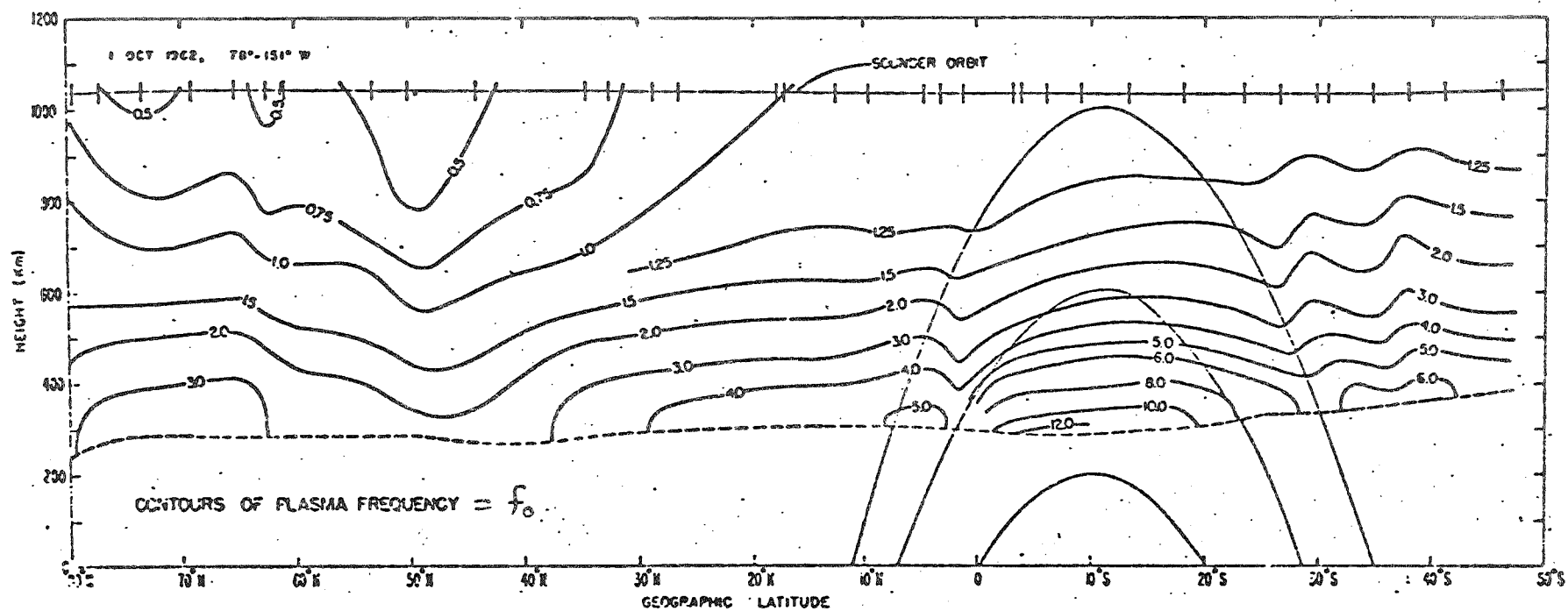


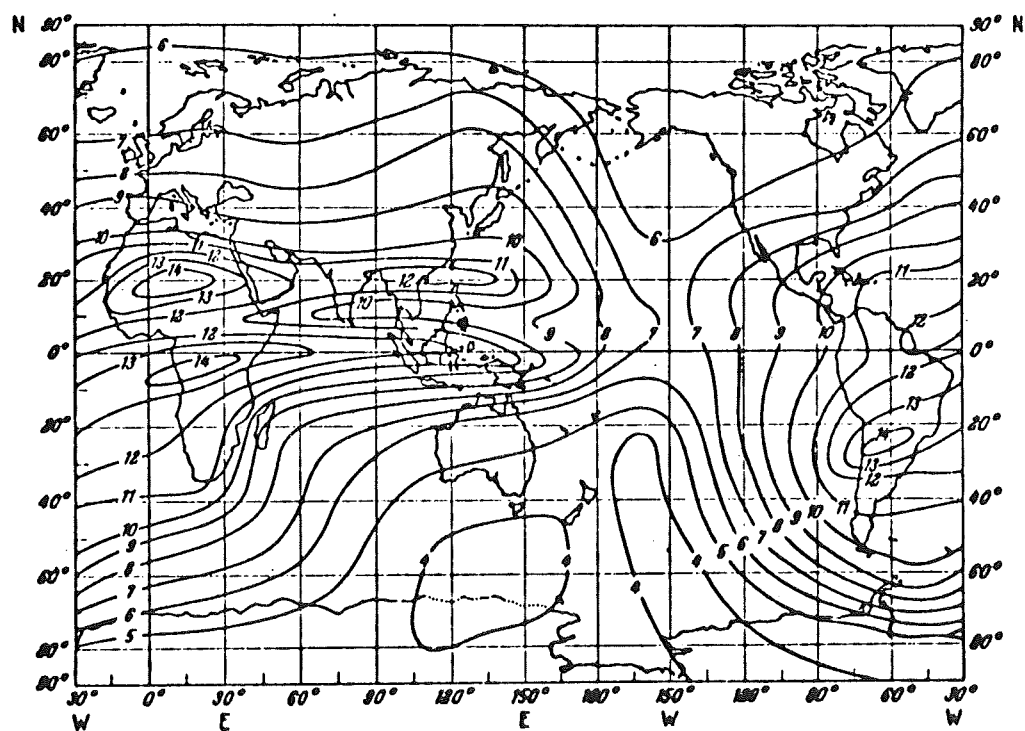
Figure 33: LATITUDINAL VARIATIONS OF TOPSIDE ELECTRON DENSITY
 (31 October 1963)

(Reference 45)



D2-121734-1

Figure 34: TYPICAL TOPSIDE SOUNDER DATA
 (Note: $N_e = 1.2404 \times 10^4 f_o^2 \text{ cm}^{-3}$)

Figure 35: WORLD MAP OF f_oF_2 FOR 15 UT

to the geomagnetic equator above 600 km altitude (Fig. 36).

The electron and ion temperatures generally rise slowly with altitude, and the latitude and local time dependencies are strong. Mid-latitude temperature profiles on December 18, 1964 illustrate the time and altitude dependency (Fig. 37).

The composition of the ionosphere is principally O^+ below the F_2 peak. The O^+ concentration decreases monotonically with altitude. The H^+ and He^+ concentration increases at all latitudes, peaking above the F_2 layer and then decreasing monotonically. A typical composition profile (Ref. 58) is presented in Figure 38. Local time dependence of the composition is shown in Figure 39. The altitude where H^+ becomes the major ion is strongly dependent upon latitude and local time. A profile for the polar ionosphere (Ref. 59) is presented in Figure 40.

13.3.5.3 Seasonal and Diurnal Variations

The strongest electron and ion density changes are the diurnal variations. An example of Equatorial ionosphere changes is provided in Figure 41. An example of mid-latitude density appears in Figure 42. A map of f_oF_2 seasonal and long term variation during a period of decreasing solar activity in Solar cycle 18 (1944-1954), originally presented by Rawer and Suchy, is shown in Figure 43. The monthly mean density N_e at the F_2 peak is given by $1.2404 \times 10^4 f_o^2 \text{ cm}^{-3}$. Thus, the monthly mean at 23.5° dip latitude exceeded $3.6 \times 10^6 \text{ cm}^{-3}$ from 1100 to 1600 hours in the fall of 1949. The solar cycle variation is strongest at the higher latitudes, as can be seen by comparing Figures 43b and 43d. Figure 43c shows the seasonal variation of the diurnal maximum.

The electron temperature exceeds the ion temperature immediately after sunrise and remains higher throughout the day in altitudes over 800 km. Typical profiles of mean daytime temperatures are presented in Figures 44a through 44f.

The temporal changes of the composition are generally small. In the excited warm ionosphere at O^+ ion concentration is enhanced while the H^+ concentration is enhanced at night and during periods of low solar activity.

13.3.5.4 Geomagnetic Latitude Dependence

The geomagnetic latitude competes with the local time for F_2 layer control. Figure 35 shows a typical contour plot of $\log n_{\max}$ for March 1958, a period near the peak of Cycle 19, when $R = 210$. Above the F_2 peak the density generally decreases with latitude, reaching a minimum at about 60° latitude and increasing slightly in the polar regions. Figure 45 shows typical latitude profiles at around 800 km, demonstrating that averaging over time will wash out the minimum so-called F_2 "trough".

The ionosphere temperature depends strongly upon latitude. Figure 46 presents for 800 km a simple model which is consistent with topside sounder data. The highest temperatures are observed in the auroral zone. Recently electron temperatures as high as 6000°K have been deduced from probe measurements at 1000 km in an auroral storm (Ref. 60).

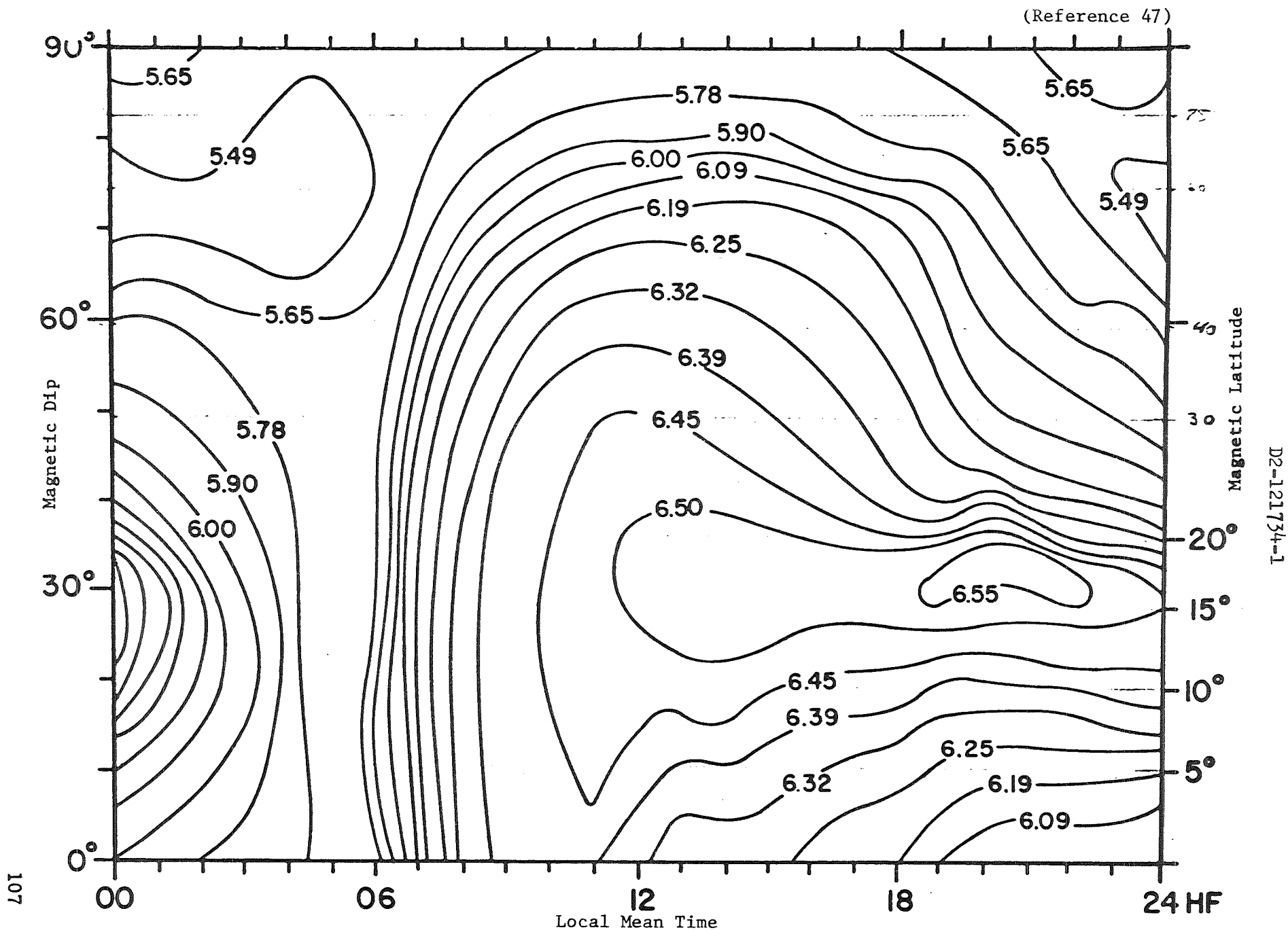


Figure 36: $\text{LOG } N_{\text{MAX}}$ VS MAGNETIC DIP ANGLE, I, AND LOCAL MEAN TIME
(March 1958)

(Reference 45)

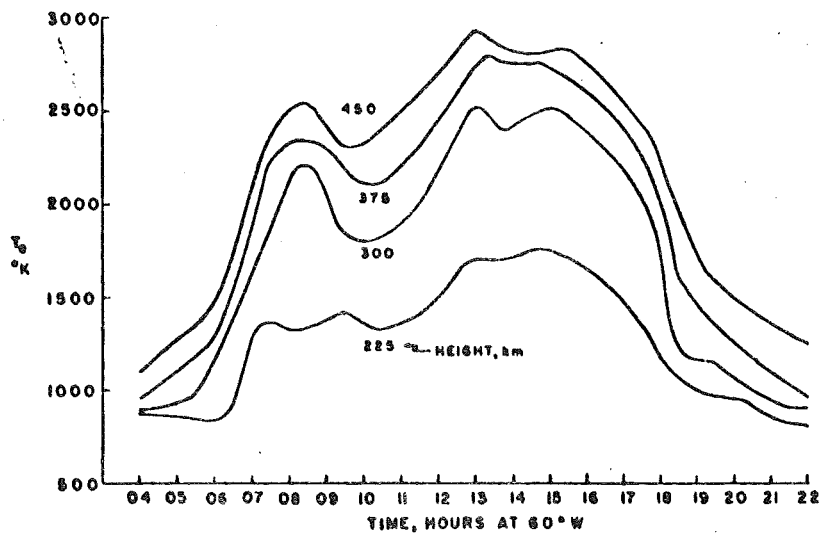


Figure 37: ELECTRON TEMPERATURES OBSERVED ON DECEMBER 18, 1964

(Reference 58)

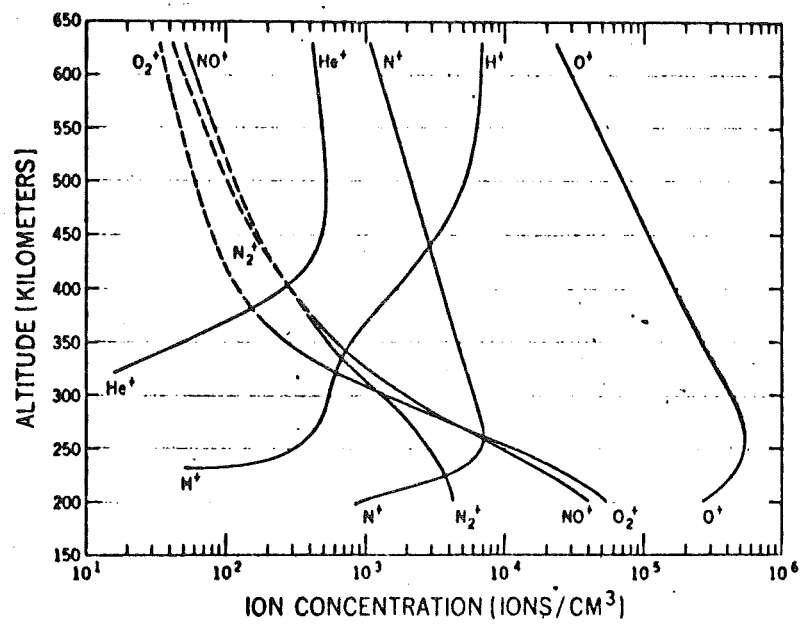


Figure 38: ALTITUDE PROFILES OF INDIVIDUAL ION CONCENTRATIONS

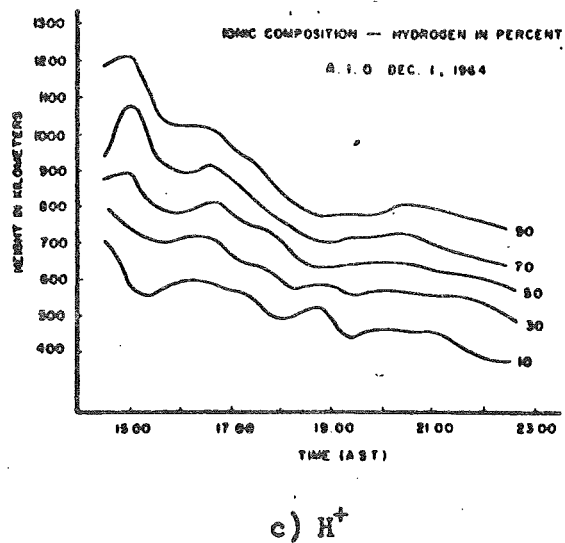
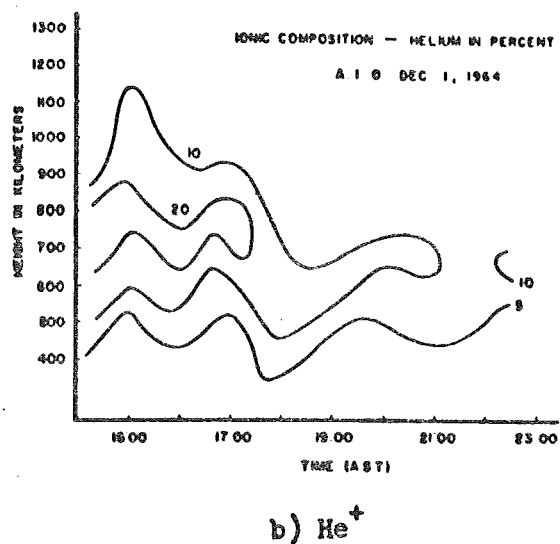
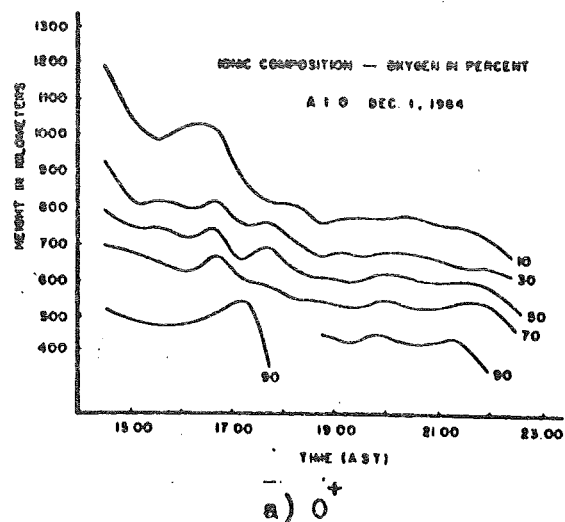


Figure : IONIC COMPOSITION IN THE LATE AFTERNOON AT MIDLATITUDES

(Reference 59)

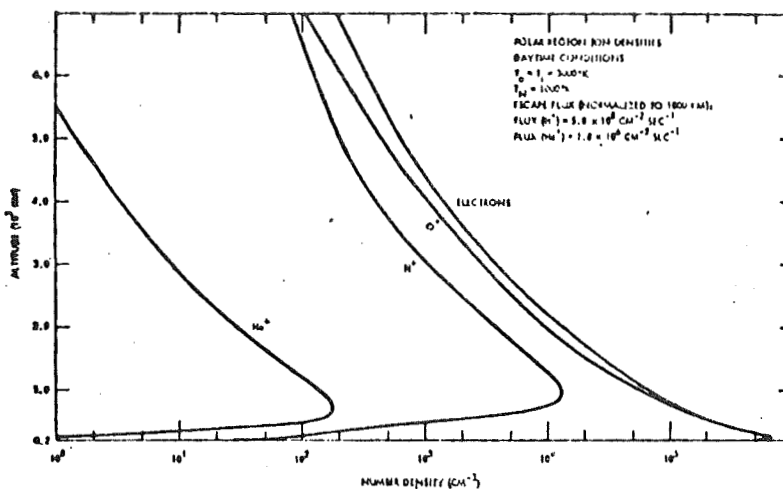


Figure 40: ION COMPOSITION MODEL OF THE POLAR IONOSPHERE

(Reference 45)

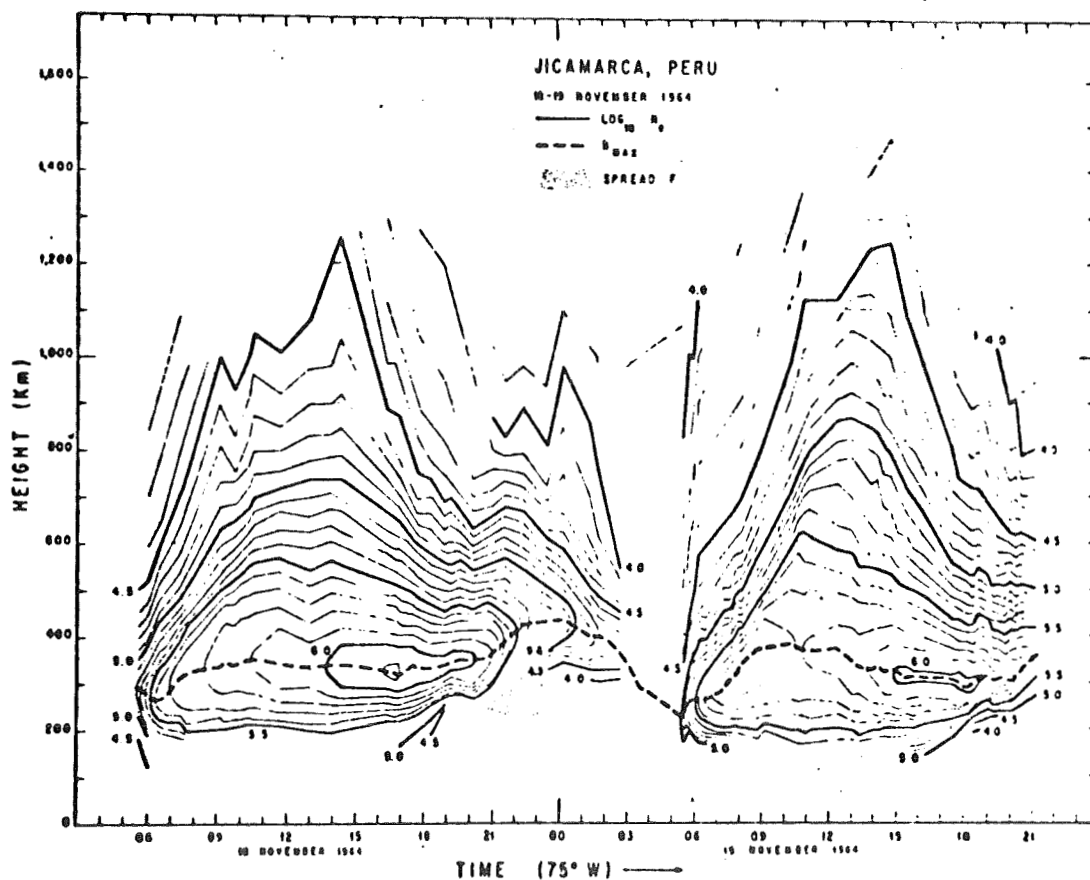


Figure 41: CONTOURS OF ELECTRON DENSITY NEAR THE EQUATOR

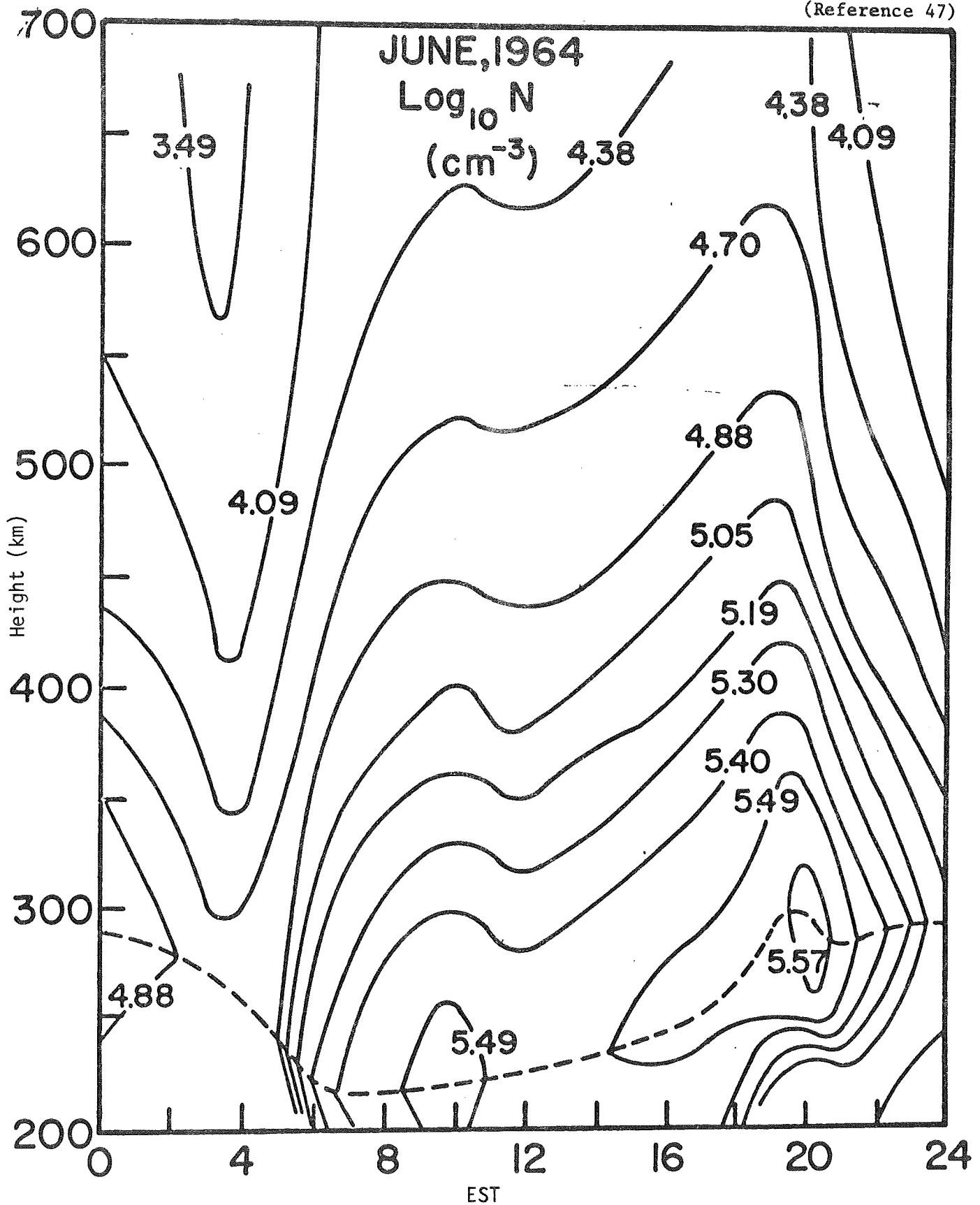
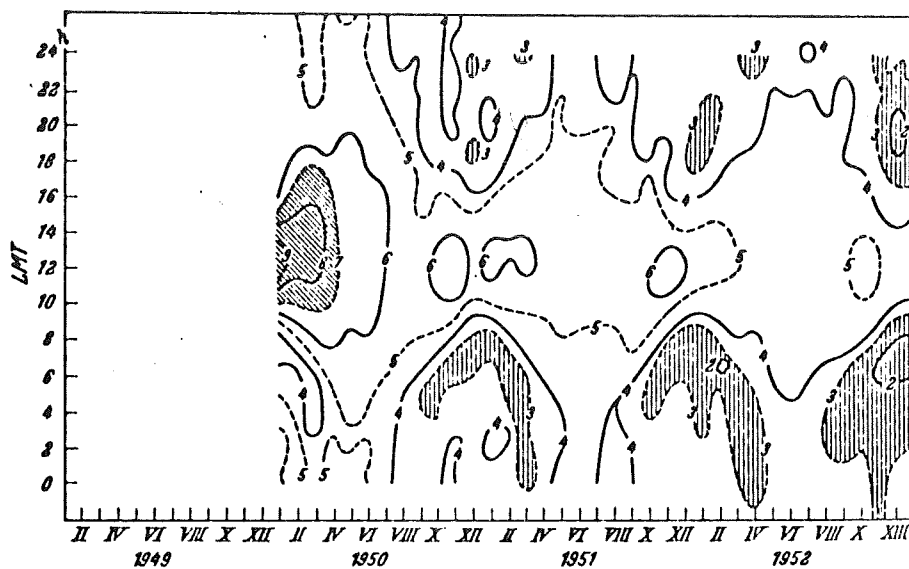
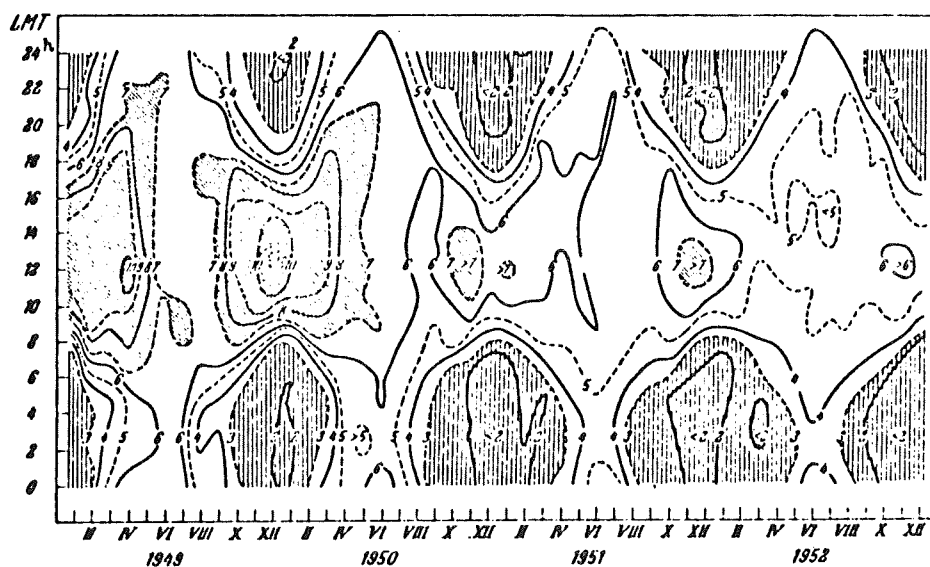


Figure 42: CONTOURS OF ELECTRON DENSITY OVER MILESTONE, MASS



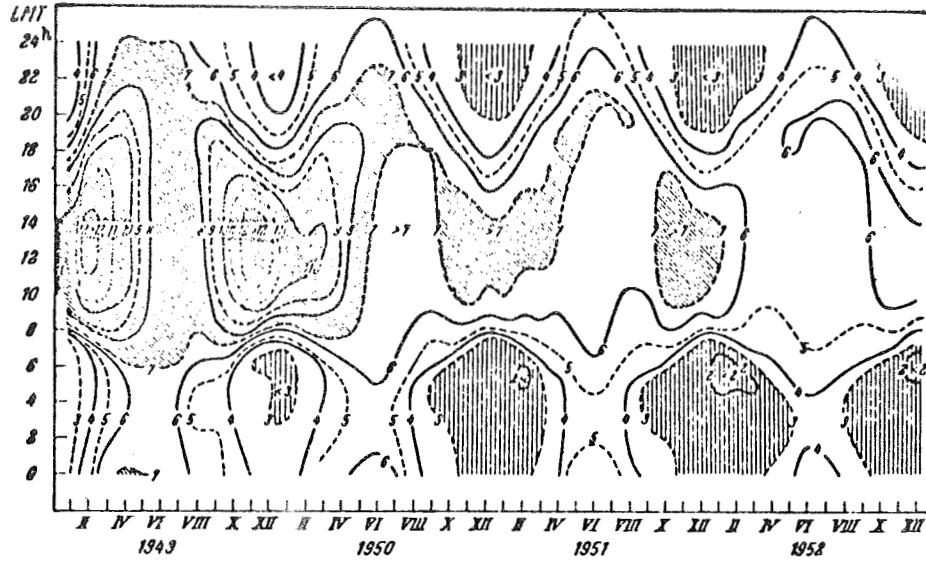
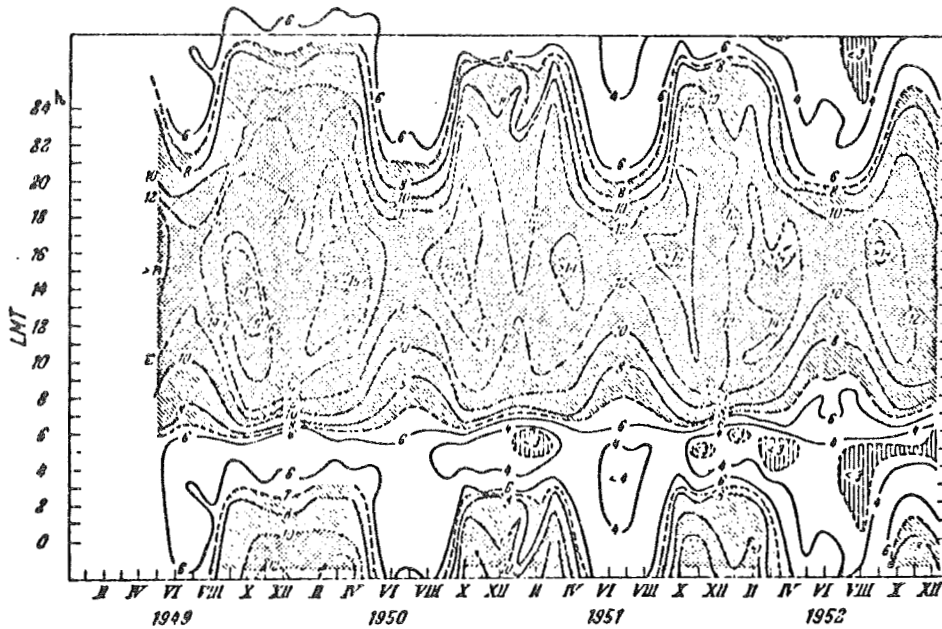
a) Reykjavik, $I = 76^\circ$



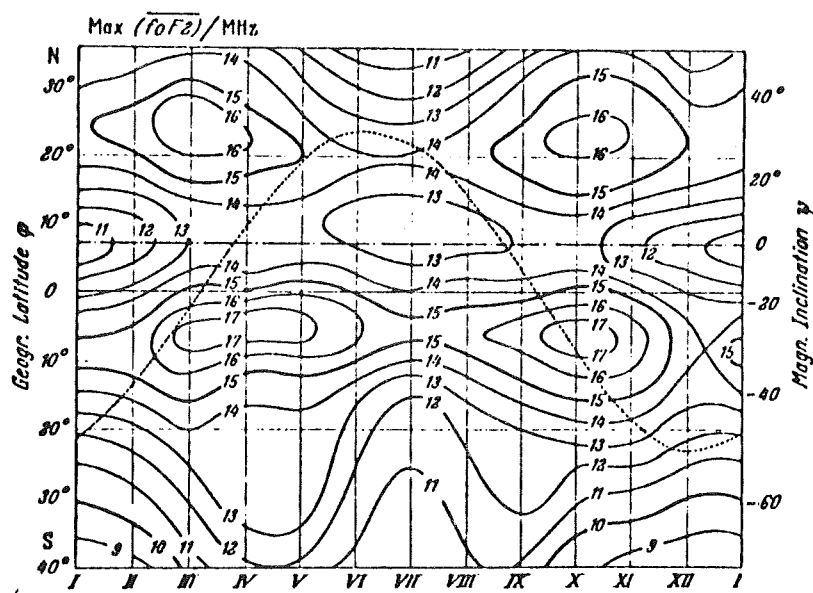
b) Oslo, $I = 72^\circ$

Figure 43: SEASONAL AND LONGTERM VARIATION OF f_oF_2 DURING A PERIOD OF DECREASING SOLAR ACTIVITY

(Reference 43)

c) Slough, $I = 67^\circ$ d) Dakar, $I = 23.5^\circ$ Figure 43: SEASONAL AND LONGTERM VARIATION OF f_oF_2 DURING A PERIOD OF DECREASING SOLAR ACTIVITY

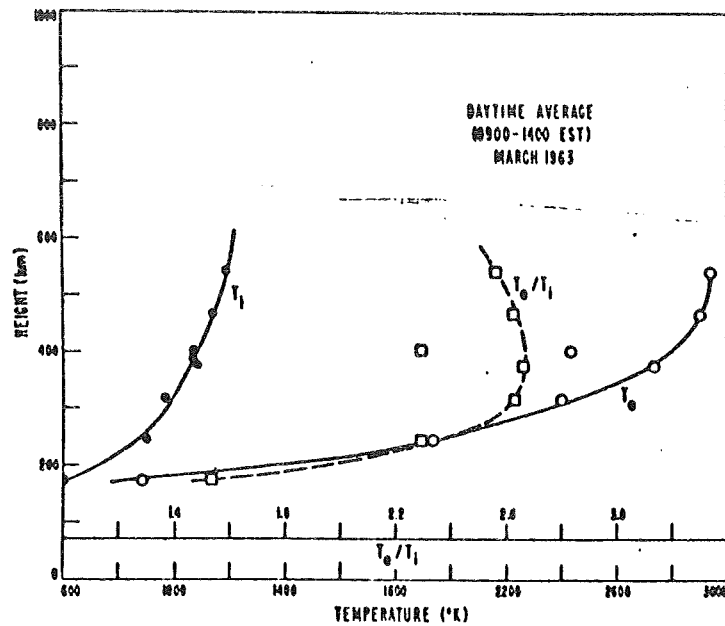
(Reference 43)



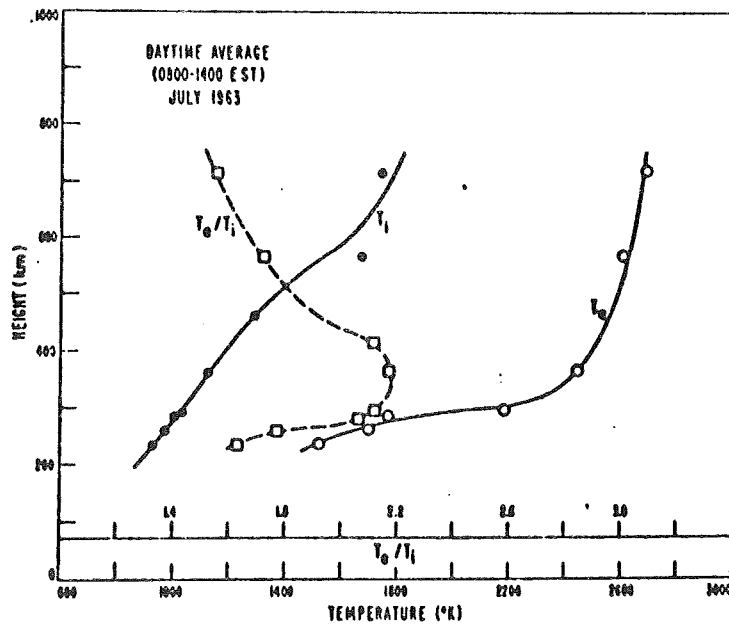
e) Dotted Line is the Subsolar Point at Noon

Figure 43: DIURNAL MAXIMUM OF f_oF_2 AS A FUNCTION OF LATITUDE AND SEASON (FAR EAST STATIONS)

(Reference 45)

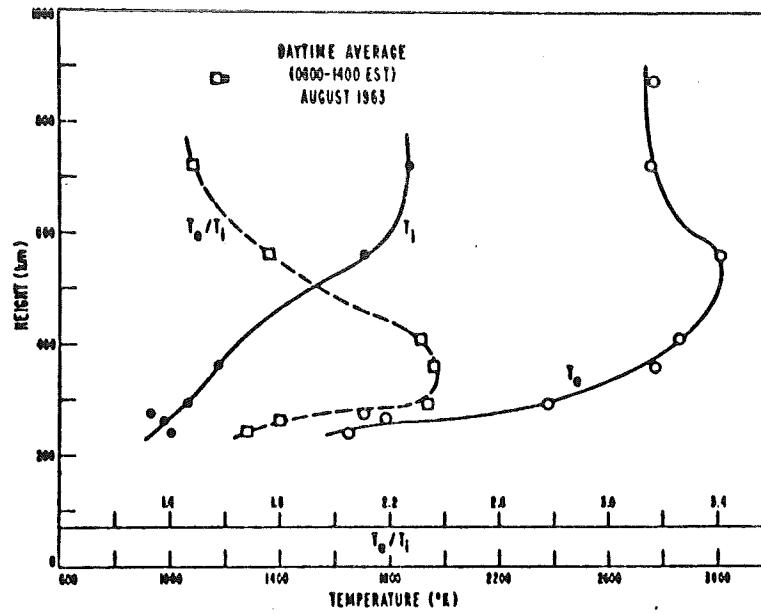


a) March, 1963

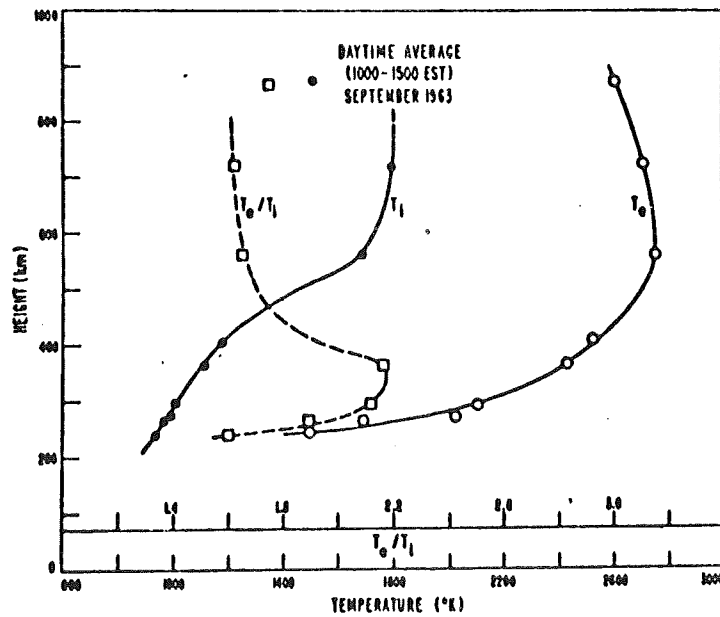


b) July, 1963

Figure 44: VARIATION OF T_i , T_e , AND T_e/T_i WITH HEIGHT DURING THE DAYTIME



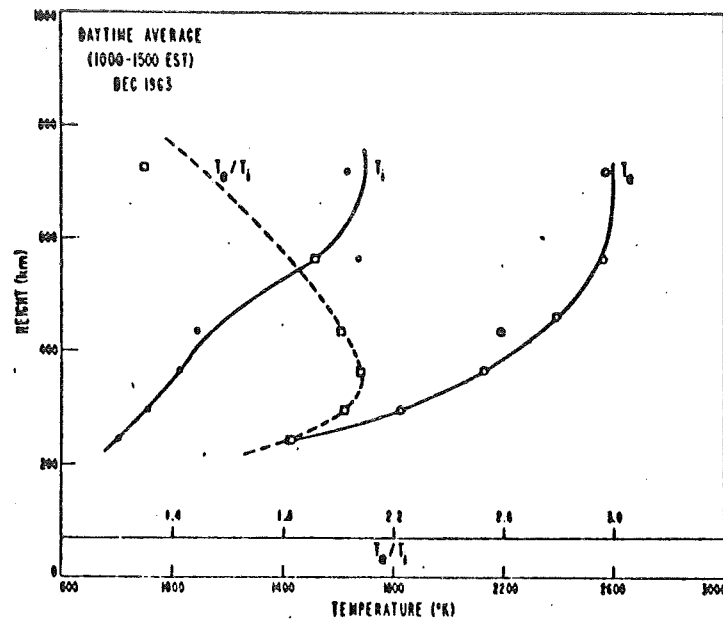
c) August, 1963



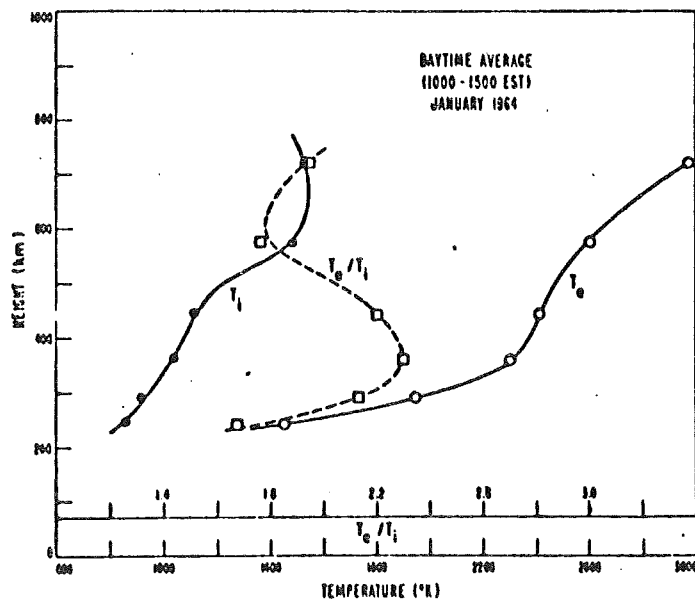
d) September, 1963

Figure 44: VARIATION OF T_i , T_e , AND T_e/T_i WITH HEIGHT DURING THE DAYTIME (CONT)

(Reference 45)



e) December, 1963



f) January, 1964

Figure 44: VARIATION OF T_i , T_e , AND T_e/T_i WITH HEIGHT DURING THE DAYTIME (CONT)

(Reference 45)

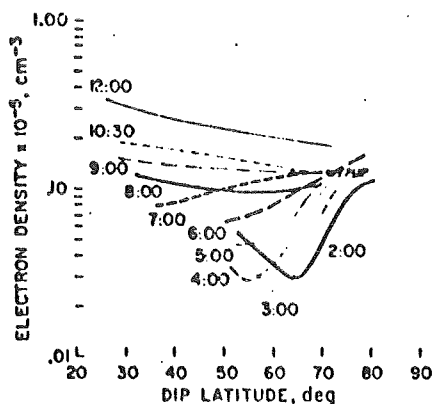


Figure 45: AVERAGE LATITUDINAL VARIATION OF THE ELECTRON DENSITY AT THE ALOUETTE I ORBIT, SUMMER OF 1963

(Reference 45)

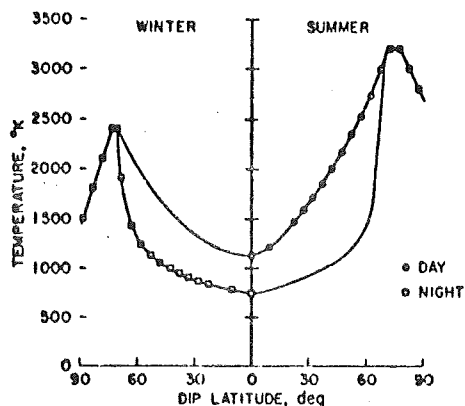


Figure 46: MODEL LATITUDINAL VARIATION OF THE EFFECTIVE TEMPERATURE OF THE IONOSPHERE PLASMA ABOVE 800 KM

(Reference 45)

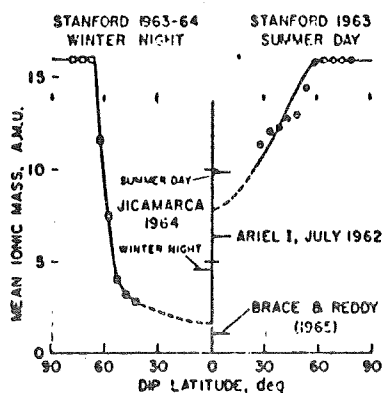


Figure 47: LATITUDINAL VARIATION OF MEAN IONIC MASS AT AN ALTITUDE OF 800 KM

The ionic composition is under strong geomagnetic control. Figure 47 gives the mean mass at about 800 km. Figures 48 through 50 give at 1000 km typical ion concentrations versus latitude in the dawn and dusk meridians. As mentioned previously the high altitude polar ionosphere is predominately H⁺.

13.3.5.5 Plasmasphere

Ambipolar diffusion controls densities within the plasmasphere and its extent is controlled by geomagnetic activity. Figure 51 shows the typical dependence of the boundary upon the planetary index K_p . Typical equatorial density profiles for quiet times are presented in Figure 52. The hydromagnetic emissions that generate ULF whistlers may represent a plasma instability and thus the envelope of these data will represent peak densities.

During disturbed times the energetic flow of plasma observed by Freeman (Ref. 57) can be expected. Figure 53 presents an example of the directional flux of thermal H⁺ ions near synchronous altitude. The extreme condition of directed flux at synchronous altitude would be that observed in the solar wind.

13.3.6 Magnetosphere

The influence of the Earth's magnetic field is confined by the pressure of the solar wind to a region about the Earth termed the magnetosphere. Although the high-voltage solar array will normally remain within the magnetosphere, occasionally solar activity will increase the velocity of the solar wind and compress the magnetosphere on the sunward side to the extent that a synchronous-altitude spacecraft will penetrate the boundary of the magnetosphere. The solar array may then be exposed to the extra-magnetospheric environment, as well as to the transition region at the edge of the magnetosphere.

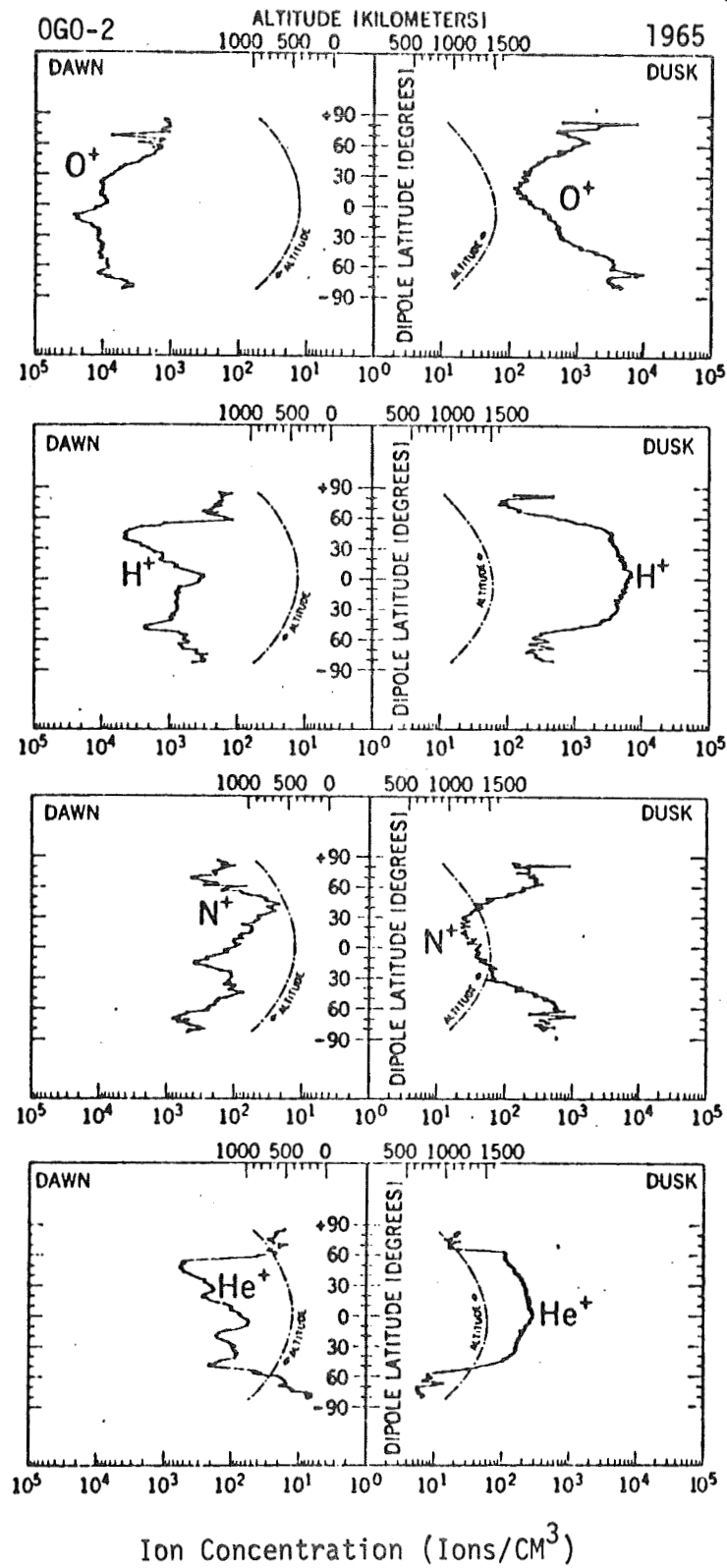
The solar wind, emitted by the sun's corona, is an ionized plasma of hydrogen and helium which streams past the Earth with a bulk velocity of 300 to 500 km/sec. Embedded in this plasma is the interplanetary magnetic field, which near the Earth has a field strength of about 5 γ (5×10^{-9} Tesla). The solar wind bulk velocity with respect to the Earth is nearly eight times the speed of sound in the plasma, so a bow shock forms at about 14 earth radii and trails around the Earth in a teardrop shape. Inside the bow shock we encounter the turbulent magnetosheath, a region of disordered magnetic fields and irregular fluxes of protons and electrons. At about 10 Earth radii in the direction of the sun we encounter the magnetopause, a thin boundary between the magnetosheath and magnetosphere.

Inside the magnetopause, which trails behind the Earth in the anti-solar direction forming the magnetic tail, the Earth's magnetic field is a dominant influence in ordering charged particle motions. As we approach the Earth, the strength of the magnetic field increases until it is well represented by the stable modified dipole representation of Mead, and then by the model of Jenson and Cain.

13.3.6.1 Solar Wind and Storm Variations

An excellent review of the state of knowledge of the solar wind was written in 1966 by Dressler (Ref. 61). The plasma experiments on the Pioneer, Vela, IMP and

(Reference 50)

Figure 48: CONCENTRATIONS OF H⁺, O⁺, N⁺, AND He⁺ AS A FUNCTION OF DIPOLE LATITUDE

(Reference 50)

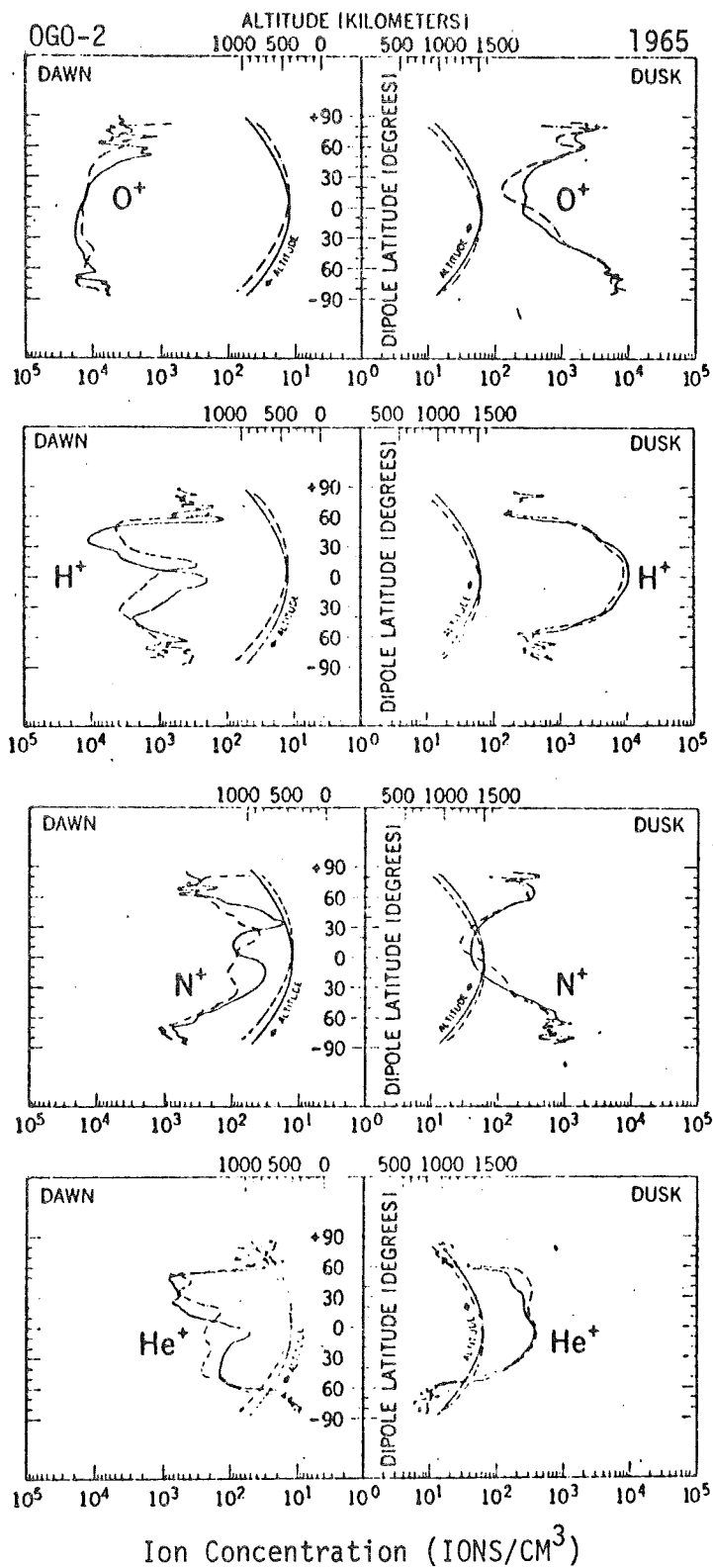


Figure 49: CONCENTRATIONS OF H⁺, O⁺, N⁺, AND He⁺ FOR TWO ORBITS ON OCTOBER 14-15, 1965

(Reference 50)

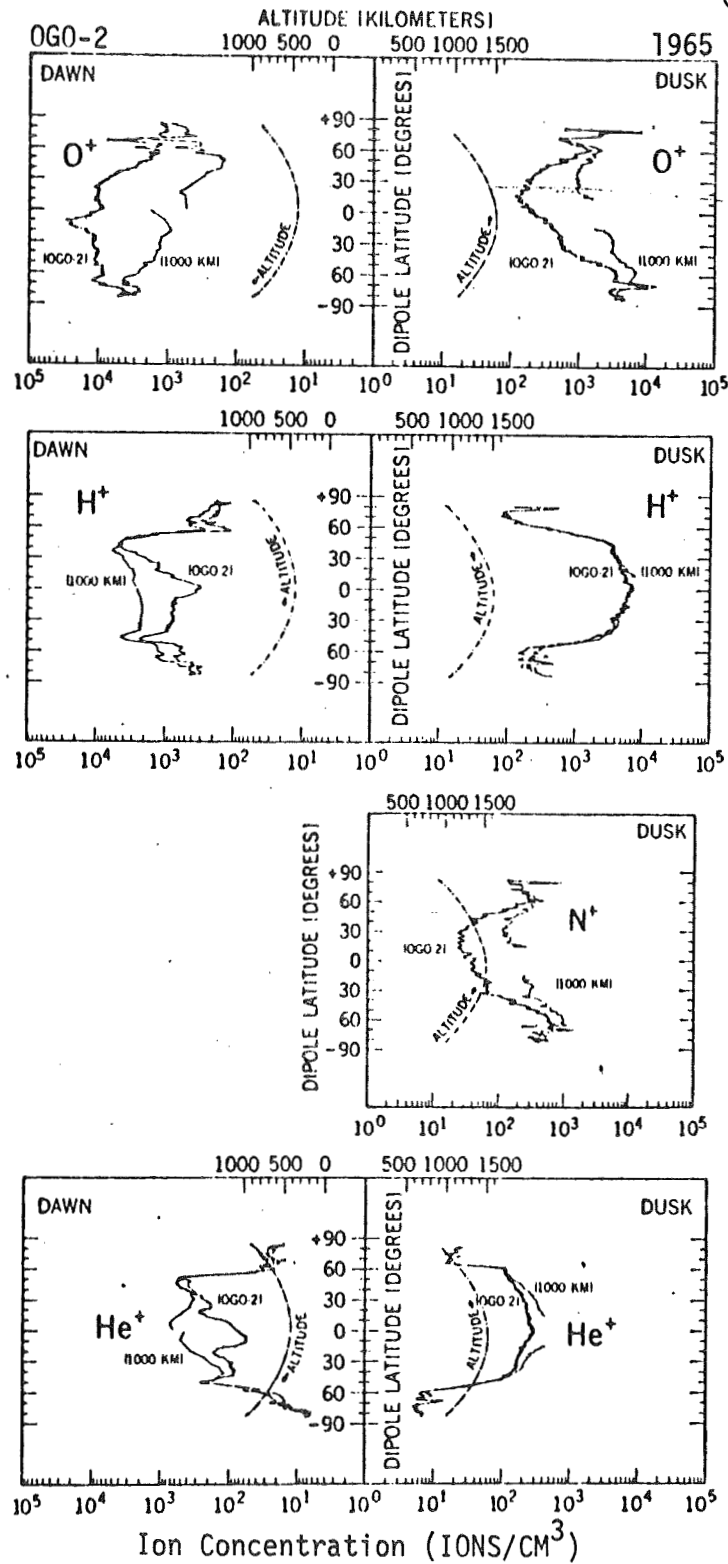


Figure 50: COMPARISON OF DISTRIBUTIONS OF O⁺, H⁺, N⁺, AND He⁺ OBSERVED AT VARIOUS ALTITUDES WITH THE EXTRAPOLATION OF THESE DATA TO A CONSTANT 1,000-KILOMETER LEVEL (SOLID CURVES). FIELD-ALIGNED CHEMICAL AND DIFFUSIVE EQUILIBRIUM ASSUMED.

(Reference 45)

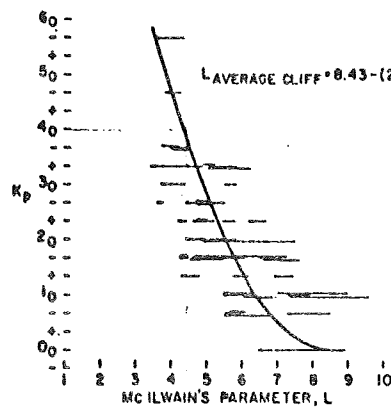


Figure 51: REGRESSION OF THE SHELL PARAMETER OF THE CLIFF IN ELECTRON DENSITY WITH PLANETARY INDEX K_p FOR LOCAL NIGHT DURING THE SUMMER OF 1963

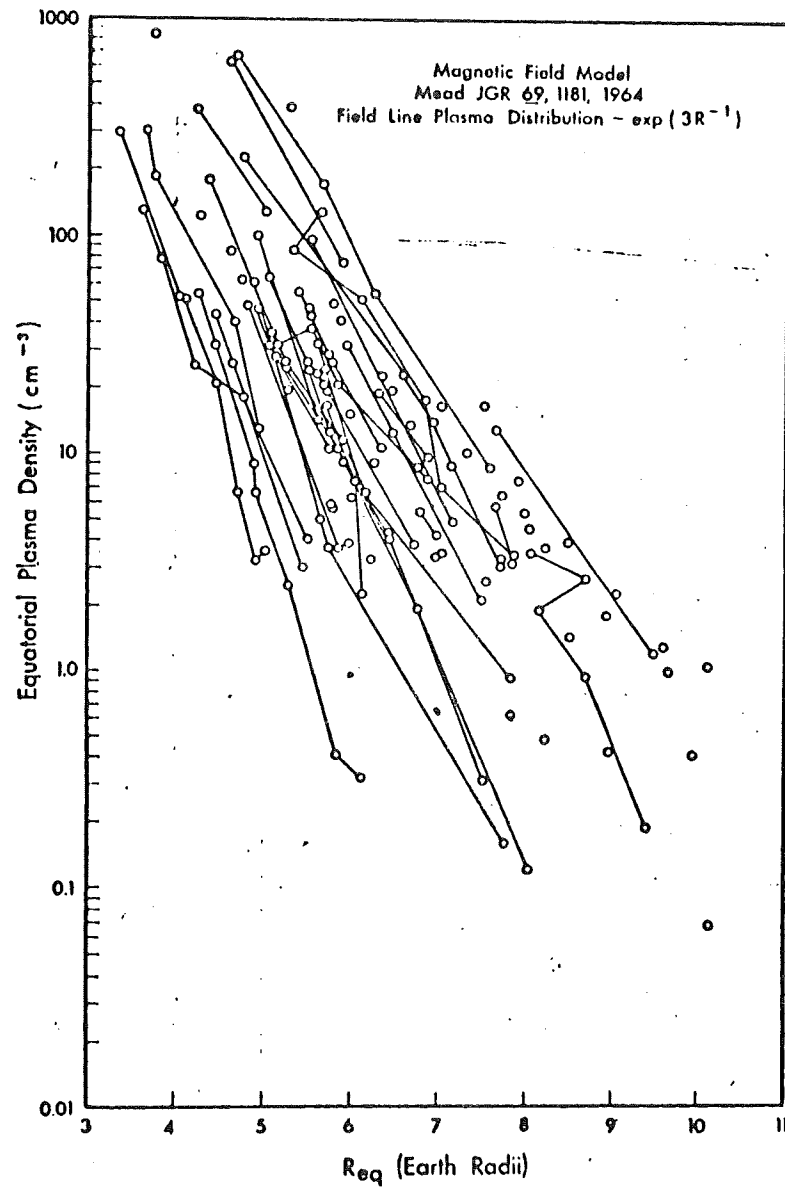


Figure 52: EQUATORIAL PLASMA DENSITY DETERMINED FROM ULF WHISTLER ANALYSIS

(Reference 57)

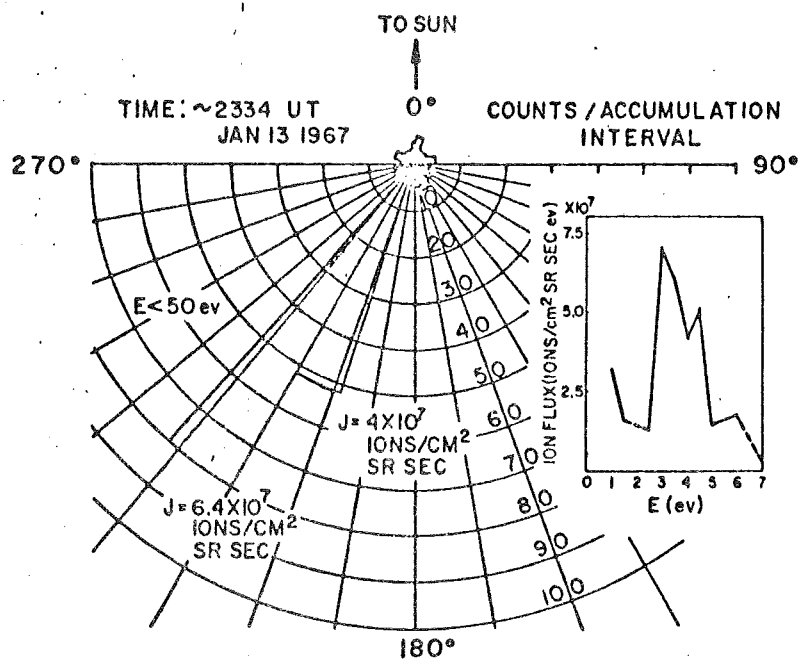


Figure 53: DIRECTIONAL FLOW OF PROTONS AT SYNCHRONOUS ALTITUDE AND POSITIVE ION ENERGY SPECTRUM (INSET)

Explorer satellites have revealed a reasonably consistent picture of this environment. A brief description of the wind's general properties is appropriately given here.

The Solar Wind is effectively a neutral plasma flowing nearly radially from the sun, carrying the solar magnetic field with it to several astronomical units (AU). It consists principally of protons, electrons, and alpha particles with minor concentrations of heavier ions (O^{+6} , O^{+7} , O^{+8} , C^{+6} , He^{+} , O^{+5}). The hot neutral hydrogen density is less than 1 percent of the proton density. The plasma density varies as $1/R^2$ and ranges between 1 and 100 cm^{-3} at one AU with the typical value of 5 cm^{-3} . The alpha/proton density ratio varies between 0.005 and 0.18 with 0.04 being typical. The ions all have similar velocity distributions characterized by a bulk velocity between 270 and 800 km/sec, averaging 400 km/sec.

In the coordinate frame moving with the bulk velocity the ion velocities are represented well by a bimaxwellian distribution. Thus, the ion temperature, generally about 10^5 K , is anisotropic, with the temperature parallel to the magnetic field (T_{11}) typically exceeding the temperature perpendicular to the field (T_1) (Ref. 60). However, Pioneer 6 did observe $T_1 \sim 4T_{11}$ early in the mission (Ref. 64). A small component (~ 2 percent) of plasma energized by the Earth's magnetosphere has been detected not only in the tail of the magnetosphere, but also upstream from the dawn bow shock (Ref. 64).

The electron temperature is generally 1.5 to 5 times the average ion temperature and is more nearly isotropic (Ref. 65). Typically T_{11}/T_1 for the electrons is 1.2 (Ref. 66). Thus the average electron thermal energy is on the order of 25 eV ($T = 2 \times 10^5 \text{ K}$) and far exceeds the energy of bulk motion ($\sim 0.5 \text{ eV}$). The electrons' non-thermal tail ($E > 100 \text{ eV}$), when fitted to a bi-maxwellian distribution, typically yields $n = 5 \times 10^{-2}$ and $T_{11} = 8 \times 10^5 \text{ K}$ (Ref. 63, 66). Thus the electron flux across an imaginary surface exceeds the ion flux by a factor of 4.

The ion fluence spectrum resulting from the fluctuations in the density and in the speed and direction of bulk flow is typically 30° to 40° wide, and it peaks at 0.8 keV and ranges from 0.3 keV to 5 keV. The electron fluence spectrum is effectively isotropic, peaks at 25 eV and contains a high energy tail with a few percent exceeding 100 eV.

The solar array will penetrate the magnetosheath only during large magnetic storms, and the spacecraft may never penetrate the bow shock to reach the undisturbed solar wind. However, a conservatively designed solar array would be capable of operating in the solar wind. Solar wind values typical during large magnetic storms are thus appropriate for the model environment.

13.3.6.2 Trapped Radiation

High energy protons ($> 4.0 \text{ Mev}$) and electrons ($> 0.5 \text{ Mev}$) of the inner and outer radiation belts are trapped in the Earth's dipole-like magnetic field. These radiation belts have been studied intensively since their discovery in 1958 by Van Allen, and an enormous literature exists at present. There are excellent reviews of this literature (Ref. 34, 68, 69).

A substantial continuing effort by NASA and the Air Force is directed to defining the temporal and spatial variation of the particle fluxes. Data from satellites has been compiled by Vette and his co-workers into proton and electron model environments. We recommend the latest of these model environments for evaluating the radiation effects on the high voltage solar array. For protons, this environment would consist of the AP5 map for the energy range from 0.1 to 4 Mev. For 4 to 30 Mev the AP6 map is applicable, while above 30 Mev the AP1 map remains current. For electrons, the AE2 map with the 1968 projection for the inner-belt electrons is applicable. A synchronous altitude electron environment has also been developed(AE3).

The low energy protons ($E < 100$ keV) are significant at synchronous altitude. The spectrum at synchronous altitude, derived from OGO-3 measurements of L. A. Frank, is presented in Figure 54.

Extrapolation of the AE3 synchronous altitude model to 10 keV is sufficiently accurate for our purposes.

13.3.6.3 Solar Flare Activity

Solar activity can modify the environment of the high voltage solar array in several ways:

- o Large optical flares, which are occasionally accompanied by x-ray and solar particle emission, can significantly disturb the lower ionosphere. As the enhancement of the solar electromagnetic spectrum is at short wave lengths, the most pronounced changes occur deep in the ionosphere.
- o The enhanced solar wind pressure associated with solar activity can, as mentioned before, compress the magnetosphere and produce strong time variations in the outer-belt particle fluxes.
- o Energetic particles emitted by certain optical events can degrade solar cells.

Variations in the electron density produced by the large optical flares is included in the ionosphere model. Direct ionization effects on the spacecraft are not significant. Predictions of solar particle activity expected in solar cycle 20 are given in Ref. 70.

The galactic cosmic-rays provide a low-level background of high energy particles throughout the mission. Solar-minimum free-space flux measurements (Ref. 71) show yearly doses of 12 rads and fluxes in the order of 10^8 protons/cm²-year. These particles are not expected to produce any significant problem for solar array operation and they are mentioned only for completeness.

13.3.7 Meteoroids

Meteoroids, small particles in elliptical orbits about the Sun, become meteors as they encounter the Earth's atmosphere. Meteoroids heavier than 10^{-2} grams become sufficiently luminous to be observed visually or photographically.

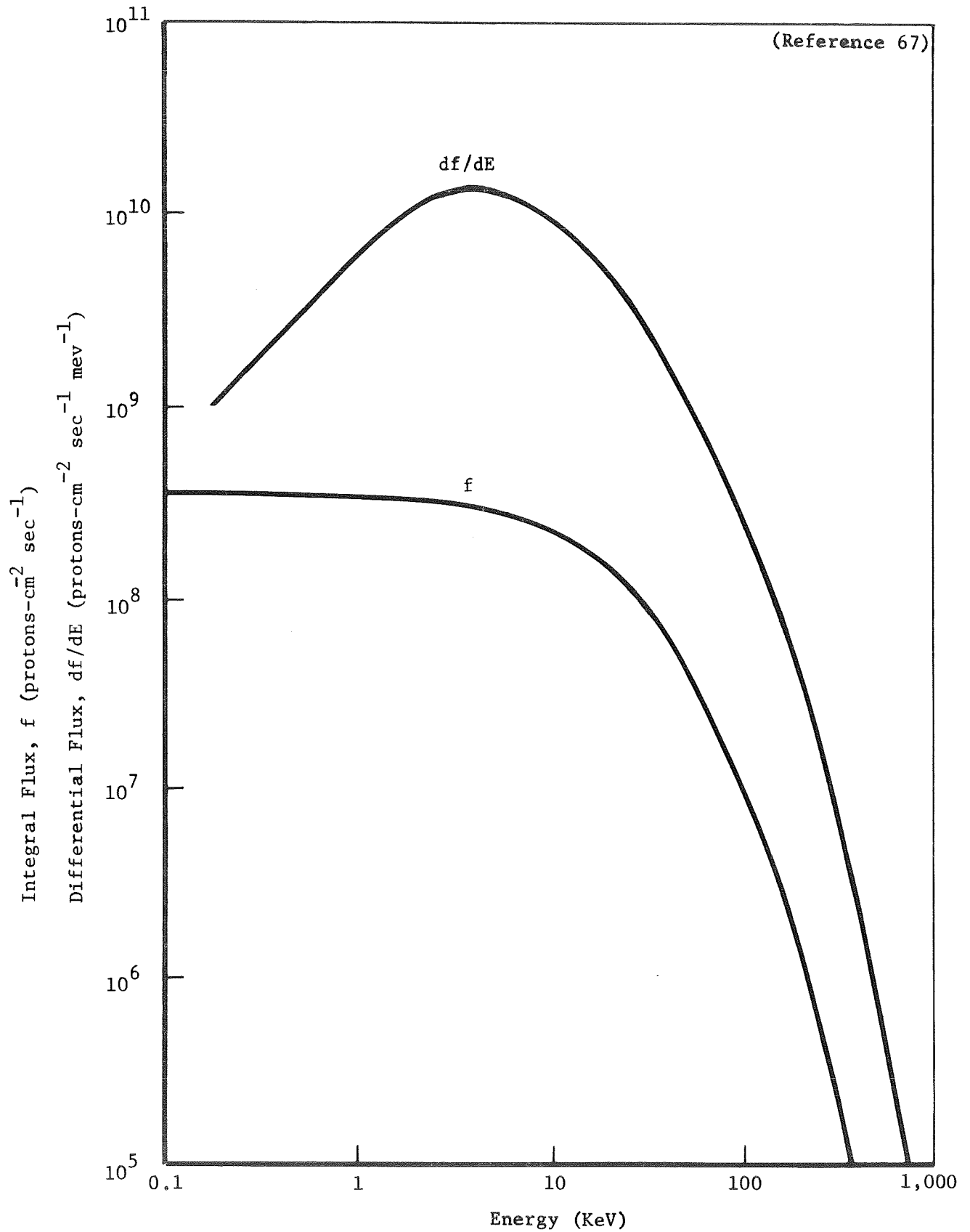


Figure 54: TRAPPED PROTON SPECTRA AT SYNCHRONOUS ALTITUDE

The ionization trails left by meteoroids heavier than 10^{-5} grams can be detected by radio means. More recently satellite sensors have measured impact rates of particles having 10^{-10} to 10^{-6} grams of mass.

Meteoroids are believed to be almost entirely of cometary origin. A small fraction of the annual mass influx of meteors is associated with meteor streams (Ref. 72). Most meteor streams are distinguished by their high geocentric velocity, usually greater than 30 km/sec. Some streams are identified with known comets. Most meteoroids have no observable associations and are called sporadic meteors when they encounter the atmosphere.

Velocity

The average of the observed meteor velocities in the atmosphere is about 33 km/sec. When the observational bias is removed the average velocity is 16.5 km/sec (Ref. 73). Meteors observed in the atmosphere are in hyperbolic paths about the Earth and hence have a minimum velocity of 11.2 km/sec, the escape speed. The velocity distribution of meteoroids is shown in Figure 55.

Flux

The most reliable information on meteoroid rates is obtained from ground-based photographs and from satellite penetration sensors. Neither of these methods provide the mass of the meteoroid directly. The luminous flux of photographic meteors in the Earth's atmosphere (Ref. 74) has been converted to a mass flux by a relation between mass and luminosity (Ref. 73). The average velocity is 16.5 km/sec and the cumulative flux is given by

$$\log_{10} N = -1.21 \log_{10} M - 13.85 \quad (\text{m}^{-2}\text{sec}^{-1})$$

where N is the number of meteoroids and M is their mass.

When the influence of Earth's gravitational field is removed the corrected average velocity becomes 14.2 km/sec and the flux is

$$\log_{10} N = -1.21 \log_{10} M - 14.20 \quad (\text{m}^{-2}\text{sec}^{-1})$$

The straight line portion of the flux curve in Figure 56 is given by the latter expression. The curved portion in Figure 56 has been derived from spacecraft measurements using the methods given in references 75 and 76. Reference 77 gives additional justification. Radio data, although very extensive, is not yet sufficiently correctable to provide flux values. In Figure 56 the region between the satellite and photographic ranges is provided by a linear interpolation.

Satellite penetration rates are converted to mass rates by means of a penetration equation of the form

$$p = k d^{\frac{1}{18}} \rho^{\frac{1}{6}} M^{\frac{1}{3}} v^{\frac{2}{3}}$$

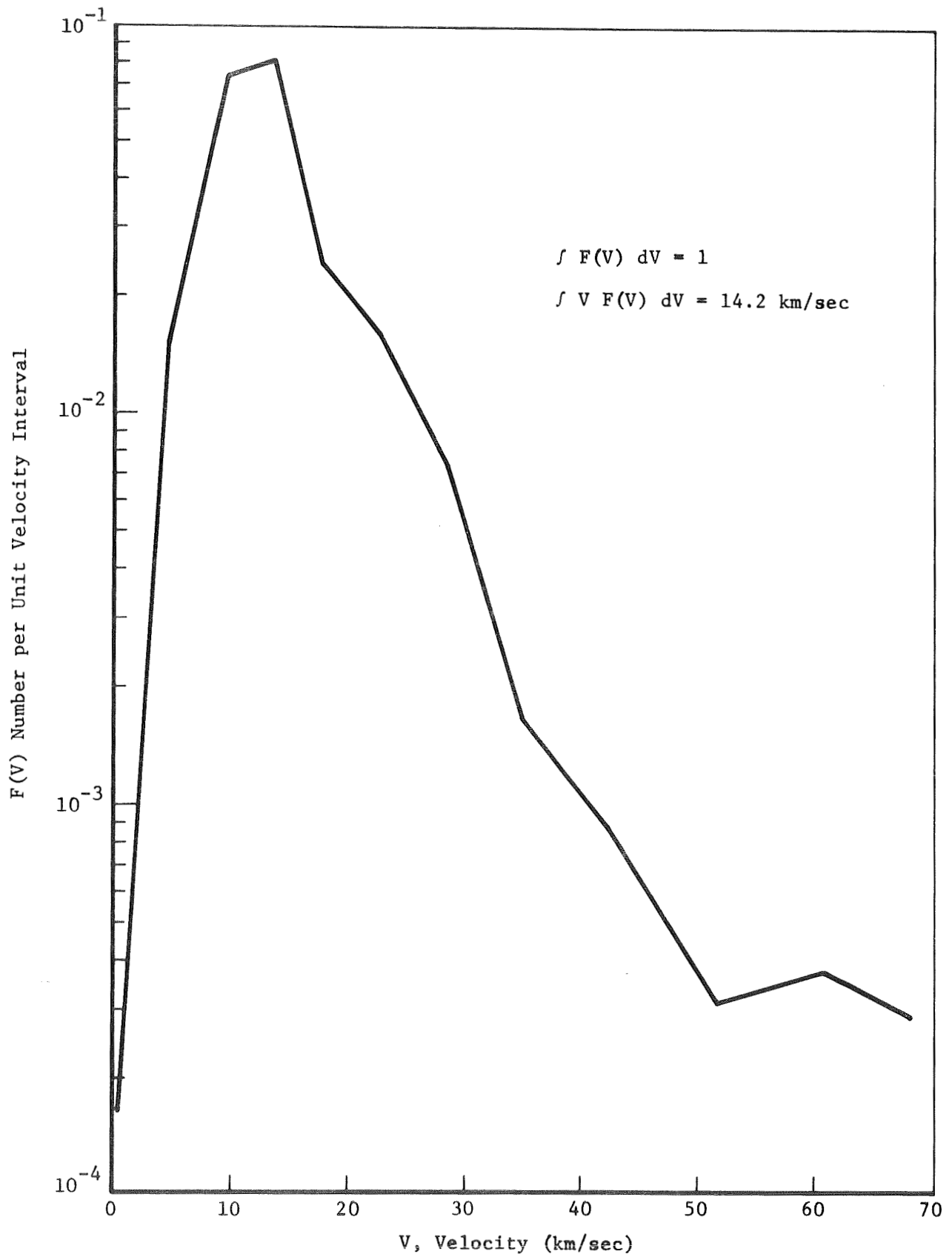


Figure 55: DISTRIBUTION OF METEOROID VELOCITIES RELATIVE TO EARTH
(OUTSIDE THE GRAVITATIONAL INFLUENCE OF EARTH---SPORADICS ONLY)

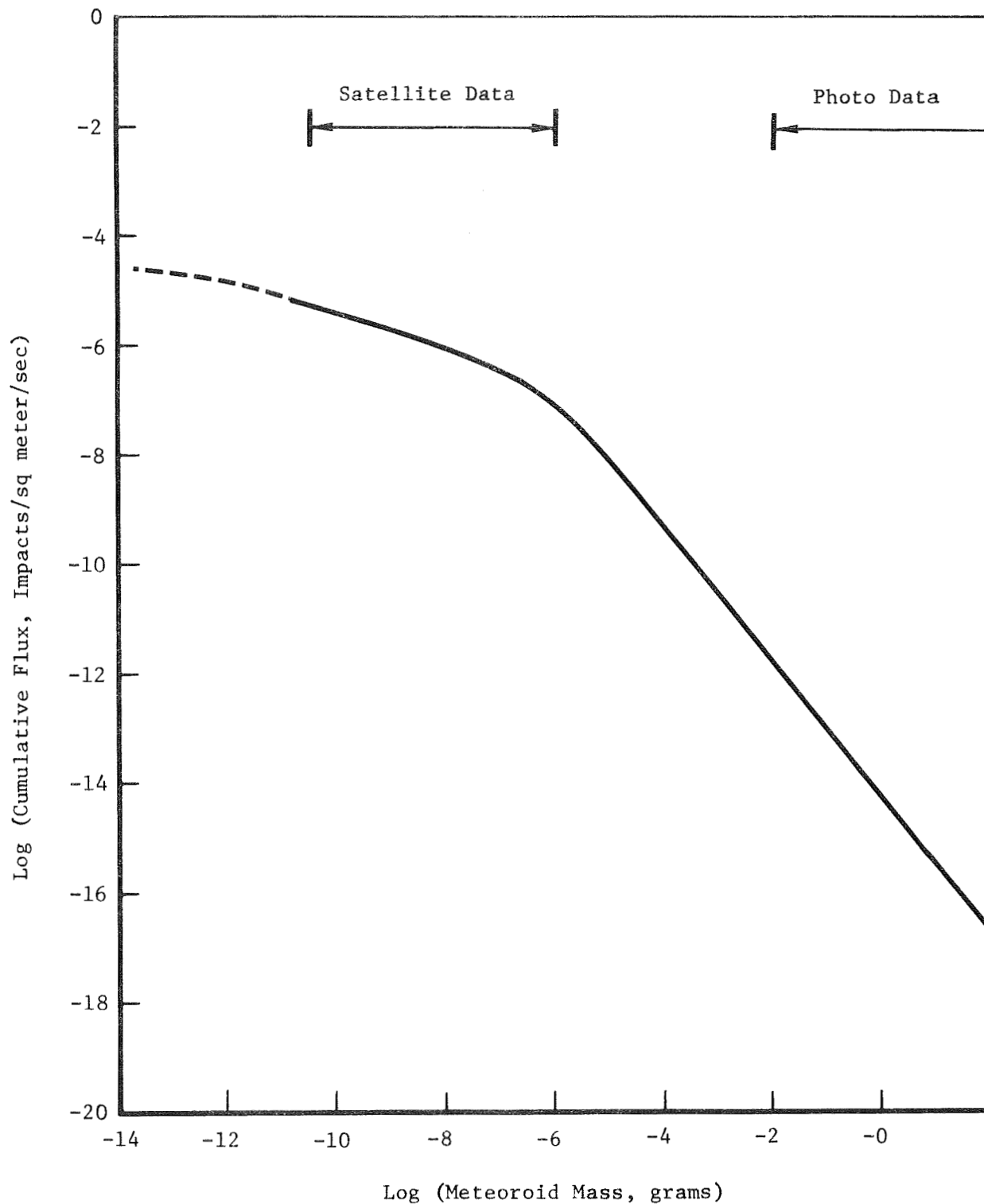


Figure 56: METEOROID ENVIRONMENT NEAR EARTH
(IN THE ABSENCE OF EARTH'S GRAVITATIONAL FIELD)

where p is the penetrated thickness, d is the equivalent spherical diameter of the meteoroid, ρ is its density, M is its mass and V is the velocity relative to the spacecraft. The average velocity for penetration of a satellite in a very high orbit is 17 km/sec. For a near-Earth satellite it is 19 km/sec. This difference is a consequence of the greater speed of both the satellite and the meteoroids in low orbits.

The flux encountered by the satellite varies with orbital radius as a consequence of satellite motion and the focusing effect of the Earth's gravitational field on the meteoroids (Ref. 75). The mass flux curve in Figure 57 gives the variation in the rate which particles of a given mass are swept up by the satellite. The penetrating flux is the rate at which a given thickness of material would be penetrated.

Meteor Streams

The contribution by annual meteor streams to the meteoroid mass influx is about one percent per year. About 6 percent of the energy influx comes from streams (Ref. 72). The very large visual rates of meteor streams results from their high atmosphere velocities, the luminosity varying approximately as MV^4 . In the peak intensity of an annual stream the penetration rate would be at most double the average rate (Ref. 72 and 73).

Physical Characteristics

The physical consistency of meteors is in keeping with a cometary origin. They have little strength, disintegrating readily in the atmosphere. When observed they are at an altitude between 70 and 120 km. Photographic meteors have an average density of about 0.25 gm/cc (Ref. 78) and faint radio meteors have a density of 0.8 gm/cc (Ref. 79). In the range 10^{-5} to 1 gram the density can be related to mass by

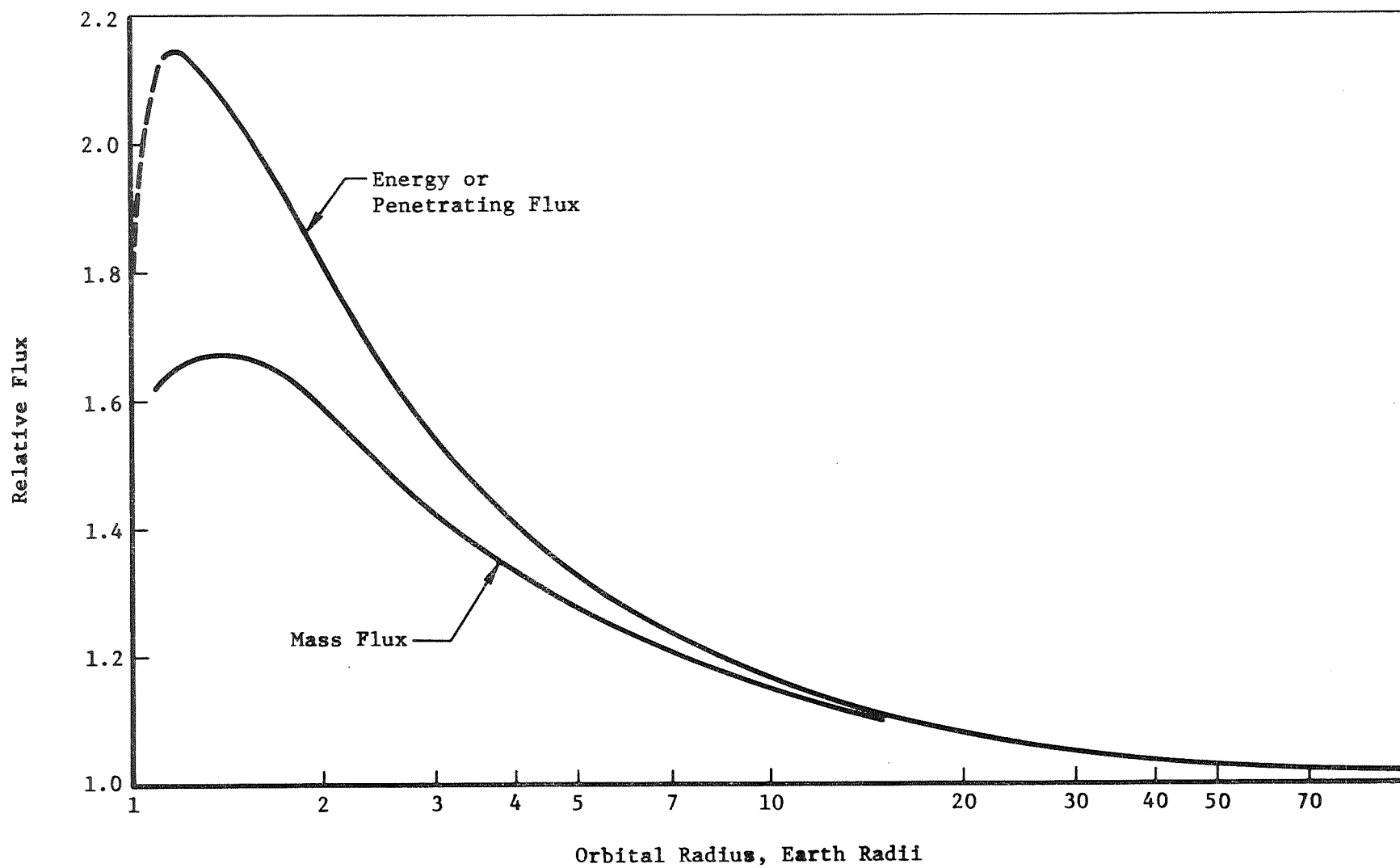
$$\rho = 0.25 M^{-\frac{1}{8}}$$

13.4 ENVIRONMENTAL MODEL

The environment most important to the high-voltage solar array study is the ionosphere. The micrometeoroid environment is also important. The geometric field, neutral atmosphere, solar spectrum, auroral and polar storm particles, and the magnetosphere contribute only secondary effects. However, they influence the spatial and temporal distribution of the ionosphere. Hence their description is necessary in establishing the significance of the variations in the ionosphere model.

13.4.1 Geomagnetic Field

For this study the tilted dipole model of the geomagnetic field (Ref. 40) is sufficient. If a more accurate near-Earth model were needed, then the appropriate one would be the 1960 Jensen and Cain field model (Ref. 35) which has been graphically displayed by horizontal (Ref. 81) and meridional (Ref. 82) projections. The modification of the dipole field model at synchronous altitude caused by the solar wind interaction is described below in the magnetospheric model.



D2-121734-1

Figure 57: METEOROID FLUX AT A SPACECRAFT IN A CIRCULAR ORBIT ABOUT EARTH
(THE FLUX IS NORMALIZED TO THE VALUE AT INFINITY)

13.4.2 Neutral Atmosphere

The neutral atmosphere model for this study will be the 1962 Standard atmosphere (Ref. 37), and its supplement (Ref. 38) for the analysis of effects of seasonal and solar activity variations of the exosphere.

13.4.3 Solar Spectrum

The model solar spectrum (Figure 58) is adapted from Reference 39. Also shown is the Sun's 6000°K black body spectrum, which is sufficient for estimating array temperatures.

13.4.4 Auroral and Polar Storm Particles

Rocket (Ref. 83, 84) and satellite (Ref. 85) measurements have shown the peak fluxes of low-energy electrons and protons in the auroral zone (Figure 59). Typically, the flux of electrons of energy ≤ 10 keV becomes $10^9 \text{ cm}^{-2}\text{sec}^{-1}\text{sr}^{-1}$. The 1 to 10 keV proton flux is about the same. We consider the peak flux to be more significant to the study than a typical moderate storm flux. The model therefore is the auroral-storm peak flux, $10^{10} \text{ cm}^{-2}\text{sec}^{-1}\text{sr}^{-1}$, with the spectrum in Figure 60 at the top of the atmosphere.

13.4.5 Ionosphere

The plasma-density model, derived from the envelope of altitude profiles, is shown in Figure 61. This model represents the peak electron densities that will be encountered. Mean values were not derived, but they would range between 1/4 and 1/10 of the values in the model.

A typical daytime profile of electron and ion temperature was chosen for the model (Figure 62). The variation of temperature with geomagnetic latitude, as previously discussed, should be considered if significant. The 6000°K temperature at 1000 m in the auroral zone should be considered if spacecraft flight in this region is planned.

The ionosphere composition is under strong geomagnetic and local time control. We adopted for a model the composition measured by Brinton et al (Figure 38), but scaled so that the total ion density equals the model electron density. Should a particular ionic species become important to the study, a peak density versus altitude plot will be included in the model.

13.4.6 Magnetosphere

For the solar wind model, the upper ion velocities are those described in section 13.3.6.2.

For this study the trapped radiation model is that of J. I. Vette and co-workers. The proton environment below synchronous altitude consists of AP5 (0.1 to 4 meV), AP6 (4-30 meV) and AP1 (> 30 meV) while the electron environment will be the AE2 model-1968 prediction. At synchronous altitude the mean AE3 electron model is recommended and the proton spectrum is as presented in Figure 54.

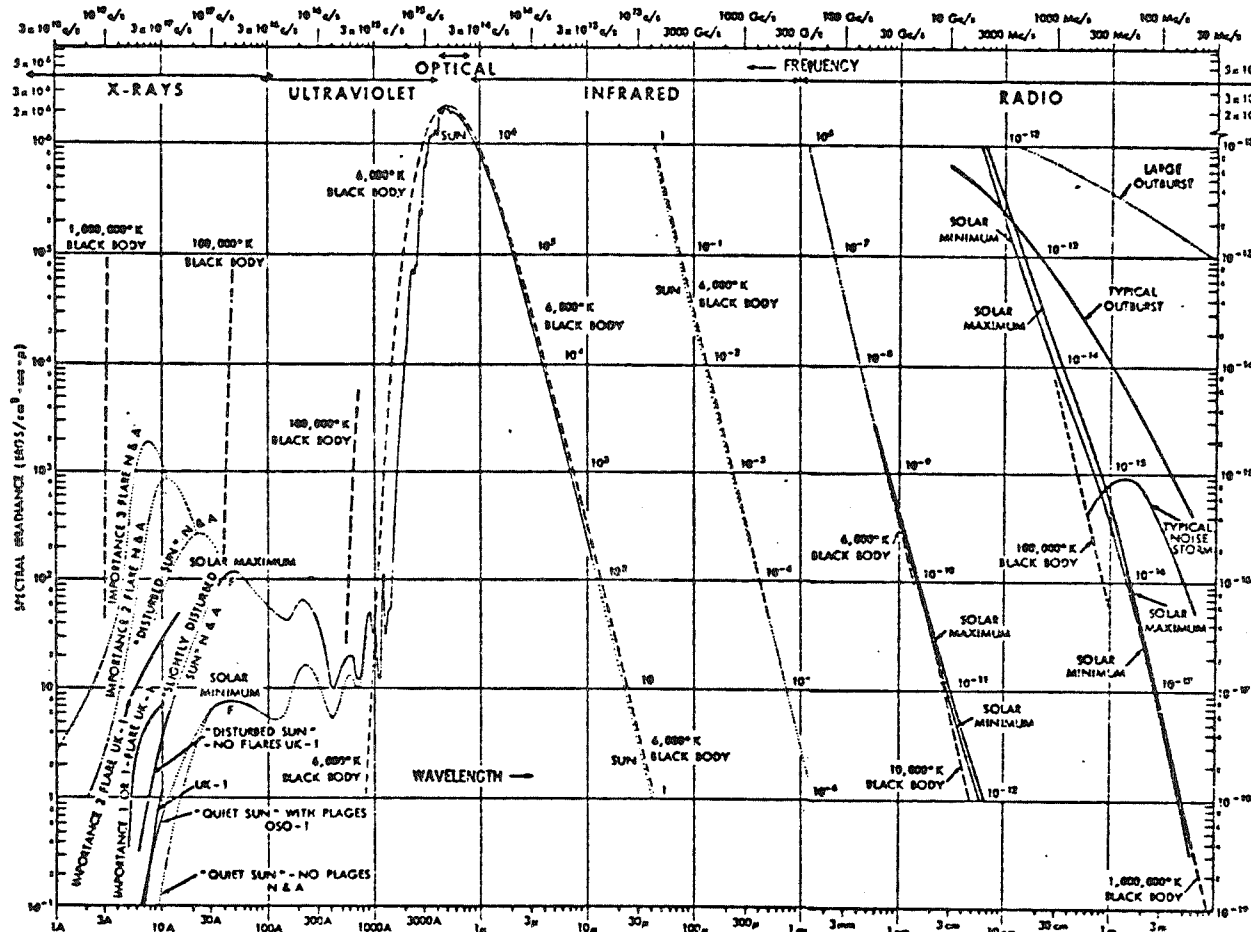


Figure 58: THE SOLAR SPECTRUM AS OBSERVED OUTSIDE THE EARTH'S ATMOSPHERE

(Reference 60)

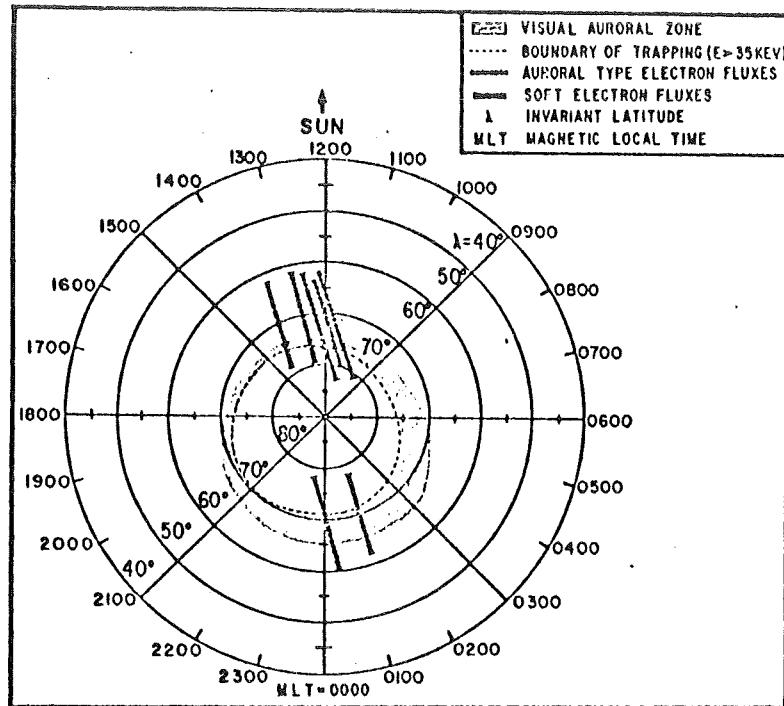


Figure 59: DIURNAL VARIATION OF THE POSITION OF THE "AURORAL ZONE" AND SOFT ELECTRON FLUXES ON JUNE 30, 1967 ($K_p \approx 3$)

(Reference 60)

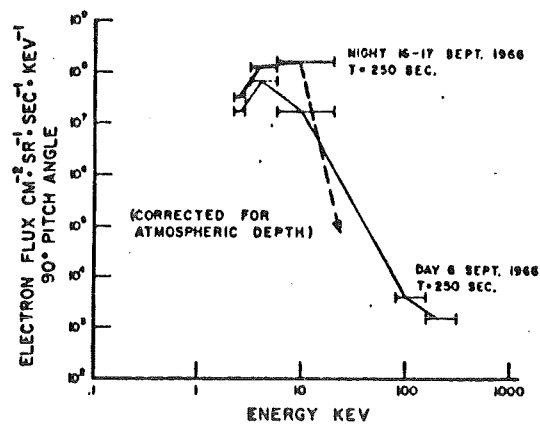


Figure 60: SPECTRA OF AURORAL ZONE ELECTRONS

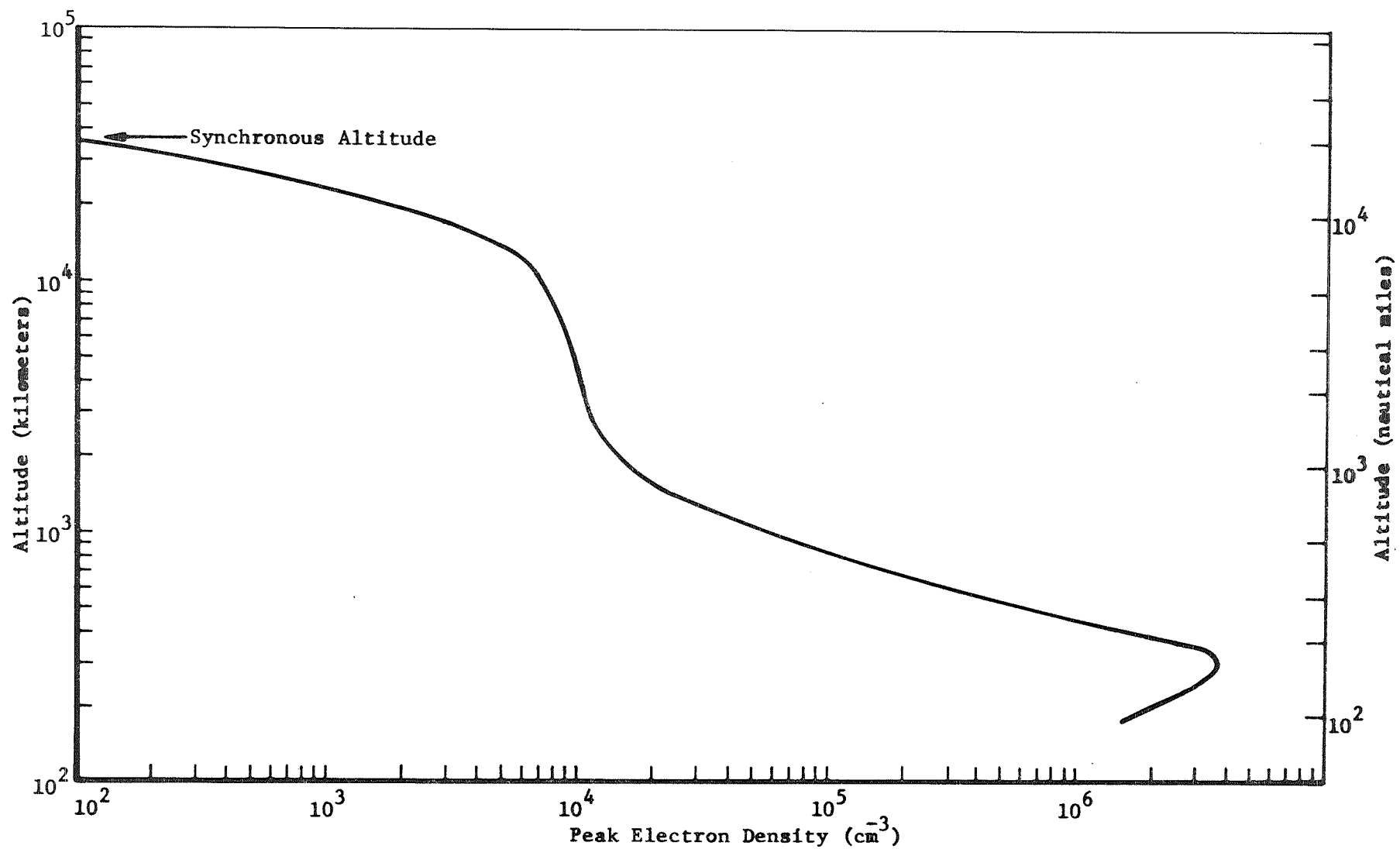


Figure 61: MODEL ELECTRON DENSITY VERSUS ALTITUDE

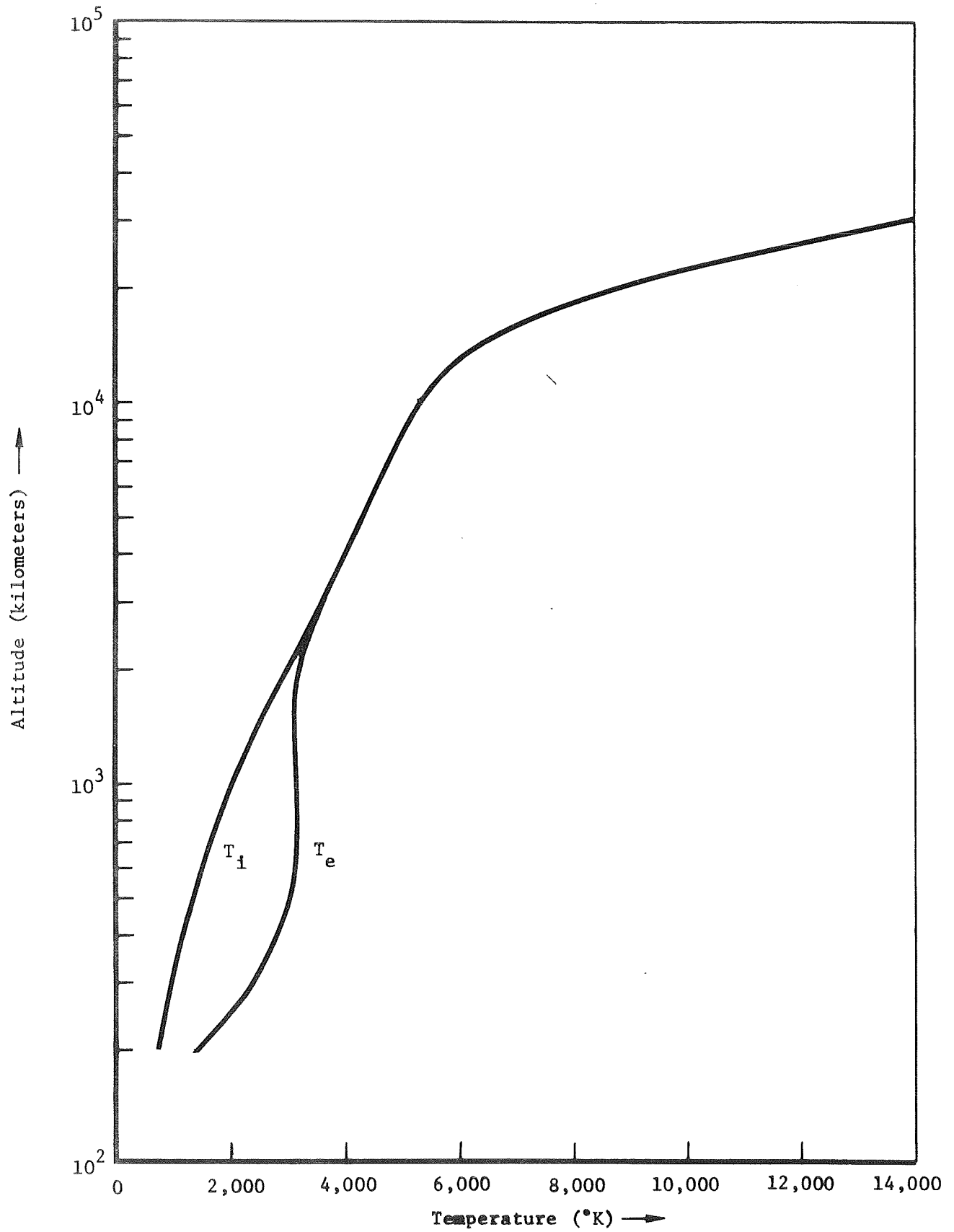


Figure 62: MODEL ELECTRON AND ION TEMPERATURE VERSUS ALTITUDE

The influences of solar activity on the ionosphere, the solar spectrum, and the solar wind have been included in the appropriate environment models. High-energy particle fluxes for the time period of interest are available in Reference 70.

13.4.7 Meteoroids

The model for cumulative meteoroid flux is reproduced in Figure 56. The velocity distribution is given in Figure 55 and the correction to the mass and energy flux distributions for near Earth orbits is given in Figure 57.

14.0

REFERENCES

1. Sellen, J. M. Jr. and R. G. Kemp, "Research of Ion Beam Diagnostics", Report No. NASA CR-54692, prepared by TRW Systems under Contract NAS 3-6276 (Feb. 1966)
2. Cole, C. K., H. S. Ogawa and J. M. Sellen Jr., "Operation of Solar Cell Arrays in Dilute Streaming Plasmas", Report No. NASA CR-72376, prepared by TRW Systems under Contract NAS3-10612 (March, 1968)
3. Sellen, J. M. Jr., and R. J. Cybulski, "Environmental Effects on Laboratory and In-Flight Performance of Neutralization Systems", Report No. NASA TMX-52093 (1965)
4. Chen, F. F., "Electric Probes", Plasma Diagnostic Techniques, edited by R. H. Huddlestone and S. I. Leonard, Academic Press, New York, pp. 113-200 (1965)
5. Schott, L., "Electrical Probes", Plasma Diagnostics, edited by W. Lockte-Holtgren, North Holland Publishing Co., Amsterdam; John Wiley & Sons Inc., New York, pp. 668-725 (1968)
6. Cole, R., H. Ogawa, J. Sellen, Jr., "Operation of Solar Cell Arrays in Dilute Streaming Plasma, NASA CR72376, March, 1968.
7. Abstracts of papers presented in Session 5E of the 1969 Annual Meeting of the Division of Plasma Physics, held Nov. 12-15, 1969, Bulletin of American Physical Society, 14 (1969).
8. Burroughbridge, D. R., "A Technique for Simulating the Ionospheric Plasma", Goddard Space Flight Center Report No. X-325-68-172, (May, 1968)
9. Medved, D. B., "On the Formation of Satellite Electron Sheaths Resulting from Secondary Emission and Photoeffects", Interactions of Space Vehicles with an Ionized Atmosphere, edited by S. F. Singer, Pergamon Press, pp. 305-321, (1965)
10. Batanov, G. M., "Secondary Emission of No. 46 Glass Under the Effect of Positive Ions of Some Gases, Soviet Physics Solid State 2, 1839 (1961).
11. Greene, D., "Secondary Electron Emission from Molybdenum produced by Helium, Neon, Argon and Hydrogen", Proc. Phys. Soc. (London), B62, 876 (1950).
12. Reynolds, T. W. and E. A. Richley, "Propellant Condensation on Surfaces Near an Electric Rocket Exhaust", AIAA Paper No. 69-270, AIAA Seventh Electrical Propulsion Conference, (March 1969)
13. Langmuir, I., "Currents Limited by Space Charge Between Concentric Spheres", Phys. Rev. 23, 49 (1924)

14. Schwartz, "Measurement Techniques for Thin-Films", Johnson Reprint Corporation, pp. 191-272, (1967).
15. Colligan, J. S., "Ion Bombardment of Metal Surfaces", Vacuum 11, 272 (1961).
16. Hansen, R. G. and others, "Effects of Atomic Oxygen on Polymers", Journal of Polymer Science, Vol. A3, 2205 (1965)
17. Jaffe, L. D. and J. B. Rittenhaus, "Behavior of Materials in Space Environments", JPL Technical Report No. 32-150 (Nov. 1, 1961)
18. Kilpatrick, W. D., "Progress in Dielectrics" No. 7, p. 199, London Heywood Books, (1967)
19. N. Riehl, et al, "Non Destructive Breakdown in Mylar Films, Part I," Z. Angewandte Physik 27, 261 (1969)
20. Whitehead, S., "Dielectric Breakdown of Solids," Oxford (1953)
21. Fowler, R. H. and L. W. Nordheim, "Electron Emission in Intense Electric Fields," Proc. Royal Society (London) A119, 173 (1928)
22. Nordheim, L. W., "The Effect of the Image Force on the Emission and Reflexion of Electrons by Metals," Proc. Royal Society (London) A121 626 (1928)
23. Schottky, W., Physik Z. 15, 872 (1914)
24. Dobrezow, L. N., "Electron and Ion Emission of Thoriated Wolfram in Sodium Vapour," J. Exp. Theor. Physics (USSR) 17, 301 (1947)
25. Good, R. H. and E. W. Muller, "Field Emission at Higher Temperatures," Handbuch der Physik 21, 190 (1956)
26. Kaminsky, M., "Atomic and Ionic Impact Phenomena on Metal Surfaces," Academic Press, New York (1965)
27. Hawley, R. and A. A. Zaky, "Conduction and Breakdown in High Vacuum," Progress in Dielectrics #7, p. 115, London Heywood Books, (1967)
28. Cooley and Barrett, "Handbook of Space Environmental Effects on Solar Cell Power Systems," Exotech Inc., NASW-1345, (Jan. 1968)
29. "Feasibility Study 30 Watts Per Pound Rollup Solar Array," Final Report No. 40067-4, Ryan Aeronautical Company, (June 1968)
30. Murray, William A., The Boeing Company, "What Parts Lessons from Lunar Orbiter?" Proceedings 1969 Annual Symposium on Reliability
31. Binckley, W. G., TRW Systems, "Power System Configuration Study and Reliability Analysis," 3rd Quarterly Progress Report, JPL Contract No. 951574

32. Tanner, T. L., Bell Telephone Laboratories, "Operational Reliability of Components in Selected Systems," 1966 Annual Symposium on Reliability.
33. "Tables of the Individual and Cumulative Terms of the Poisson Distribution," Defense Systems Department, General Electric Company
34. Hess, W. N., "The Radiation Belt and Magnetosphere," Blaisdell Publishing Co., Waltham, Mass., (1968)
35. Jense, D. C., and J. C. Cain, "An Interim Magnetic Field," J. Geophys. Res., 67 3568, (1962)
36. Mead, G. D., "Deformation of the Geomagnetic Field by the Solar Wind," J. Geophys. Res., 69 1181, (1964)
37. "U. S. Standard Atmosphere, 1962," Committee on Extension to the Standard Atmosphere (COESA), Wash., D. C., (December 1962)
38. "U. S. Standard Atmosphere Supplements, 1966" NASA, ESSA, Air Force, Wash., D. C., (1966)
39. "Introduction to Space Science," W. N. Hess and G. D. Mead, editors Gordon and Breach, New York, (1968) Pages 668 and 669
40. "Handbook of Geophysics and Space Environments," Air Force Cambridge Research Laboratories, (1965)
41. "Ionospheric Radio Propagation," Kenneth Davies, National Bureau of Standards, (1965)
42. "Introduction to Space Sciences," Second Edition, Edited by W. N. Hess and G. D. Mead, Gordon and Breach Science Publishers, New York, (1968)
43. Rawer, K., and K. Suchy, "Radio-Observations of the Ionosphere" in Encyclopedia of Physics, Volume XLIX, Part 2, Ed., S. Flugge, Springer-Verlag, New York, (1967)
44. Evans, J. V., "Theory and Practice of Ionospheric Study by Thomson Scatter Radar" Proceedings of the IEEE, 57, (1969)
45. Electron Density Profiles in Ionosphere and Exosphere, Edited by J. Frihagen, North-Holland, Amsterdam, (1966)
46. Bramley, E. N., and M. Peart "Diffusion and Electromagnetic Drift in the Equatorial F2 Region," J. Geophys. Res. 69, 4609, (1964)
47. Sterling, D. L., W. B. Hanson, R. J. Moffett and R. G. Bextor, "Influence of Electromagnetic Drifts and Neutral Air Winds on Some Features of the F2-Region," Southwest Center for Advanced Studies Report #SP-69-008, Submitted to the J. Geophys. Res. (March 1969)

48. Evans, J. V., "Sunrise Behavior of the F-Layer at Mid Latitudes," J. Geophys. Res. 73, 3489 (1968)
49. Brace, L. H., N. W. Spencer, and A. Dalgarno, "Detailed Behavior of the Midlatitude Ionosphere from Explorer XVII Satellite," Planet. Space Sci. 13, 647 (1965)
50. Taylor, H. A. Jr., H. C. Brinton, M. W. Pharo, III, and N. K. Rahman, "Thermal Ions in the Exosphere; Evidence of Solar and Geomagnetic Control," J. Geophys. Res. 73, 5521 (1968)
51. Taylor, H. A. Jr., H. C. Brinton, and M. W. Pharo, III, "Contraction of the Plasmasphere During Geomagnetically Disturbed Periods," J. Geophys. Res. 73, 961, (1968)
52. Binsack, J. H., "Plasmapause Observations with the M.I.T. Experiment on IMP 2," J. Geophys. Res. 72, 5231 (1967)
53. Carpenter, D. L., C. G. Park, H. A. Taylor, Jr., and H. C. Brinton, "Multi-Experiment Detection of the Plasmapause from EOGO Satellites and Antarctic Ground Stations," J. Geophysics Res. 74, 1837 (1969)
54. Liemohn, H. B., J. F. Kenney, and H. B. Knafllich, "Proton Densities in the Magnetosphere from Pearl Dispersion Measurements" Earth Planetary Sci. Letters 2, 360, (1967)
55. Kenney, J. F., H. B. Knafllich and H. B. Liemohn "Magnetospheric Parameters Determined from Structured Micropulsations," J. Geophys. Res. 73, 6737, (1968)
56. Angerami, J. J., "A Whistler Study of the Distribution of Thermal Electrons in the Magnetosphere," Stanford Electronics Lab. Tech. Rept., 3412-7, (1966). See also D. L. Carpenter, "Whistler Studies of the Plasmapause in the Magnetosphere, 2, Electron Density and Total Tube Electron Content near the Knee in the Magnetospheric Ionization, J. Geophys. Res. 71, 711, (1966)
57. Freeman, J. W., Jr., "Observation of Flow of Low-Energy Ions at Synchronous Altitude and Implications for Magnetospheric Convection," J. Geophys. Res. 73, 4151, (1968)
58. Brinton, H. C., M. W. Pharo, III, H. G. Mayr, and H. A. Taylor, Jr., "Implications for Ionospheric Chemistry and Dynamics of a Direct Measurement of the Ion Composition in the F2 Region," J. Geophys. Res. 74, 2941, (1969)
59. Banks, P. M., and T. E. Holzer, "The Polar Wind," J. Geophys. Res. 73, 6846, (1968) and J. Geophys. Res. 74, 3734, (1969)
60. Findlay, J. A., P. L. Dyson, L. H. Brace, A. J. Zmuda and W. E. Radford, "Ionospheric and Magnetic Observations at 1000 km During the Geomagnetic Storm and Aurora of May 25-26, 1967," J. Geophys. Res. 74, 3705, (1969)

61. Dessler, A. J., Reviews of Geophys. 5, 1, (1967)
62. Hundhausen, Bame and Ness, J. Geophys. Res. 72, 5265, (1967)
63. Wolfe, J. H., and D. D. McKiblen, Planet. Space Sciences 16, 953, (1968)
64. Ashbridge, Bame and Strong, J. Geophys. Res. 73, 5777, (1968)
65. Montgomery, Bame and Hundhausen, J. Geophysical Res. 73, 4999, (1968)
66. Formisano, V. J. Geophys. Res. 74, 355, (1969)
67. Frank, L. A., Trans. Am. Geophys. Union, 49, 262, (1968)
68. Anderson, K. A., "Energetic Particles in the Earth's Magnetic Field," Annual Reviews of Nuclear Science, Vol. 16, 291, (1961)
69. Filkins, R. W., "Trapped Protons of the Inner Radiation Belt," J. Geophys. Res. 71, 97, (1966)
70. Webber, W. R., and J. R. Thomas, "Sunspot Number and Solar Cosmic Ray Predictions for Cycle 20, 1965-1975 With Preliminary Estimates for Cycle 21," Boeing Document No. D2-113522-1, (May, 1967)
71. Curtis, S. B. and M. C. Wilkinson, "Study of Radiation Hazards to Man on Extended Missions," NASA CR-1037, (May 1968)
72. Erickson, J. E., "Mass Influx and Penetration Rate of Meteor Streams," J. Geophys. Res. 74, 576-585, (1969)
73. Erickson, J. E., "Velocity Distribution of Sporadic Photographic Meteors," J. Geophys. Res. 73, 3721-3726, (1968)
74. Hawkins, G. S., and E. K. L. Upton, "The Influx Rate of Meteors in the Earth's Atmosphere," Astrophys. J. 128, 727, (1958)
75. Erickson, J. E., "Analysis of the Meteoroid Flux Measured by Explorer 16 and Lunar Orbiter," Astron. J. 74, 279-283, (1969)
76. "Space Vehicle Integrated Thermal Protection/Structural Meteoroid Protection System," A technical proposal to NASA - Lewis Research Center (RFP C-358689) Boeing Document D2-121085-1, (June 1969)
77. Naumann, R. J., "The Near-Earth Meteoroid Environment," NASA Rept. TN D-3717, (1966)
78. Jacchia, L. G., F. Vernioni, and R. E. Briggs, "An Analysis of the Atmospheric Trajectories of 413 Precisely Reduced Photographic Meteors," Smithsonian Contrib. Astrophys. 10, 1, (1967)
79. Vernioni, F., "Physical Characteristics of 320 Faint Radio Meteor", J. Geophys. 71, 2749-2761, (1966)

80. Clifton, S., and R. Naumann, "Pegasus Satellite Measurements of Meteoroid Penetration," NASA, Rept. TM X-1316, (1966)
81. Dudziak, W. F., D. D. Kleinecke and T. J. Kostigen "Graphical Displays of Geomagnetic Geometry," G. E. Tempo Rept. RM 63 TMP-2, (April 1963)
82. Harrison, R. E., R. W. Hubbard, F. L. Keller and J. I. Vette "Plots of Constant B and Constant L for Various Longitudes," Aerospace Corp. Rept. TDR-169 (3510-41) TR-4, (Sept. 1963)
83. Chase, L. M., "Spectral Measurements of Auroral-Zone Particles," J. Geophys. Res. 73, 3469, (1968)
84. Bernstein, W., G. T. Inouge, N. L. Sanders, and R. L. Wax, "Measurements of Precipitating 1-20 Kev protons and Electrons During a Breakup Aurora," J. Geophys. Res. 74, 3609, (1969)
85. O'Brien, B. J., "High-Latitude Geophysical Studies with Satellite Injun 3, 3, Precipitation of Electrons into the Atmosphere," J. Geophys. Res. 69, 13, (1964)